PREDICTION OF CUTTING FORCES IN FIVE-AXIS MICRO-BALL END MILLING

BY

CHI XU

THESIS

Submitted in partial fulfillment of the requirements
for the degree of Master of Science in Mechanical Engineering
in the Graduate College of the
University of Illinois at Urbana-Champaign, 2015

Urbana, Illinois

Advisor:

Professor Shiv Kapoor

ABSTRACT

Five axis micro-ball end milling has been shown as a viable option for machining complex free form surfaces with high aspect ratios and provide micron-scale tolerances. Unfortunately, due to the high fragility of the cutting tool, premature tool failure has been a major challenge in micro-scale machining. Tool strength of a micro-ball end mill can be easily exceeded by the strain induced by cutting force, thus cutting force is desired to be accurately predicted. Traditionally, researchers have used the mechanistic relationship between experimental force and chipload to develop empirical cutting force models for end mill operation. However, these models suffer the drawbacks including the need for extensive experimental calibration, and the limitation to in-plane tool movements. Therefore a comprehensive cutting force model that is suitable for micro-ball end milling operation is desired.

The work in this thesis presents a five-axis ball end milling force model that is specifically tailored to micro-scale machining. A composite cutting force is generated by combining two force contributions from a shearing/ploughing slip-line field model and a quasi-static indentation model. To fully capture the features of micro-scale five-axis machining, a unique chip thickness algorithm based on the velocity kinematics of a ball end mill is proposed. This formulation captures intricate tool trajectories as well as readily allows the integration of runout and elastic recovery effects. A workpiece updating algorithm has also been developed to identify tool-workpiece engagement. As a dual purpose, historical elastic recovery is stored locally on the meshed workpiece surface in vector form so that the

directionality of elastic recovery is preserved for future time increments. The model has been calibrated and validated through a comparison with experiment data gain by five axis micro-ball end mill testing. Simulation results show reasonably accurate prediction of end milling cutting forces with minimal experimental data fitting. A potential model application for machining process planning is also presented.

For My Family

ACKNOWLEDGEMENTS

I would like to express my gratitude to my academic advisor, Professor Shiv G. Kapoor for his technical and financial support through the process of this research as well as his patient, guidance and encouragement. None of my contribution in this thesis would be possible without the help from him. I also want to thank James Zhu for his extraordinary help and technical support throughout this research, and Avery Rosenbloom for his initial works on this topic.

This research was funded through the Grayce Wicall Gauthier Chair at the University of Illinois, Urbana, Illinois. I am also thankful to the department of Mechanical Science and Engineering for the financial support during my graduate study.

I would also like to thank Professor Bretl for his helpful discussions during the early stage of this research.

Furthermore, I would like to thank all of my fellow graduate research assistants that I worked closely with, especially Soham, Asif, Chandra, Arvin, Surojit, Jin, Jorge, Kyle and Hazel.

Most importantly I would like to thank my family for their unconditional support and endless encouragement.

TABLE OF CONTENTS

Nomenclature

$d\gamma$	Discretized cutter edge polar angle segment
$\overrightarrow{P_t}$	Tool cutting edge point in tool frame
$\overrightarrow{P_w}$	Tool cutting edge point in workpiece frame
N_s	Total number of discretized circular sectors
$[X_t, Y_t, Z_t]$	Cartesian tool coordinate frame
R_0	Nominal radius of the ball end mill
φ	Tool immersion angle
λ	Local helix angle
δ	Lag angle
N_f	Total number of flutes
$[X_w, Y_w, Z_w]$	Workpiece coordinate frame
l_t	Length of the tool
α	Angular axis misalignment angle on Z- axis
β	Angular axis misalignment angle on X- axis
$\varepsilon_x, \varepsilon_y$	Parallel axis runout components
ε	Total parallel runout
λ_s	Parallel runout locating angle
θ	Spindle rotation angle
Ω_z, Ω_x	Tool inclination angles

$\overrightarrow{Q_w}$	Tool center position vector
$x_{tool}, y_{tool}, z_{tool}$	Position vector components in the workpiece coordinate frame
$\boldsymbol{T}_t^i$	Intermediate tool frame transformation matrix
$\boldsymbol{T}_t^w$	Workpiece frame transformation matrix
$\boldsymbol{A}$	Rotation matrix
$\vec{d}$	Translational vector
N	Spindle speed
$\overrightarrow{n_r}$	Outward radial vector
$\overrightarrow{h_{ro}}$	Tool runout factor
$\overrightarrow{h_{er}}$	Elastic recovery vector
$\overrightarrow{h_{er,prev}}$	Elastic recovery vector from a previous time increment
$\vec{f}$	Tool feed vector
κ	Elastic recovery rate factor
p_e	Recovery rate for mixed elasto-plastic deformation[1]
$t_{c,min}$	Minimum chip thickness
t_{ce}	Chip thickness corresponding to the elastic limit of the material
$\overrightarrow{t_c}$	Total chip thickness
z_{node}	Interpolated Z-height
z_i	Z-height on cutting edge points
A_i	The area opposite to the vertex of Z- height z_i
A	Unit square area

dS	Infinitesimal length of the helical cutting edge segment
df_{sc}	Differential shearing force in cutting direction
df_{st}	Differential shearing force in thrusting direction
df_{pc}	Differential ploughing force in cutting direction
df_{pt}	Differential ploughing force in thrusting direction
k	Material shear flow stress
ϕ	Shear angle
α_o	Nominal rake angle
α_e	Effective rake angle
$a_\theta, a_1, a_2, e_0, e_1, e_2$	Coefficients defined by [1]
η_0, η_1, η_2	Friction factors defined by [1]
ψ, ψ_e, α_p	Slip-line field angles defined by [1]
l_s, l_b	Slip-line lengths in chip-formation force model defined by [1]
l_e, l_p	Slip-line lengths in ploughing force model defined by [1]
df_c	Total differential cutting force
df_t	Total differential thrusting force
$df_{r,cut}, df_{t,cut}, df_{a,cut}$	Differential radial, tangential, and axial cutting forces
df_{ind}	Differential indentation force
p_e	Elastic contact pressure
p_p	Plastic contact pressure
E	Workpiece elastic modulus

σ_y	Workpiece yield strength
ν	Poisson's ratio
r_e	Cutting edge radius
x	Projected distance along the cutting edge flank face
x_0	Projected length of initial contact of the indentor
x_1, x_2	Transition locations between elastic and plastic pressure
b	Total projected length of the indentor
C	Plastic flow constant
$y(x), y_1$	Parameters defined explicitly by [2]
$\overrightarrow{v_r}, \overrightarrow{v_t}$	Cutting edge point radial and tangential velocity
$\overrightarrow{e_3}$	Standard basis vector
$\overrightarrow{n_z}$	Unit vector in tool axis direction
$\overrightarrow{n_t}$	Unit vector in tool tangential velocity direction
χ	Magnitude ratio between cutting edge point radial/tangential velocity
μ	Indentation model weighing function
c_0	Indentation model weighing function sensitivity parameter
df_r, df_d, df_a	Differential total radial, tangential and axial force components
$df_x \quad df_y \quad df_z$	Differential X- Y- and Z- force in global workpiece frame
$F_x \quad F_y \quad F_z$	Total force acting on the tool in X-, Y- and Z- directions

Chapter 1

Introduction

1.1 Background and Motivation

Recent trends towards miniaturization have driven the development of a wide range of micro-/nano-scale technology [3]. In particular, micro-ball end milling has emerged as a viable option for many applications requiring the manufacture of non-silicon parts with micron-scale tolerances [4-6]. Five-axis machining has been shown to be a versatile manufacturing process capable of creating a wide range of three dimensional complex surface geometries with high aspect ratios [7]. In addition, the two rotary degrees of freedom increase feature accessibility such that parts can be machined in a single setup without the need for re-fixturing, thus reducing cycle times [6, 8, 9]. However, premature tool failure has been found to be a major challenge in micro-ball end milling due to induced machining stresses that can easily exceed tool strength [10]. Thus, modelling of force generation during micro-ball end milling process is essential for determining appropriate machining conditions. A comprehensive force model can also facilitate process parameter optimization and force-based tool path generation [11].

Force modeling in macro-scale end milling has been intensely studied as the cutting force is considered to be directly related to the chip thickness [12-15]. However, as the conventional macro-scale end milling is scaled down to micro-level, the scale of cutting conditions are dropped from ~feed rate of 100μm/flute and depth of cut (DOC) of ~1mm to

feed rate of ~1μm/flute and depth of cut < 100μm. In macro scale, the cutting edge radius is often considered negligible compared to the chip thickness generated in the process. However, due to limitation of tool-making process and tool material property, the ratio between chip thickness and cutting edge radius becomes significantly larger in micro-scale machining, as the cutting edge in micro-end mills are around 2μm, which is on the same scale as the chip thickness. The difference in chip thickness/ edge radius ratio will cause the chip generation process and force generation in micro-end milling to be drastically different than the process in macro-scale end milling. In micro-scale, the chip formation depends on the chip thickness: when the chip thickness is above a certain level called the minimum chip thickness (MCT) [1, 16], chips will be formed and the cutting force generation is dominated by shearing effect similar to the macro-scale machining. However, when the chip thickness is below MCT, instead of forming a chip, material will be ploughed towards the cutting direction, such that the cutting force is contributed by ploughing effect. The difference between ploughing and shearing regime causes nonlinearity in the chipload/cutting force relationship, thus the force models developed for macro-scale end milling cannot be directly used for micro-end milling force predictions. Hence, a force model that considers both the shearing and ploughing force is essential to the micro-end milling force prediction.

In order to accurately predict the cutting force, the chip thickness in end milling operations needs to be precisely calculated. Shown in Fig. 1.1, a helical ball end mill has cutting edges that lie on the surfaces of a hemisphere. Therefore compared to a flat end mill, the ball end mill has cutter flutes that have constantly changing cutting edge geometry along the axis of the tool. Hence, the chip thickness calculation for ball end mill is considered more complex. Previous approaches have been done to calculate chip thickness in ball end mill for in-plane tool movements [17, 18]. However, as shown in Fig. 1.1, ball end mill operations in

five-axis environment often include various tool-workpiece inclination angles. Therefore, a different approach is needed for five-axis ball end mill chip thickness calculation. In addition, tool runout conditions are proven to be significantly affecting chip thickness generation in micro-end milling [1], this adds another complexity to the micro-ball end milling chip calculation. Hence, a comprehensive chip thickness calculation that considers ball end mill geometry, different tool orientations and runout conditions is in need for reasonable force prediction in five-axis ball end milling.

The cutting force generated by micro-ball end milling is not always contributed entirely by the shearing and ploughing force. The generation of shearing or ploughing force needs the relative tangential movement between the ball end mill cutting edge and the workpiece. However the tangential speed is very small or zero in the tool tip area of the ball end mill. Such portion of the tool often experiences radial movement towards the workpiece, and generates considerable amount of force due to such movements. For instance, the cutting force exerted on the ball end mill with tool orientation and feed direction relative to the workpiece shown in Fig. 1.1 is significantly contributed by the indentation of the rigid tool cutting edge [2]. Hence, in order to predict the extra cutting force for such five axis tool movements, the inclusion of an indentation force model is desired in the cutting force model.

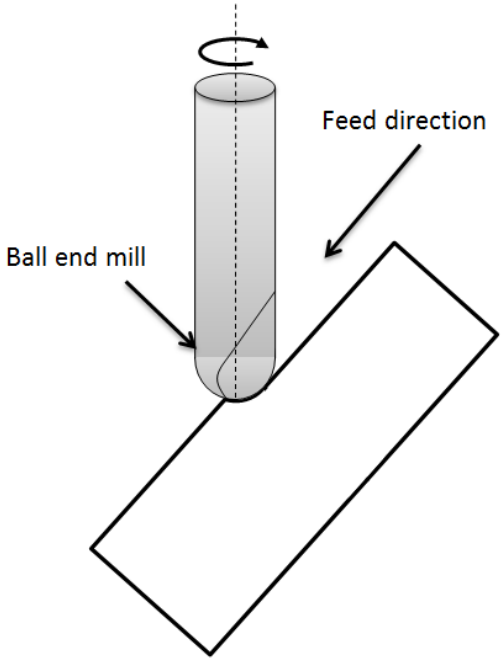

Figure 1.1 Illustration of a ball end mill performing machining with plunging movement

1.2 Research objectives, Scope, and Tasks

The objective of this research is to develop a five-axis ball end mill force model that is specifically tailored to micro-scale machining. A novel chip thickness algorithm that captures complex tool trajectories experienced during five-axis milling will be implemented based on the velocity kinematics of the tool. This unique framework allows both runout effects and elastic recovery generated during ploughing to be easily incorporated within chip thickness calculations. To capture tool-workpiece engagement, a workpiece updating algorithm will be introduced. As a dual purpose, the algorithm stores historical elastic recovery locally on the workpiece surface while retaining its directionality. Then, a composite force model that combines shearing/ploughing contributions from a slip-line field framework with indentation forces attributed to plunging effects will be presented. To validate this force model, a set of micro-five-axis ball end mill testing will be performed and compared to model simulations of various cutting conditions. Finally, the composite model application of ball end milling

process planning will be illustrated.

This research considers the cutting tool to be completely rigid, thus will not cover the effects of dynamic process faults including tool vibration and extra tool runout due to rotary inertia, gyroscopic movements and shear deformation in order to concentrate on the static model development. The heat generation, temperature effect and workpiece grain size effect will not be covered in this research since these concepts do not significantly affect the force generation and is more important to tool wear.

The research objective will be achieved by the following specific tasks:

- Chip thickness algorithm development: The chip thickness algorithm for micro-ball end milling that is based on a novel discretization of the ball end mill cutting flute, and created by the velocity kinematic of the tool cutting edge points. The resulting chip thickness is in form of vectors such that both direction and magnitudes are recorded. The framework created by this algorithm enables runout condition simulation as well as the historical chip thickness recording.
- Workpiece updating algorithm development: The workpiece updating algorithm is developed to capture the complex tool-workpiece engagement condition in five-axis ball end milling environments. The 2-D workpiece model is also designed to store both directions and magnitudes of historical chip thickness for future cutting edge passes.
- Development of composite cutting force model: The cutting force model is developed as a weighted component of two parts, a slip-line cutting force model that computes shearing/plunging force and a quasi-static tool indentation model that predicts tool force generated by cutting edge radial indenting into the workpiece. The

weighting function is developed to distribute force calculated from both models on the basis of the cutting edge radial/tangential velocity ratio.

- Calibration and validation of the composite cutting force model: The slip-line model component and the indentation model component are individually calibrated through specifically designed cutting experiments. The runout condition is then validated through runout measurement and experiment/ model simulation comparison. Finally, the composite force model is validated thought experiments with various five-axis cutting conditions.

1.3 Thesis outline

The remaining content of this thesis is organized as follows.

In Chapter 2, a review of literature that is relevant to the topic of this thesis is presented. First, to provide fundamental knowledge's of this thesis work, basic force modelling for conventional macro-scale end milling is discussed, followed by process modelling of in-plane macro-scale ball end milling. Then, to distinguish the concept of five-axis process modelling from the conventional three-axis modelling, ball end milling modelling efforts in five-axis machining condition as well as special chip thickness modelling in five-axis ball end milling are presented. Further, the concept of micro-scale force modelling is presented, starting with effects of minimum chip thickness and elastic recovery, followed by review on relevant work on micro-scale ball end mill modelling. Next, several important modelling examples that contributes to the work in this thesis, including slip-line modelling, runout modelling and indentation force modelling are specifically discussed. Finally, the gap in present knowledge that inspired this research is discussed.

In Chapter 3, steps of the five-axis micro-ball end mill force model development will be

explained. Starting from constructing the ball end mill geometry model, detailed coordinate transformations that enable model interaction between the tool and the workpiece will be presented. A novel chip thickness algorithm specifically designed for five-axis ball end milling will be explained next. This will be followed by the development of the tool and workpiece interaction model that enable both the tool registration and historical chip thickness storage is presented. For the force modelling section, a slip-line model that takes into account two cutting mechanisms in micro-machining is presented, followed by the introduction of tool indentation force model, which serves as a model supplement when the slip-line model failed to fully predict plunging force. At last, a composite model that automatically adjusts the weighting factor between the slip-line model and indentation model is presented.

Chapter 4 presents both the calibration and validation processes of the composite force model. First, an experimental test bed for both calibration and validation is introduced. Individual components of the composite force model, i.e. slip-line force model and indentation model are separately calibrated using specifically designed experiments that isolate each of the force effects. The runout model is also validated through experiment. Lastly, the composite force model is comprehensively validated across multiple cutting conditions that represent typical five-axis movements.

Chapter 5 demonstrates a possible model application to improve tool life and reduce machining cost. It shows that by using pre-generated force prediction results, the force model is potentially able to help schedule the real time feed rate and tool positions to avoid large tool forces. Two examples of process planning for ball end mill is presented and simulation has shown that the proposed strategies are able to reduce risk of encountering high force during machining, thus achieving the goal of prolong tool life.

Chapter 6 presents conclusions of this thesis. Recommendations for future research are also given.

Chapter 2

Literature Review

In this chapter, the background of existing research that related to the development of a 5-axis micro-scale ball end mill force model is presented. The chapter presents the overview of conventional macro-scale ball end milling force model development, including chip thickness calculation, in plane mechanistic force modelling approach and ball end milling geometry modelling. Secondly, research on five-axis end milling that incorporates different tool trajectory, tool orientation and tool-workpiece interaction positions is discussed. Existing research on unique micro-machining effects during end milling, including effects of minimum chip thickness (MCT) and elastics recovery due to larger tool cutting edge radius to chip thickness ratio, as well as runout effect are discussed. Research that focus on combining ball end milling modelling and micro-machining effects, such as effects of cutting edge indentation to the excreting tool force is summarized next. Finally, a summary of knowledge gaps between exiting relevant studies that lead to this research is presented.

2.1 Macro-scale five-axis ball end milling force model development

In the past, macro-scale ball end mill force models based on a mechanistic relationship between cutting force and chip load have been explored by several researchers [5, 8, 9, 18] . These models discretize the ball end mill into a series of disks and describe in fairly rigorous detail the ball end mill geometry and chip thickness calculation. In order to provide a general foundation of knowledge that helped the development of the model in this thesis, research on

conventional end mill force model and ball end mill geometry is discussed.

2.1.1 Macro-scale flat end mill mechanistic force model

The most common way to predict cutting force in machining operation involving shear cutting is the mechanistic approach force modelling. Multiple models have been developed towards prediction of end milling force [12, 13, 19]. Mechanistic models are based on the assumptions that the normal dF_n and friction dF_f forces generated by machining are directly related to the chip thickness through scalar multipliers call specific energies.

For the purpose of discrete computation, the flat end mill is discretized into angles, flute and axial segments [13]. According to [19], when a chip with thickness t_c is formed, the force generated on each individual cutting edge segment that is on i^{th}disk, j^{th}flute and k^{th}angle are calculated as

$$dF_n(i,j,k) = K_n t_c(i,j,k)dz$$
$$dF_f(i,j,k) = K_f t_c(i,j,k)dz \quad (2.1)$$

Where K_n and K_f are called specific cutting energy and specific friction energy, respectively. dz is the thickness of each disk element. The values of K_n and K_f can be determined by performing calibration experiments for a range of cutting conditions and cutting edge geometries [14], and are considered highly dependent on chip thickness t_c, linear cutting speed V and nominal rake angle α_n, In three-dimensional space, K_n and K_f can be used to calculate the oblique tangential force F_t, radial force F_r and axial force F_a through local helix angle λ and chip flow angle η.

Once dF_n and dF_f are calculated for each cutting edge segment, they can be transformed into forces in global X-Y-Z- coordinates and integrated as total forces $F_X$and F_Y by

$$F_X = \sum_{i=1}^{N_{\max}(i)} \sum_{j=1}^{N_{\max}(j)} \sum_{k=1}^{N_{\max}(k)} (-dF_r(i,j,k)\cos\theta(i,j,k)) +$$

$dF_t(i,j,k)\cos\theta\,(i,j,k))$(2.2)

$$F_Y = \sum_{i=1}^{N_{\max(i)}} \sum_{j=1}^{N_{\max(j)}} \sum_{k=1}^{N_{\max(k)}} (-dF_r(i,j,k)\sin\theta(i,j,k)) - dF_t(i,j,k)\cos\theta\,(i,j,k)),$$

where $\theta(i,j,k)$is the k^{th} rotated angular position. The resulting total global force $F_X$and F_Y can then be used to validate the mechanistic model by comparing the simulation result to the experimental result gain by X- and Y- directional force sensor placed underneath the workpiece.

However, the precise prediction of instantaneous chip thickness $t_c(i,j,k)$ is essential to the computation of $F_X$and F_Y. According to [15], regarding a flat end mill, without consideration of process faults including runout and tool dynamics, the chip thickness in each cutting edge point for each tool pass is simply calculated as

$$t_c(i,j,k) = f_t \sin\theta(i,j,k), \qquad (2.3)$$

where f_t is the feed rate per flute.

The semi-empirical mechanistic model is being widely successful in conventional macro-scale end mill force prediction since it is calibrated by experiment, and can avoid complex analytical efforts toward material behaviour and geometry of the shear zone [9].

2.1.2 Mechanics of ball end mill machining

Due to the versatile nature and its ability to machine complex free-form surfaces, ball end mill is getting high interest among industries. Therefore the mechanics of in-plane ball end mill operation has been widely studied in the past [17, 20, 21]. Due to the spherical ball end mill surface, the helix angle and tool radius is variable along the tool axis. Yang et. al.[21] suggests that the ball end mill cutting edge can be discretised as a series of small elements, and oblique cutting process in each of the cutting edge segment is analysed individually as an orthogonal cutting model. Lee et. al. [17] has extended this model to include mechanistic

model in which force coefficients can be calibrated against experiment data.

A detailed geometry and coordinate system of a helical ball end mill cutting edge is presented by Lee et. al. [17]. Showing in Fig. 2.1, the origin of the X-Y-Z coordinate is located on the ball end mill tool tip, and the ball part geometry expression is given by

$$x^2 + y^2 + (R_0 - z)^2 = {R_0}^2 , \tag{2.4}$$

where R_0 is the ball radius of the sphere C. The variable cutter radius in X-Y plane and height z is $R(z)$, and is calculated as

$$R^2(z) = x^2 + y^2 . \tag{2.5}$$

With ψ being the lag angle between the line connecting cutting edge point and tool centre point C and the Z-axis, i_0 being the nominal helix angle on the tool shaft, and $i(\psi)$being the local helix angle on the cutting edge that has lag angle ψ, the following relationships are given by [17],

$$z = \frac{R_0 \psi}{\tan i_0}, \tag{2.6}$$

$$\tan i(\psi) = \frac{R(\psi)}{R_0} \tan i_0. \tag{2.7}$$

Thus the local cutter radius is expressed as

$$R(\psi) = \sqrt{1 - (\psi \cot i_0 - 1)^2}. \tag{2.8}$$

The infinitesimal curved cutting edge segment dS is then given by

$$dS = \sqrt{(R'(\psi))^2 + R^2(\psi) + {R_0}^2 \cot^2(i_0)}\, d\psi, \tag{2.9}$$

where $R'(\psi)$ is derived by

$$R'(\psi) = \frac{-R_0(\psi \cot i_0 - 1)\cot i_0}{\sqrt{1-(\psi \cot i_0 - 1)^2}}. \tag{2.10}$$

Thus in the tool polar coordinate system, a point on flute j and with height z is indexed by its angular position $\psi_j(z)$, with $\varphi_p = 2\pi/N_f$ being the cutter pitch angle and θ being the

flute rotation,

$$\psi_j(z) = \theta + (j-1)\varphi_p - \frac{z}{R_0}\tan i_0 \tag{2.11}$$

Therefore with feed rate f_t during orthogonal cutting, the chip thickness normal to the cutting edge is a function of cutting edge point location described by ψ, θ and axial angle κ, thus

$$t_c(\psi, \theta, \kappa) = f_t \sin\psi \sin\kappa, \tag{2.12}$$

where

$$\kappa = \sin^{-1}\frac{R(\psi)}{R_0}$$

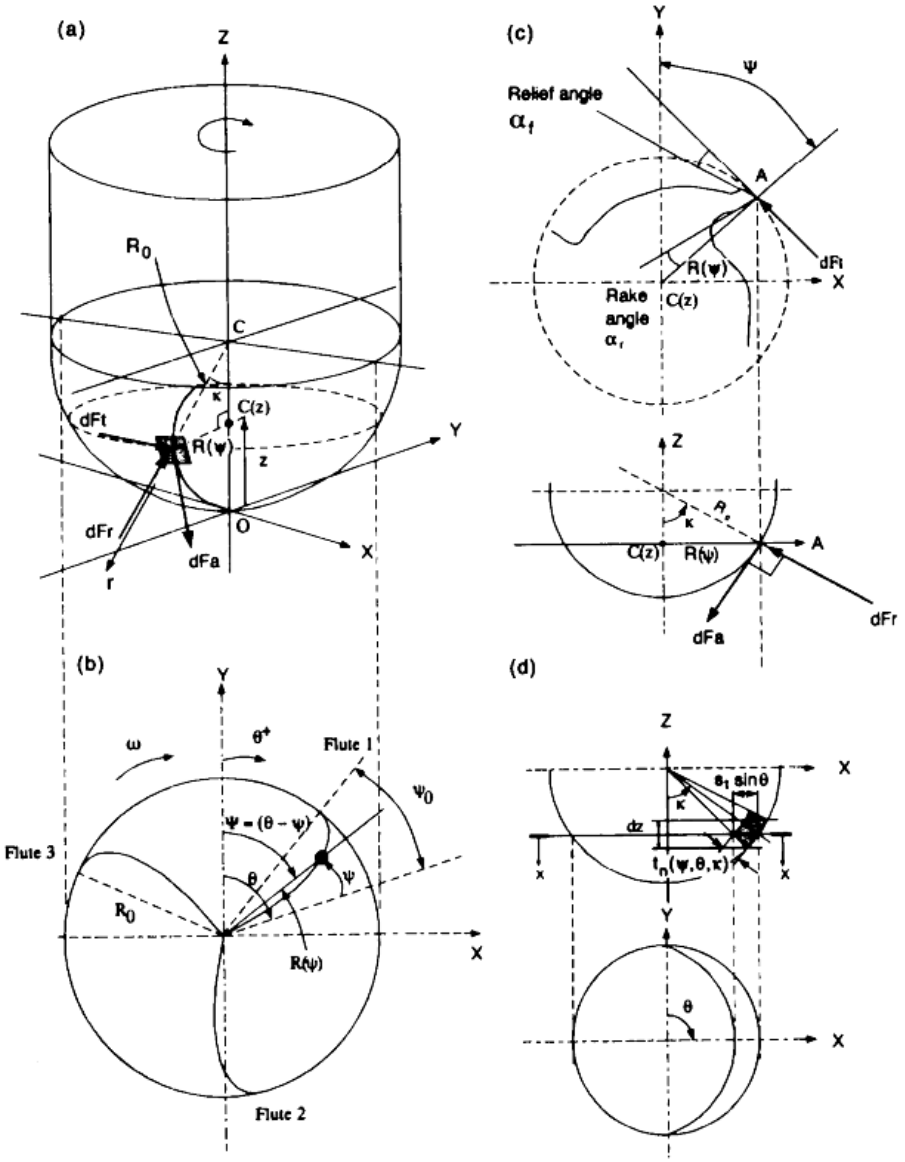

Figure 2.1 Geometry and tool coordinates for a ball mililng cutter [17]

Alghout the theoretial chip thickness model is relatively accurate in most part of the cutting edge, Lee et. al.[17] has pointed out that the error generated around the ball tip area is significant. However due to the negaligibal force genetaion on the tool tip area during orthogonal cutting, the error around this area does not effect force prediction significantly.

The same mechanistic force model introduced in 2.1.1 was used on the ball end mill condition, but due to the spherical shape of the flute, the tangenrial, radial and axial force to

X-Y-Z coordinate transformation is updated to

$$\begin{bmatrix} dF_x \\ dF_y \\ dF_z \end{bmatrix} = \begin{bmatrix} -\sin(\kappa)\sin(\psi) & -\cos(\psi) & -\cos(\kappa)\sin(\kappa) \\ -\sin(\kappa)\cos(\psi) & \sin(\psi) & -\cos(\kappa)\cos(\kappa) \\ \cos(\kappa) & 0 & -\sin(\kappa) \end{bmatrix} \begin{bmatrix} dF_r \\ dF_t \\ dF_a \end{bmatrix} \tag{2.13}$$

Therefore for orthogonal cutitng condition, the total X-, Y- and Z- cutting force generated by the ball end mill depth of cut z is

$$\begin{bmatrix} F_x \\ F_y \\ F_z \end{bmatrix} = \int_0^z \begin{bmatrix} dF_x \\ dF_y \\ dF_z \end{bmatrix} \tag{2.14}$$

Note that the above force model is only suitable for orthogonal cutting prediction due to the inability to distinguish tool and workpiece engage condition if the tool is tilted relative to the workpiece surface. The lack of chip thickness calculation accuracy around the tool tip will also affect force prediction result if the tool is doing plunging movement and the tool tip area is experiencing large force.

To enable the possibility of modelling five-axis tool movement for ball end mill where the tool is not always orthogonal to the workpiece surface, a tool-workpiece engagement algorithm is needed. The following section discusses the research that relate to five-axis ball end mill modeming.

2.2 Five-axis ball end milling model

The foundational modelling approaches taken in past literature have led to moderately accurate force predictions, but are limited to in-plane tool movement, and simple flat workpiece surfaces. Five-axis machining, on the other hand, introduces a greater variety of possible tool trajectories and workpiece surfaces. In a recent study performed by Fard et al. [22], tool orientation in five-axis micro-ball end milling has been shown to not only affect cutting forces, but also alter surface morphology of the machined surface. In attempt to

capture the effects of tool orientation on the machining process, five-axis cutting force models developed by Lazoglu et al., Zhu et al. and Sonawane et al. [8, 9, 23]have extended the basic ball end milling models to include tool orientation, varying cutting depths, and complex tool-workpiece contact area by developing versatile tool/workpiece engagement models and chip thickness generation models.

2.2.1 Tool-workpiece engagement models

The tool-workpiece engagement model serves the dual purpose of determining real time chip thickness in every part of the cutting edge, as well as updating the workpiece after a flute sweep and prepare for the next flute. Multiple approaches has been done to model the tool-workpiece engagement. Lazoglu et. al.[8] developed a boundary representation based contact workpiece engagement (CWE), based on 3-D modelling of the tool and workpiece. CWE used Boolean operations to determine the cutter/workpiece engagement condition by considering the tool as a spherical surface. Shown in Fig. 2.2, the tool tip has been discretized into disks along the tool axis, and the tool-workpiece engagement on the tool is determined by the start and exit angle for each discrete disks on the tool. The cutting force is calculated independently on each disks depending on the engagement angle along with the corresponding depth of cut and summed up. The workpiece surface is updated by mathematically removing the volume swept by the tool movements.

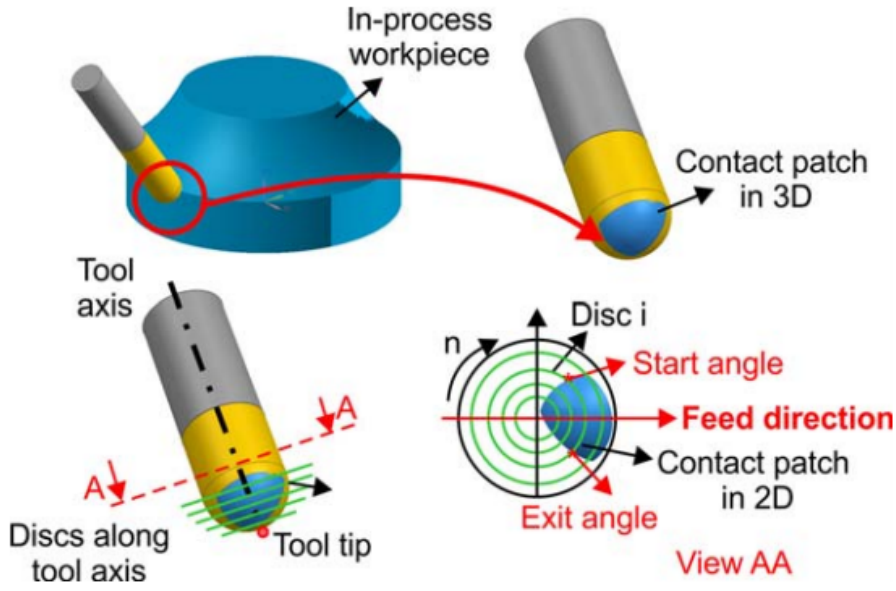

Figure 2.2 Cutter-workpiece engagement geometry extraction[8]

Zhu et. al. [9] has presented a more numerical way of modelling the workpiece and ball end mill cutting edge. In this work, the complex workpiece surface is modelled by a matrix of variable Z values on the X-Y plane. The X-Y plane is represented by a uniform grid mesh with constant intervals a and b in X- and Y- directions respectively. Shown in Fig. 2.3, The height of any point S that fall into the space that connected by four neighbouring lattices $S_{q,r}$, $S_{q+1,r}$, $S_{q,r+1}$ and $S_{q+1,r+1}$can be interpolated using the following Lagrangian basis function:

$$z(S) = N_1(\Delta x, \Delta y) \cdot z\left(S_{q,r}\right) + N_2(\Delta x, \Delta y) \cdot z\left(S_{q+1,r}\right) + N_3(\Delta x, \Delta y) \cdot z\left(S_{q+1,r+1}\right) + N_4(\Delta x, \Delta y) \cdot z(S_{q,r+1}), \quad (2.15)$$

where Δx and Δy are the distance from S to $S_{q,r}$in X- and Y- directions, and the $N_i(\Delta x, \Delta y)$ are called basis functions that expressed as:

$$N_1(\Delta x, \Delta y) = 1 - \frac{\Delta x}{a} - \frac{\Delta y}{b} + \frac{\Delta x \cdot \Delta y}{ab}$$

$$N_2(\Delta x, \Delta y) = \frac{\Delta x}{a} - \frac{\Delta x \cdot \Delta y}{ab}$$

$$N_3(\Delta x, \Delta y) = \frac{\Delta x \cdot \Delta y}{ab}$$

$$N_4(\Delta x, \Delta y) = \frac{\Delta y}{b} - \frac{\Delta x \cdot \Delta y}{ab} \tag{2.16}$$

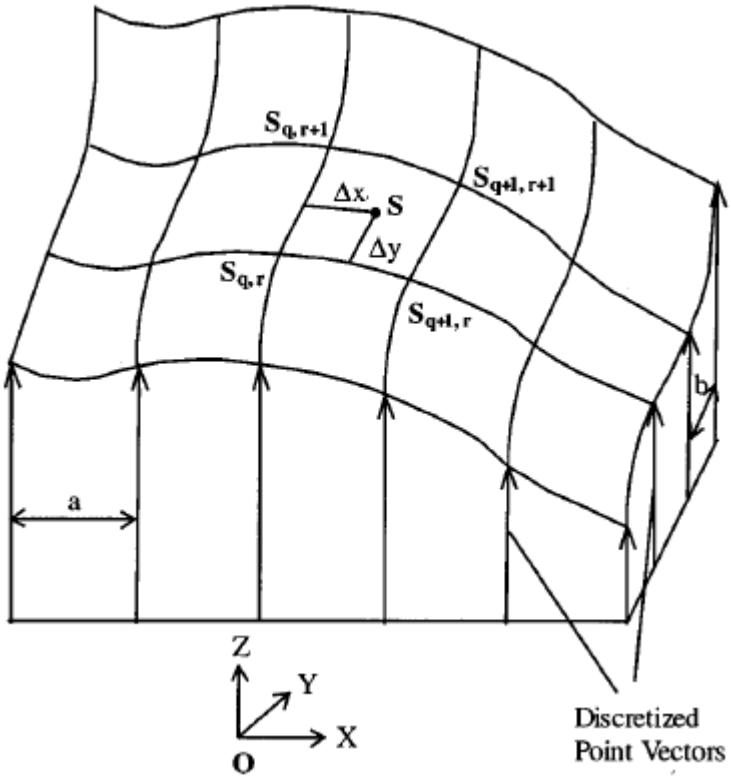

Figure 2.3 Representation of workpiece surface modeling [9]

With the workpiece surface model developed, the cutting edge engagement algorithm can be achieved when combining previously developed cutting edge models. As shown in Fig. 2.4, following the ball end mill cutting edge geometry presented in Sec. 2.1.2, the X-Y- and Z- coordinates on every points of the cutting edge can be transformed into the workpiece coordinate frame. The Z- heights on each cutting edge point can then be compared to the Z-height on the workpiece surface that has the same X- and Y- coordinates. Tool/workpiece engagement will be determined by if the cutting edge point has a Z- value that is lower than the workpiece height. The radial depth of cut of the tool can be calculated as the difference between the tool Z- coordinate and the workpiece Z- coordinate if the engagement happens.

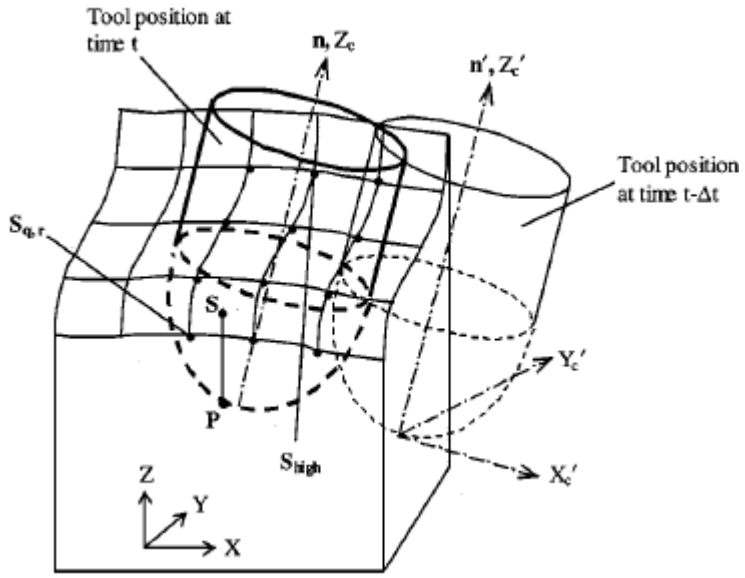

Figure 2.4 Cutting engagement with repsect to workpiece

The engagement of tool and workpiece will result in deformation of the workpiece surface, as the sweep of one pass of the flute cannot re-engage with the workpiece material that has been removed by previous flutes. Zhu et al. [9] has provided the solution of checking the distance D between current cutting edge location and the tool centre in the previous tool movement, and compare it to the tool radius R. If $D > R$ was found for any of the cutting edge points, this portion of the cutting edge is outside of the previous tool envelope and thus able to engage with the workpiece again.

The basis of tool-workpiece model has enabled the five-axis ball end mill model to calculate real time cutting conditions in complex tool geometry and workpiece surface conditions. However, the chip thickness model in five-axis condition should also be updated due to the inability of inclined tool chip prediction by the conventional in-plane ball end mill cutting force model.

2.2.2 Five-axis ball end milling chip thickness model

Chips generated by inclined tool cutting on complex workpiece surface are significantly different from ones generated by in-plane orthogonal cutting. Therefore a comprehensive chip thickness model for five-axis ball end milling is essential to accurate cutting force prediction. Multiple approaches have been used in previous works to predict the chip thickness in five-axis ball end mills [8, 9, 23]. This section presents works that have developed chip thickness models that are suitable for varying tool orientation and feed direction conditions.

Lazoglu et al. and Sonawane et al. [8, 23] has modelled the instantaneous chip thickness in five-axis condition with rather similar approach to the in-plane chip calculation presented in Sec. 2.1.2, but with consideration of tool orientation angles as well as horizontal and vertical feed components of the tool. Chip thickness in this model is also calculated on individual discrete disk elements on the ball end mill. By introducing the feed inclination angle α, the chip thickness is analytically obtained as the sum of two components: the chip thickness generated by tool horizontal movement and the one generated by tool vertical movement.

$$t_c = f_t \times \sin(\theta) \times \sin(\psi) \times \cos(\alpha) \pm f_t \cos(\psi) \sin(\alpha). \qquad (2.17)$$

While this analytical chip thickness is easy to calculate, but is rather limited to ideal cutting conditions where no process faults are present. Zhu et al. [9] has instead presented a numerical chip thickness calculation approach that utilized the relative instantaneous cutting edge distance over a discretized time period. Shown in Fig. 2.5, let $P(z_c, \theta, j)$ equals the distance between the current tool centre C and the cutting edge point P on height z_c, rotation angle θ and the flute j, while $P'(z_c, \theta, j)$ equals the portion of CP that is beyond the tool envelope in the previous time step. Thus the chip thickness in the current time step is:

$$t_c(z_c, \theta, j) = |P(z_c, \theta, j) - P'(z_c, \theta, j)|. \quad (13)$$

One of the advantage of numerical chip thickness model is that it can incorporate process faults such as runout and tool deflection, since such extra tool movements can be added on top of the instantaneous cutting edge locations according to [9].

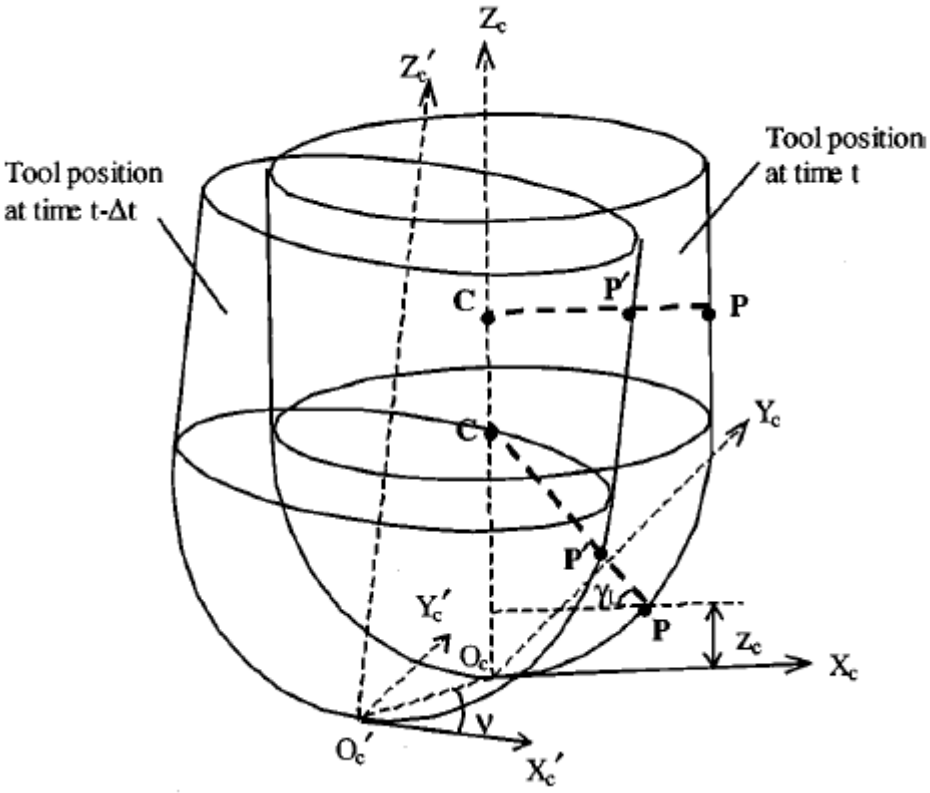

Figure 2.5 Determination of undeformed chip thickness [9]

Due to often negligible cutting edge radius effect in macro scale ball end milling, the versatile five-axis ball end milling mechanics along with tool inclination incorporated chip thickness model can provide fairly accurate force predictions. However, in micro-scale machining, as the ratio between tool edge radius and chip thickness become significantly larger, the uniqueness of workpiece chip forming behaviours will cause the macro-scale force model not directly applicable. Therefore new models tailored for micro-scale ball end milling is in need. predictions.

2.3 Micro-scale ball end milling force model development

At the micro-scale, there are a number of fundamental differences in the cutting mechanisms that prevent the direct application of the macro-scale ball end milling force models. First, the relatively large cutting edge will lead to increasing importance of the ploughing force, as minimum chip thickness effect plays an important role in force predictions. When unreformed chip is lower than the minimum chip thickness, no chip will be formed as the material will be ploughed and generate different cutting and thrusting force along the process. Second, effects of tool runout will be enlarged in micro-cutting conditions due to inevitable relatively large set up error in micro-machining. Last but not least, previously less important cutting edge indentation force is contributing considerable amount of additional force in micro-ball end milling. This section covers previous research that concentrates on above topics that enabled micro-ball end milling force predictions.

2.3.1 Effects of minimum chip thickness and elastics recovery

One important characteristic of micro-end milling is the relative significance of the cutting edge radius [1, 4, 24, 25]. As the uncut chip thickness approaches the size of the cutting edge radius, the cutting process transitions from a shearing-dominated regime to a ploughing-dominated regime. This transition occurs at a condition known as the minimum chip thickness (MCT) [1, 16]. Below the MCT, the machining process is characterized primarily by elasto-plastic deformation, as opposed to chip formation. In this cutting regime, material deformation is followed by elastic recovery, thereby introducing a historical dependency on chip thickness.

The effect of minimum chip thickness is illustrated in Fig. 2.6. When the uncut chip thickness is below the minimum chip thickness as shown in Fig. 2.6-(a), no removable chip

will be formed, and the workpiece surface after the cut will partially recover due to elastic recovery effect of the workpiece material. Force generation in this condition is dominated by ploughing mechanism. If the uncut chip thickness is greater than the minimum chip thickness as shown in Fig. 2.6-(b), a chip will be formed, thus shearing mechanism will contribute to the major part of force generation. However as the relatively large cutting edge radius, ploughing effect will also generated considerable amount of force.

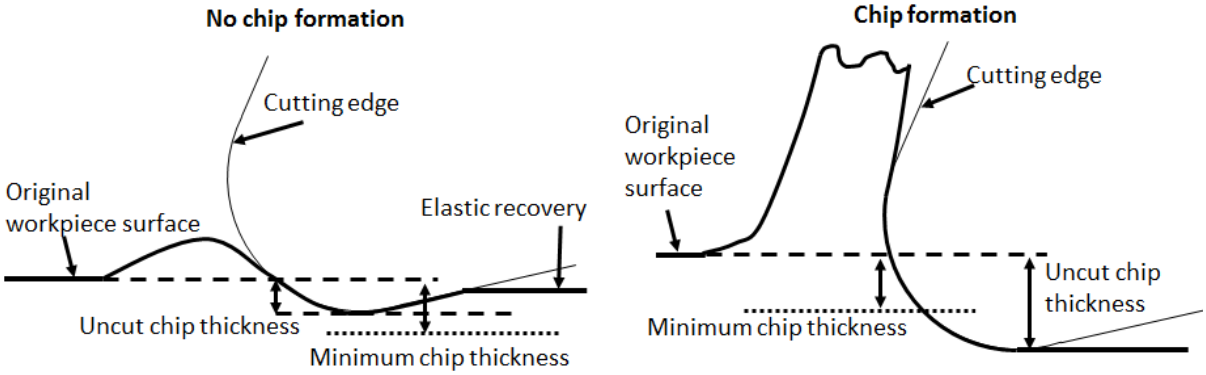

(a) (b)

Figure 2.6 Illustration of orthogonal cutting process with (a) no chip formation and (b) chip formation

Yuan et al. [24] has investigated the minimum chip thickness effect through diamond tool experiments, and discovered that chip will not be formed if the diamond tool has chip thickness lower than a certain amount. Through cutting with different edge radius, the minimum chip thickness was found to be approximately 30% of the edge radius. Liu et. al. [25] discovered that the minimum chip thickness effect is critical to the cutting force generation, as the chipload-force relationship shown in Fig. 2.7 suggest that the ploughing effect will cause higher force when chip thickness is right below the minimum chip thickness boundary.

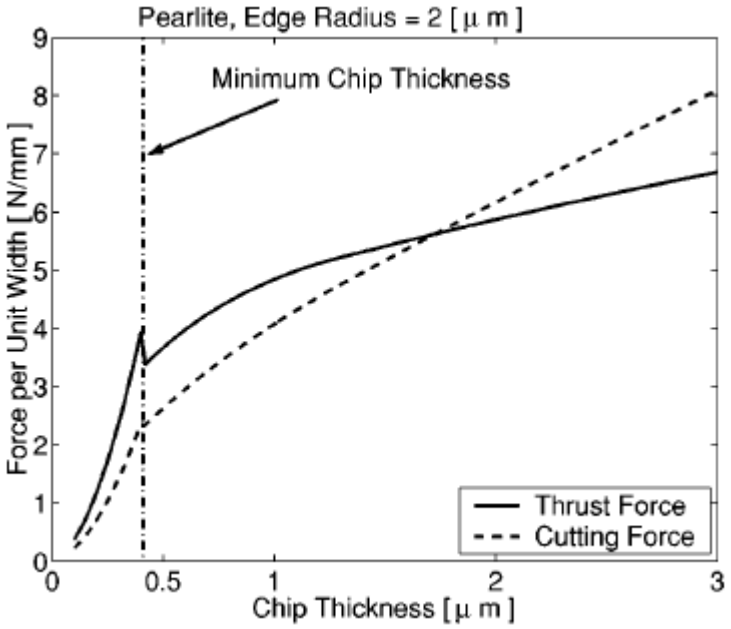

Figure 2.7 Chipload.force relationship for pearlite [25]

Vogler et al. [16] has incroporated the minimum chip thickness effect in the micro-scale cutting force prediction model, by assuming the workpiece will fully recover if the uncut chip thickness is below the minimum chip thickness. Therefore the uncut workpiece material will accumulate after number of cutting edge passes until a chip is formed. Liu et al.[4, 25] has proposed the asumption that after a no-chip-formation cut, instead of fully recover, the workpiece material will demonstrate plasto-elastic behavior and only partially recover.

2.3.2 Micro-scale in-plane ball end milling

Recent developments in machining literature [1, 16] address many of the unique process mechanics encountered during micro-scale end milling, however, very limited research has been specifically done on micro-scale ball end mill force modelling. The most relevant work was performed by Malekian et al. [5], who implemented a mechanistic-based force model by decomposing force predictions into shearing-dominated and ploughing-dominated components.

The micro-ball end mill chip thickness calculation in [5] has incorporated the concept of historical chip thickness, which is formed by the partial recovery of the workpiece material after previous cut. Shown in Fig. 2.8, when feed rate is down to a certain level, part of the flute path will fall into ploughing regime and produce historical chip thickness. When the next flute begins to engage the workpiece material, the total chip thickness will include historical recovery left by the previous flute pass. As the rotational angle proceeds, chip thickness will drop after the boundary degree θ_{er}, which is the end of previous workpiece recovery formation.

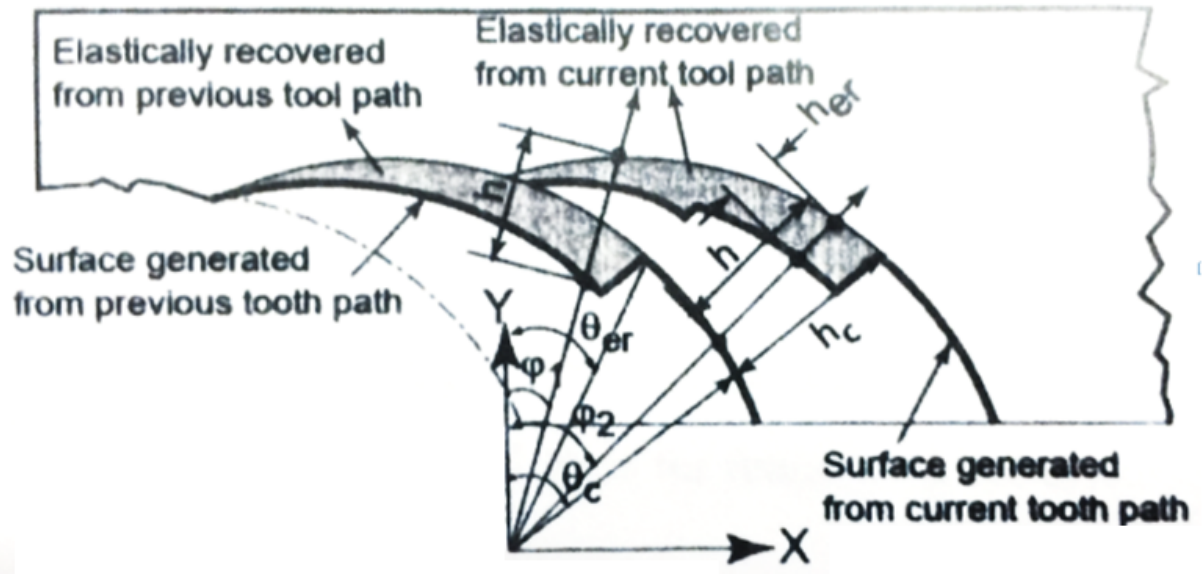

Figure 2.8 Chip thickness in micro-ball end milling [5]

According to [5], by denoting chip thickness as h, minimum chip thickness as h_c, and historical chip thickness as h_p, the chip thickness for flute j and disk i and rotational angle k is expressed as

$$h(i,j,k) = \begin{cases} \left(f_t \sin\left(\theta(i,j,k)\right) + h_p\right) \sin\psi & if\theta \le \theta_{er} \\ f_t \sin\left(\theta(i,j,k)\right) \sin\psi & if\theta > \theta_{er} \end{cases}, \tag{2.18}$$

where

$$\theta_{er} = \sin^{-1}\left(\frac{h_c}{f_t}\right) - \sin^{-1}\left(\frac{f}{R}\sin\left(\frac{\pi}{2} - \sin^{-1}\left(\frac{h_c}{f_t}\right)\right)\right), \tag{2.19}$$

$$h_p(i,j,k) = p_e h(i,j-1,k-\frac{2\pi}{\max(j)d\theta}). \tag{2.20}$$

where p_e is the elastic recovery rate.

When chip thickness is beyond minimum chip thickness, force calculation is referred to the mechanistic model in [17], where the discrete radial, tangential and axial forces on each differential flute element are calculated as:

$$\begin{aligned} dF_{rs} &= K_{rc}h\big(\theta(i,j,k)\big)dz/\sin\psi + K_{re}dS, \\ dF_{ts} &= K_{tc}h\big(\theta(i,j,k)\big)dz/\sin\psi + K_{te}dS, \\ dF_{cs} &= K_{ac}h\big(\theta(i,j,k)\big)dz/\sin\psi + K_{ae}dS, \end{aligned} \tag{2.21}$$

where dz is the thickness of the discrete disk section on the tool; K_{rc}, $K_{tc}$and K_{ac} are the cutting coefficients for radial, tangential and axial components, respectively; K_{re}, $K_{te}$and K_{ae} are the edge coefficients for radial, tangential and axial components, respectively.

Once the cutting flute reaches the region where the uncut chip thickness is below minimum chip thickness, the ploughing force becomes dominant. According to [5], for each differential flute element, the ploughing force in radial, tangential and axial directions are expressed as:

$$\begin{aligned} dF_{ps} &= K_{rp}A_p dz/\sin\psi + K_{re}dS, \\ dF_{ps} &= K_{tp}A_p dz/\sin\psi + K_{te}dS, \\ dF_{ps} &= K_{ap}A_p dz/\sin\psi + K_{ae}dS, \end{aligned} \tag{2.22}$$

where K_{rp}, $K_{tp}$and K_{ap} are the radial, tangential and axial components, respectively; A_p is the ploughing area defined by tool geometry and uncut chip thickness. The radial, tangential and axial force on each discrete flute element are then translated to X-Y-Z coordinate using

(2.13) and summed across all the discretized elements to obtain the total force.

After detailed model calibration, the work by [5] is suitable for force prediction in in-plane micro-ball end milling, as it can capture effects of minimum chip thickness and historical chip thickness. Unfortunately, this work is constrained to constant depth, constant feed rate force predictions along a single planar direction, as there is no consideration of tool-workpiece engagement and chip thickness generation in five-axis conditions. The mechanistic-based force model also relies on the accurate estimation of a number of experimentally calibrated cutting coefficients.

2.3.3 Slip-line field force modelling

With the increasing significance of edge radius effects at the micro-scale, the calibration procedure for empirical mechanistic models becomes highly complex. For this reason, analytical slip-line field theory has recently gained greater appeal [1, 26-28] because force predictions do not rely on experimental calibration, but are rather based on geometry analysis and inherent material properties.

The combination of ploughing mechanism and special shear mechanism behaviour in micro-machining has been considered by many researchers [29, 30] the cause of the "size effect", which means increase in specific cutting energy with decrease chip thickness when machining with relatively large radius cutting edges. Nakayama et al. [30] discovered that ploughing force is not the only component during low chip thickness machining through energy balance analysis, and suggested that the differentiate of the effective rake angle from the nominal rake angle (shown in Fig. 2.9) is affecting cutting force generation. Further study on the cause of the size effect has been done by Kountanya et al. [29], who discovered the presence of dead metal cap and raised prow angle ρ (shown in 2.9) during micro-end milling

through high-magnification experiments.

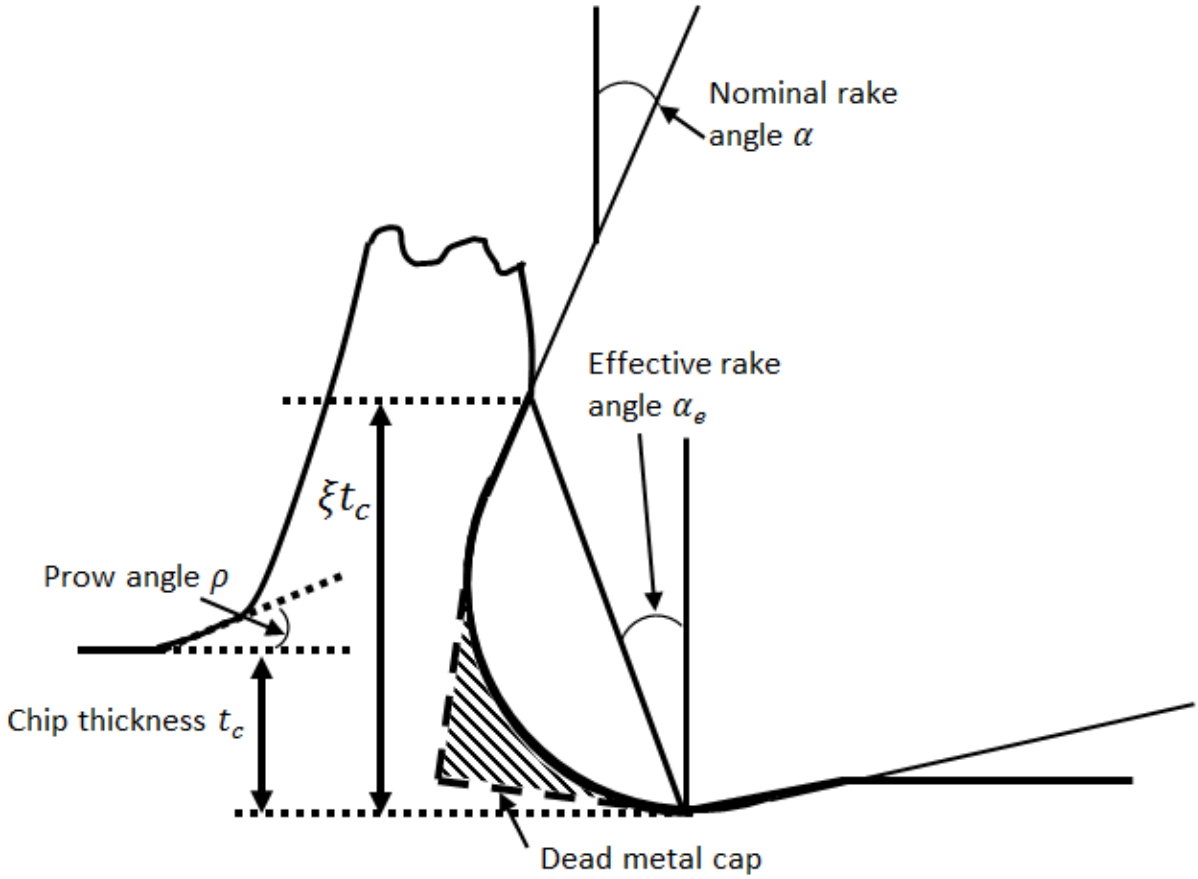

Figure 2.9 Effective rake angle and dead metal cap

Many researchers have suggests that a slip-line force model can capture the micro-scale behaviours analytically [16, 26, 27]. Fang et al. summarized previous studies on slip-line field theories and provided a very detailed theory which suggests that the entire slip-line filed in orthogonal metal cutting consists of three shear zones and 27 sub-regions. Their model is under the assumptions of plane-strain deformation conditions and perfect rigidity of workpiece material. However, no dead metal cap is considered in this model.

When chip thickness is relatively large, cutting force generation are primarily cause by shearing effect. However in cutting conditions where chip thickness is in the similar scale to the cutting edge radius but above the minimum chip thickness, ploughing effect still

significantly changes the cutting force behaviour. Waldorf et al. [26] provided an efficient plane strain slip-line model for orthogonal cutting that included ploughing force prediction when a chip is formed. This model has included the effect of prow angle ρ, and a stable build up region as the dead metal cap.

When chip thickness is below the minimum chip thickness, many researchers has suggested that the cutting tool is closely related to the interference area between the workpiece and the clearance face of the cutting edge [31-33]. Vogler et al.[16] has combined the chip-formation slip-line model by [26] and interference volume model in the no-chip-forming conditions to predict cutting forces in end milling operations. The use of two separate models can account for the non-linearity of the cutting force behaviour when chip load is small. However, this model has assumed that only elastic behaviour will occur on workpiece during ploughing movements, but study on the machined surface formation on ductile material by To et al.[34] suggests that plastic deformation also occurs in small chip thickness machining.

Jun et al.[1] proposed a slip-line model that combine previous models form [16, 26, 27], but added slip-line modelling of the dead metal cap for both chip formation case and non-chip formation case. Workpiece is also considered plastic-elastic during pure ploughing operations in this work, as the surface will partially recover after ploughed by the cutting edge. This model consists of two separate mechanisms that simulate case I: chip formation machining and case II: ploughing/rubbing.

Slip-line force model for case I by [1]:

When chip thickness is larger than the minimum chip thickness, Fig. 2.10 shows the slip-line field as well as the associated hodograph. The dead metal cap formation in this model is under the assumption that material tends to flow parallel to the effective rake angle α_e,

therefore the front face of the dead metal cap AD is also parallel to this direction. It also assumed that other faces of the dead metal cap are tangent to the incoming tool edge.

In Fig. 2, the fan field angles δ and γ are defined as

$$\delta = \phi - \alpha_e - \eta_2, \tag{2.23}$$

$$\gamma = \eta_1 + \eta_2 + \alpha_e - \psi, \tag{2.24}$$

where η_1, $\eta_2$are angles along *AC* and *AD*, respectively, and are defined by the friction factors on these surfaces. $\psi = \sin^{-1}(\sqrt{2}\sin\rho\sin\eta_1)$, ρ is prow angle. The shearing cutting and thrusting forces are then given as:

$$dF_{sc} = kw[(\cos\phi + a_\theta \sin\phi)l_s + (\cos(2\eta_2)\sin\alpha_e + a_2\cos\alpha_e)l_b],$$

$$dF_{st} = kw[(a_\theta\cos\phi - \sin\phi)l_s + (\cos(2\eta_2)\cos\alpha_e - a_2\sin\alpha_e)l_b], \tag{2.25}$$

where w is the width of cut, *k* is the material shear flow stress, $a_\theta = 1 + 2\theta$, $a_2 = (1 + 2\theta + 2\delta + \sin(2\eta_2))$, $\theta = \frac{\pi}{4} - \rho - \phi$, l_s and l_b are the lengths of slip-line DE and AD, respectively, and given as:

$$l_s = \frac{tc - r_e(1+\sin\alpha_e) + h_{prow}}{\sin(\phi)}, \tag{2.26}$$

$$l_b = r_e\tan\psi_r = r_e\tan\left(\frac{\pi}{4} + \frac{\alpha_e - \psi}{2}\right), \tag{2.27}$$

where

$$h_{prow} = \sqrt{2}r_e\sin\rho(\sin\eta_1 + \cos\eta_2)\tan\left(\frac{\pi}{4} + \frac{\alpha_e - \psi}{2}\right), \tag{2.29}$$

The ploughing component in this case is cause by indentation of face AC, therefore the ploughing force can be calculated based on l_b, the length of AC, and are given as:

$$dF_{pc} = kw[\cos(2\eta_1)\cos\psi + a_1\sin\psi]l_b,$$

$$dF_{pt} = kw[a_1\cos\psi - \cos(2\eta_1)\sin\psi]l_b, \tag{2.30}$$

where $a_1 = 1 + 2\theta + 2\delta + 2\gamma + \sin(2\eta_1)$. Therefore the total orthogonal cutting and

thrusting force are calculated as the sum of its shearing and ploughing parts:

$$dF_t = dF_{st} + dF_{pt}, \tag{2.31}$$

$$dF_c = dF_{sc} + dF_{pc}, \tag{2.32}$$

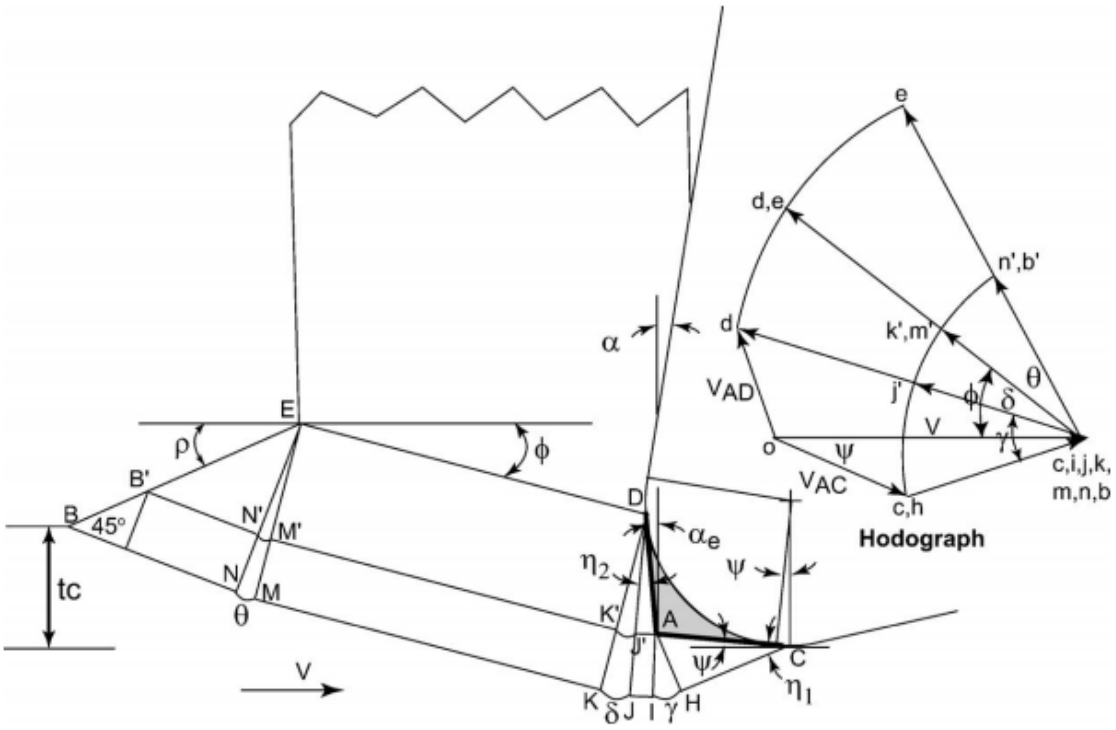

Figure 2.10 Slip-line field for chip formation forces with variable dead metal cap size and its associated hodograph [1]

Slip-line force model for case II By [1]:

In the condition of chip thickness t_c is lower than the minimum chip thickness, several assumptions in Case II has been changed. Shown in Fig. 2.11, first, since no chip formation is occurred, all the workpiece material are assumed to flow under the tool and parallel to the cutting condition, thus $\psi = 0$. Second, the dead metal cap size is considered constant since it is only related to effective rake angle at the minimum chip thickness level. Third, the material

in front of the tool will contact with the tool edge until point *F*, raised by angle ρ_p, and flow down in the direction of AF. In addition, after the material flow over the tool tip area, it will have certain elastic recovery at height κt_c, and apply pressure on the clearance face of the tool along line CG. An additional slip-line component for CG is thereby added to the case II model.

Let the height of point *F* be ξ times of the current chip thickness. The length of AC, l_b is calculated by Eqn. (2.27) but with $\psi = 0$. The angle between the line AF and the vertical line α_p is given as:

$$\alpha_p = -\tan^{-1}\left(\frac{\sqrt{\xi tc(2r_e - \xi tc)} - l_b}{\xi tc}\right). \tag{2.32}$$

The length of AF, l_p, is then given as

$$l_p = \sqrt{2r_e\xi tc + l_b^2 - 2\sqrt{\xi tc|2r_e - \xi tc|}\,l_b}. \tag{2.33}$$

The length of the line CG on the clearance face of the tool, l_e, is found as

$$l_e = \frac{\kappa tc}{\sin(\psi_e)}, \tag{2.34}$$

where

$$\psi_e = \begin{cases} \sqrt{\dfrac{\kappa tc}{2r_e - \kappa tc}} & \kappa tc \le r_e(1 - \cos\gamma_c) \\ \dfrac{\kappa tc \sin\gamma_c}{\kappa tc\cos\gamma_c + r_e(1 - \cos\gamma_c)} & else \end{cases}, \tag{2.35}$$

where γ_c is the clearance angle of the tool. The cutting and thrusting components of the ploughing fore in Case II is then given as:

$$dF_c = kw[(\cos(2\eta_0)\cos\psi_e - e_0\sin\psi_e)l_e - e_1 l_b - \big(\cos(2\eta_2)\sin\alpha_p - e_e\cos\alpha_p\big)l_p]$$

$$dF_t = kw[(\cos(2\eta_0)\sin\psi_e + e_0\cos\psi_e)l_e + \cos(2\eta_1)\,l_b - \big(\cos(2\eta_2)\cos\alpha_p + e_2\sin\alpha_p\big)l_p], \tag{2.36}$$

where

$$e_0 = 1 + 2\delta_r + \sin(2\eta_0)$$

$$e_1 = 1 + 2\delta_p + 2\gamma_p + \sin(2\eta_1)$$

$$e_2 = 1 + 2\delta_p + \sin(2\eta_2), \tag{2.37}$$

where the slip-line fan field angle δ_r is given as

$$\delta_r = \frac{3\pi}{4} - \eta_0 - \psi_e, \tag{2.38}$$

The cutting and thrusting forces for each of the cases are summed together, across discrete cutting flute elements. The same coordinate transformation from Sec. 2.1.1can be done to obtain total cutting force on the tool. In addition, the same force model can be used in ball end mill coordinate transformation presented in Sec. 2.1.2, and thereby predict micro-ball end milling force.

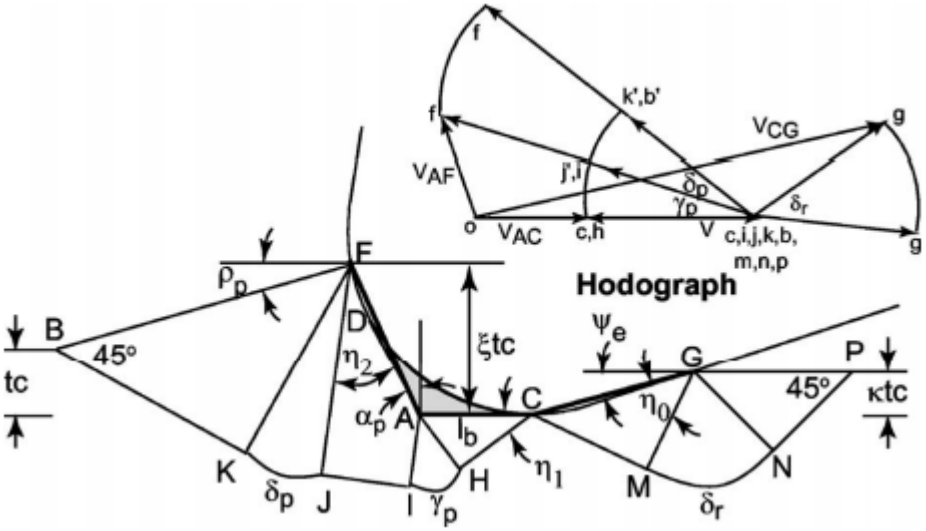

Figure 2.11 Slip-line field for ploughing/rubbing without chip formation and its associated hodograph [1]

The above slip-line model can well predict the orthogonal cutting forces in micro-level

machining, as it analytically takes into account the effects of chip thickness. Compared to the empirical mechanistic model which needs intense experimental fitting, the slip-line model can be easily calibrated by obtaining the flow stress k, the shear angle ϕ, the prow angle ρ, and angles η_0, η_1 and η_2 which depend on friction factor on different slip-line faces. Due to its accuracy in low chip thickness condition force prediction, this model is adopted as the basic slip-line model in the work of this thesis.

However, the use of the slip-line model in tool force prediction requires accurate chip thickness model, the chip thickness algorithms presented in 2.2.2 and by [16, 26] considered the tool to be perfectly rigid, which is often not the case in micro-milling operations, where runout and tool dynamics is significantly affecting the chip thickness formation. In order to study the behaviour of tool runout, next section presents previous works on tool runout modelling.

2.3.4 Runout study in micro-end milling

When tool runout presents in the end milling process, cutting edges on each flute of the end mill will rotate at a different radius due to the center offset of the tool movement, resulting in varying chip thickness in the cutting process. While the runout effect on cutting force may not be obvious during macro-scale machining, Bao et al and Li et. al [35, 36] suggests that it dramatically affects the force result in micro-scale end milling. This is due to the relatively large tool offset that is in the similar scale of the chip thickness in micro-end milling. Unbalanced tool force generation was also found to be significantly affecting tool life [37]. An effective model of the runout condition is essential to the accurate force prediction.

It is commonly believed that two types of runout are presented in machining: the parallel

offset runout shown in Fig. 2.12-(a) and the spindle tilt runout showed in Fig. 2.12(b). Early attempt of runout modelling in end mill machining by Kline et al. [13] has incorporated the parallel offset runout in the in-plane tool movement with a constant feed rate and direction. Sutherland and DeVor [38] have extended the runout model to include spindle tilt effect. In their model, chip thickness t_c can be calculated with known effective tool flute radius on j^{th} flute and i^{th} disk (i,j) , and given as

$$t_c(i,j,k) = R(i,j) - R(i,j-m) + mf_t \sin\theta(i,j,k), \qquad (2.39)$$

where the additional terms $R(i,j)$, $R(i,j-m)$ and m are characterizing the additional effect on chip thickness by runout movement. However, this model requires predetermination of runout parameters including the actual parallel offset, spindle tilt and locating angle that determines the direction of spindle tilt. In micro-end milling environment, the measurement of these small features become highly difficult. Jun et al. [1] presented a feasible method for runout parameter estimation using a capacitive distance sensor.

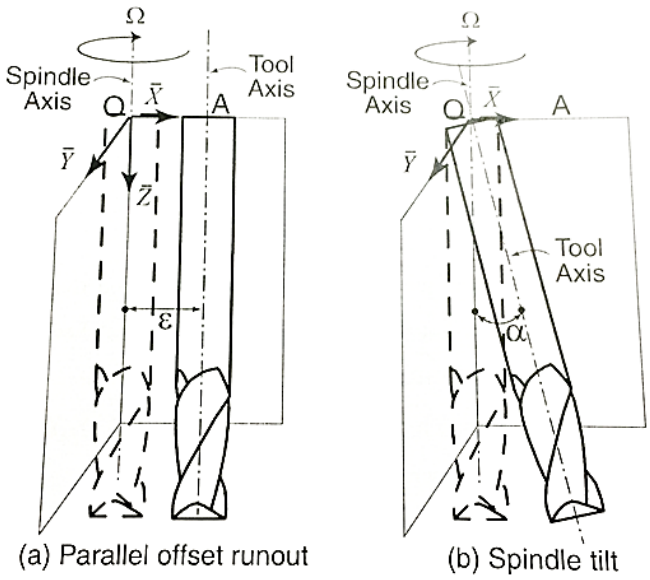

Figure 2.12 Types of runout: (a) parallel offset runout (b) spindle tilt [1]

As shown in Fig. 2.13, the tool is discretized as discs along the tool center axis. The net tool shank runout in location i is denoted as r_i. Showen in Fig. 2.14, the parallel shank runout ε and its locating angle λ_s, the shank tilting angle β and the the tilt direction angle α on tool shank location z_i has the following relationship:

$$r_i^2 = r_0 + r_1 z_i + r_2 z_i^2, \tag{2.40}$$

where

$$\varepsilon = \sqrt{r_0} \tag{2.41}$$

$$\tan(\beta) = \sqrt{r_2} \tag{2.42}$$

$$\cos\left(\frac{\pi}{2} - \alpha\right) = \frac{r_1}{2\sqrt{r_0 r_2}} \tag{2.43}$$

therefore by measureing the net shank runout r_i on multiple locations on the tool shank using capacitive displacemnet sensor as illustrated on Fig. 2.15, one can obtain the runout parameters on the current set up.

On top of tool shank runout, Jun et al. [1] also presented the cutter section runout model, as the thin and long cutter section tend to contribute a second order mode of runout. In this thesis, the expeirments has been done on stub length ball end mills, thus the effects of secon mode runout is negelegible.

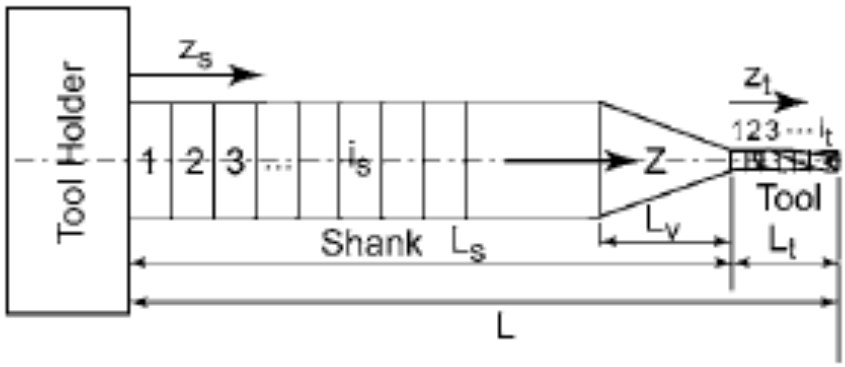

Figure 2.13 discretization of the micro-end mill [1]

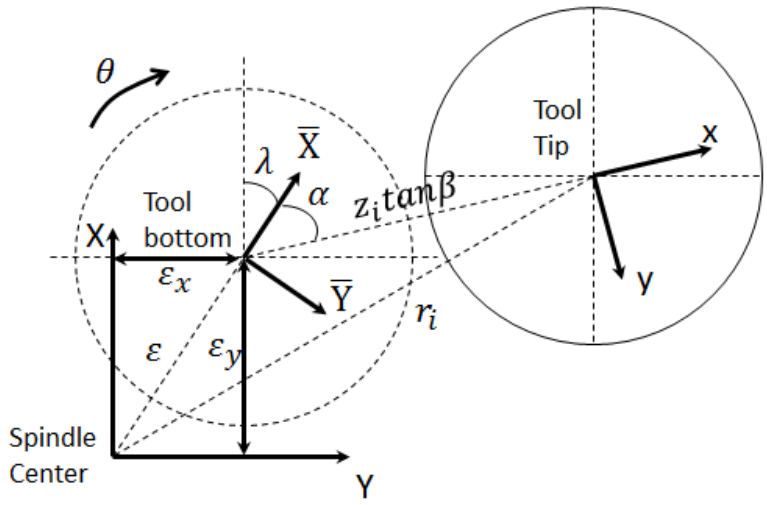

Figure 2.14 Tool runout parameters showed in the top view of the norminal tool axis

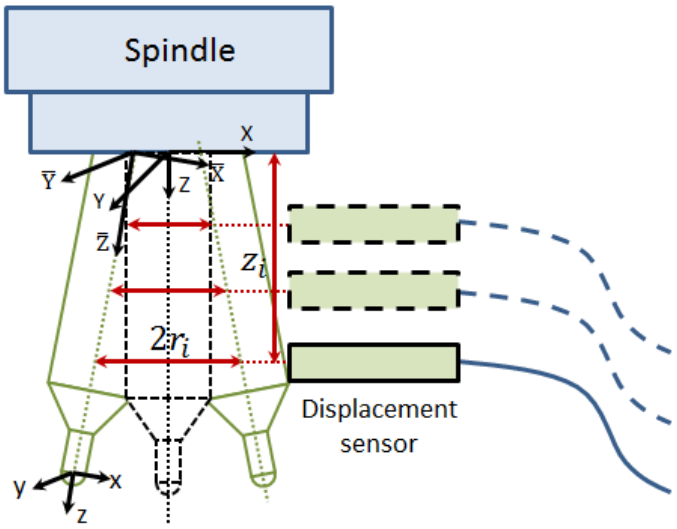

Figure 2.15 Runout measurement setup.

2.3.5 Cutting edge indentation force in ball end milling

Due to relatively large cutting edge radius to chipload ratio in micro-ball end milling, the indentation of the cutting edge into the workpiece is also creating considerable force that is not incorporated in conventional shearing-force dominated force models, research has been done by Tuysuz et al. [2] to evaluate the elasto-plastic deformation of the workpiece material indented by a rigid tool cutting edge.

Tuysuz et al. [2] proposed that as the tangential cutting speed approaches zero around the ball end mill tool tip area, the axial cutting force generated in this area is majorly contributed by the indentation of the cutting edge into the workpiece material. The indentation effect becomes most dominant when the tool is directly plunging downward into the workpiece with the tool tip region engaged. Therefore, the indentation condition is modelled analytically by [2] in order to create an indentation force prediction model. As shown in Fig. 2.16-(a), the indentation force is modelled using the elastic contact model for an inclined punch with the assumptions of plane stain deformation of the workpiece, friction less contact between the rigid cutting edge and the elasto-plastic workpiece, and straight and long enough flank on the tool.

As Fig. 2.16 (b) shows, for a cutting edge with positive rake angle, the indentation pressure along the tool flank is separated as the elastic contact pressure and plastic contact pressure along the horizontal axis X. As the origin of the coordinate system is placed in the location where the tool-workpiece contact ends, the elastic contract pressure $p_{elastic}$ along the location on X axis is expressed by [2]as:

$$p_{plastic}(x) = \frac{Eb}{4\pi R_{edge}(1-\upsilon^2)(1+y^2)}\left[(1-y^2)\left(\frac{\pi}{4}-\tan^{-1}(y_1)\right)-\frac{(y-y_1)(1-yy_1)}{(1+y_1^2)}\ln\left(\left|\frac{y_1-y}{yy_1-1}\right|\right)\right],$$

$$y=\tan\left(\frac{1}{2}\sin^{-1}\left(\frac{2x-b}{b}\right)\right), y_1=\tan\left(\frac{1}{2}\sin^{-1}\left(\frac{2c-b}{b}\right)\right), y_2=\tan\left(\frac{1}{2}\sin_1\left(\frac{-2c-b}{b}\right)\right), \quad (2.44)$$

where E is the Young's modulus and υ is the Poisson's ratio of the workpiece material. R_{edge} is the edge radius. b is the total length of the projected indentation area, and c is the length of the X_E axis projection of the flat part of the tool shown in Fig. 2.16-(b). Shown on the same figure, the indentation limit angle ξ determined the rounded part contribution to the overall cutting edge contact length, and is calculated as

$$\xi = \begin{cases} \sin^{-1}\left(1 - \frac{h_{ind}}{R_{edge}}\right), & R_{edge} \geq h_{ind} \\ 0, & otherwise \end{cases}, \tag{2.45}$$

where h_{ind} is the depth of indentation, which is also the chip thickness if applied to a ball end mill model.

The overall contact length b is expresses as

$$\begin{aligned} b &= d + c, \\ d &= R_{edge}(\sin\alpha_n + \cos\xi), \\ c &= \frac{h_{ind} - R_{edge}(1 - \cos\alpha_n)}{\tan\alpha_n}. \end{aligned} \tag{2.46}$$

On Fig. 2.16-(a), the boundary between the elastic pressure and plastic pressure zone are determined by where the elastic pressure reaches the plastic limit defined by [2] as

$$p_{plastic} = C\sigma_y, \tag{2.47}$$

where $\sigma_y$is the compression yield strength of the work material and C is a material constant. Hence for a positive rake angle cutting edge, the pressure distribution in the cutting edge element along X_E is expressed as

$$K_{ind} = \sum_{x_0}^{x_1} p_{elastic}(x)dx + \sum_{x_1}^{x_2} p_{plastic}(x)dx + \sum_{x_2}^{b} p_{elastic}(x)dx, \tag{2.48}$$

where $x_0 = R_{edge}(1 - \cos\xi)$. Hence the total indentation force in this tool section for chip thickness h_{ind} can be calculated as the integral of Eqn. (2.48). In ball end milling force model, the indentation force is then added to the axial force component along the cutting edge.

Although Tuysuz et al. [2] has also presented the indentation pressure calculation for cutting tool with negative rake angles it has been excluded from this section since only tool with positive rake angle is in interest of this research.

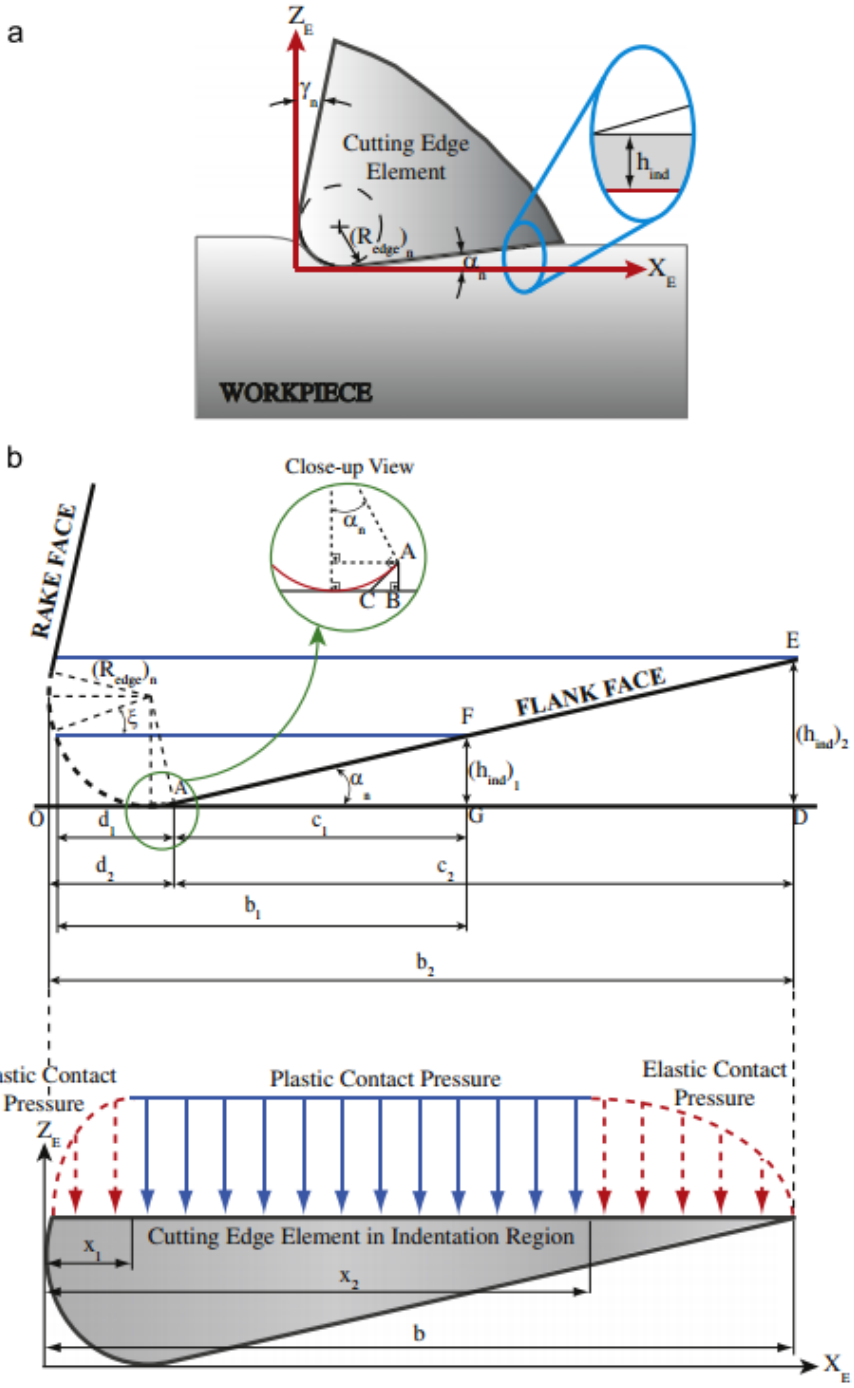

Figure 2.16 (a) indentaion of cutting edge element into the workpiece and (b) indentation geometry and general total contact pressure distribution for positive rake angle [2]

For determination of the distribution of indentation force along the ball end mill cutting edge, Tuysuz et al. [2] also proposed a distribution scheme as shown in Fig. 2.17(a) in order to determine the indentation dominiant region and shearing dominant region on the tool. This

scheme assumed that the indentaion region is alwalys centered in the tool tip area and is totally depend on the indentation depth and the tool geometry. However, in reality the indentation is not limited to the tool tip area, but depend on the ratio of the radial tool movement and the tangential tool movement.

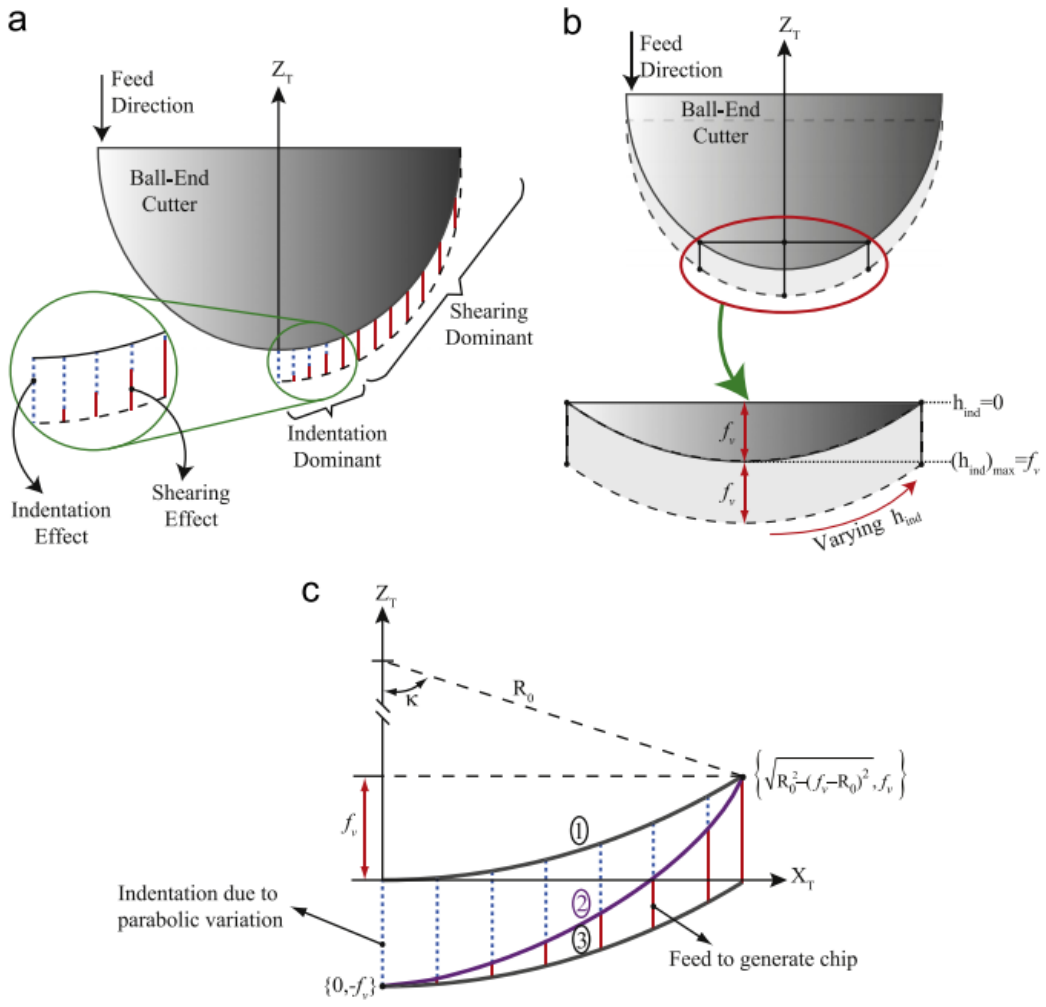

Figure 2.17 (a) Shearing and indentation regions on the cutter; (b) max. and min. indentation depths and their locations along the flute and (c) parabilic variaton of the indentation along the cutter flute [2].

2.3.6 Model-based cutting process scheduling scheme

In order to achieve optimal machining result and efficiency, conventional cutting process scheduling is often performed independently of cutting force models. Multiple researchers have focused on creating algorithms that generate smooth tool trajectories that control

velocity, acceleration and jerk of the CNC machine axes [39-42]. By implementing these strategies, machining times can be significantly reduced while maintaining continuity of the tool path. Also, less variability of cutting force will be introduced because motor/amplifier saturation will be avoided. Unfortunately, these approaches are more suitable for macro-scale machining applications due to no tool strength limitation is considered during the velocity profile optimization process.

Tansel et al. [43] has suggested that tool life is directly affected by the cutting force. However, majority of the process planning in industry is based on extensive trials and experience. This practice has become increasingly difficult in five-axis free-form surface machining, as tool trajectory and orientation is constantly changing along the machining path. Therefore machining process scheduling based on process modeling becomes important.

For five-axis micro-ball end milling, Zhu et al. [9] proposed a feed rate scheduling scheme based on a chip thickness prediction model to reduce the abrupt increase in chipload due to change of cutting conditions for machining free form surfaces. The feed rate scheduling is done by simple feed rate reduction if abrupt chip thickness increase is predicted on the tool path. However, this feed rate scheduling scheme does not use other cutting conditions including tool inclination angles to reduce cutting force, thus total machining time will be increased. In addition, the use of chip thickness model for process scheduling neglected the effect of indentation force, which can be significantly large without creating a large chip load. Therefore a more comprehensive process scheduling scheme for five-axis ball end milling using accurate force prediction model is desired.

2.4 Summary

This chapter has reviewed important research works that contribute to development of the

five-axis micro-ball end milling force modelling. The fundamentals of ball end mill force modelling including mechanistic modelling chip thickness calculation and ball end mill mechanism has been discussed. Research approaches that enabled five-axis machining environment modelling including chip thickness and tool/workpiece engagement models are also presented. Important modelling elements for micro-machining including slip-line model, runout model and indentation model are separately discussed. It is shown that detailed ball end mill force modelling for the complex micro-scale modelling with various tool positions in five-axis environment is highly possible.

Despite the tremendous amount of research achievements in both analytical and numerical force modelling, process modelling and process fault study, the knowledge gap that leads to the topic of this research is obvious. First, due to highly important tool tip area in certain five-axis machining positions, ball end mill flute elements need to be evenly distributed along the whole cutting edge, an effective five-axis ball end mill model requires a different way of geometric flute discretization rather than the traditional disk element method.

Second, the lack of historical chip thickness storage scheme in previous models prevents the accurate force modelling if the workpiece surface is being revisited by the cutter flute. A workpiece updating algorithm that stores historical chip thickness is in need.

Third, the individual use of the existing slip-line model and the indentation model will result in inconclusive force prediction results for certain cutting conditions: slip-line model does not account for extra Z-directional force during tool plunging movements, while the use of current indentation model on ball end mill does not have a versatile weighing function to properly distribute indentation and cutting force for various tool cutting conditions and trajectories. Therefore, a comprehensive composite force model that combines the advantage

of both the slip-line model and the indentation model is essential to five-axis micro-ball end milling.

Lastly, the existing model-based machining process scheduling scheme is limited to feed rate scheduling using chipload prediction model. This approach is found to be inconclusive because it only used feed rate reduction for process scheduling therefore total machining time will be significantly affected. The chipload prediction model itself also does not consider indentation force, which could be a significant cutting force contributor without creasing large chip thickness. Hence, it is desired to develop a process scheduling scheme based on a comprehensive force modeling.

The knowledge gaps discussed above are what motivate the work in this thesis. In the following chapters, a new composite model is introduced that properly addresses the unresolved needs in micro-ball end milling.

Chapter 3

Five-axis Micro Ball End Milling Force Model Development

In this chapter, the development process of the composite force model for five-axis micro-ball end milling is presented, starting by introducing the micro-ball end milling kinematics, which explains the ball end mill geometry discretization, coordinate transformations and chip thickness algorithms. This is followed by the introduction of the workpiece updating algorithm, which serves as both purpose of tool-workpiece registration and historical chip thickness storage. Next, the slip-line force model is introduced by detail explanation of the cutting and shearing force calculation in both the shearing-dominated and the ploughing-dominated regime. On the other hand, the indentation force model is introduced to calculate the extra radial directional force generated by indentation of the cutting edge into the workpiece. At last, the total cutting force is calculated by the combination of the slip-line model and the indentation force model through a dedicated weighting function.

3.1 Micro-ball end milling kinematics

In this section, the ball end mill is discretized and the cutting edge geometry is defined. Position and velocity kinematics are subsequently specified to provide a basis for chip thickness calculations.

3.1.1 Ball end mill geometry

The first step in model development is to decompose the cutting edge into a set of i circular sectors by discretizing the polar angle into differential segments $d\gamma$, as shown in Fig. 1. For the present work, it is assumed that cutting is limited to the ball-portion of the end mill. Each cutting edge point $\overrightarrow{P_t}$ is parameterized by the i^{th} circular sector element and the j^{th} flute. The location of $\overrightarrow{P_t}$ is expressed in spherical coordinates, as shown in Fig. 2. The polar angle is defined explicitly as

$$\gamma(i) = id\gamma,$$
$$d\gamma = \frac{\pi}{2N_s}, \tag{3.1}$$

where N_s is the total number of discretized circular sectors.

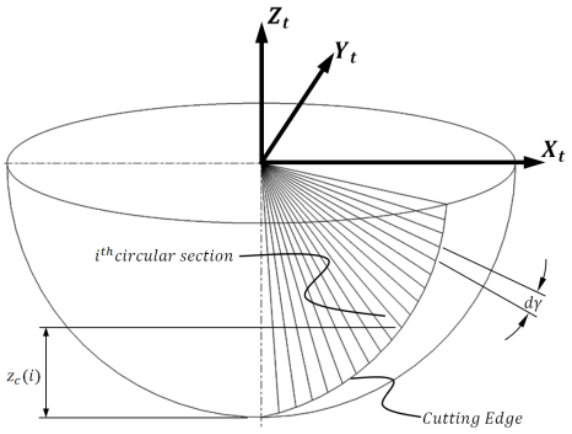

Figure 3.1. Polar angle discretization of ball tip.

Following this representation, each cutting edge point can be represented within a Cartesian tool coordinate frame $[\mathrm{X_t}, \mathrm{Y_t}, \mathrm{Z_t}]$ as

$$\overrightarrow{P_t}(i,j) = \begin{bmatrix} x_t(i,j) \\ y_t(i,j) \\ z_t(i,j) \end{bmatrix} = \begin{bmatrix} R_0 \sin(\gamma(i)) \cos(\varphi(i,j)) \\ R_0 \cos(\gamma(i)) \sin(\varphi(i,j)) \\ -R_0 \cos(\gamma(i)) \end{bmatrix}, \quad (3.2)$$

where R_0 is the nominal radius of the ball end mill and φ is the tool immersion angle.

A detailed derivation of these geometrical parameters is provided by Zhu et al. [9]. A summary of these parameters are given below

$$\begin{aligned} \lambda(i) &= \operatorname{atan}(\sin\gamma(i) \tan\lambda_0) \\ \delta(i) &= \frac{1-\cos\gamma(i)}{\sin\gamma(i)} \tan\lambda(i) \\ \varphi(i,j) &= \delta(i) + \frac{(j-1)2\pi}{N_f}, \end{aligned} \quad (3.3)$$

where λ is the local helix angle, δ is the lag angle, and N_f is the total number of flutes. Without a loss of generality, N_f is assumed to be 2 flutes in this work.

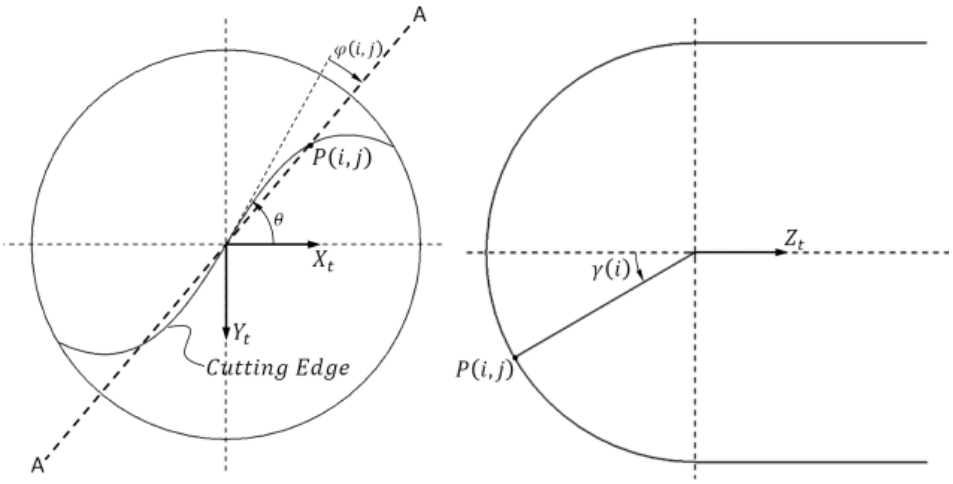

Figure 3.2. Ball end mill cutting edge location.

3.1.2 Coordinate transformations

Homogeneous transformations are used to map the cutting edge points $\vec{P_t}$ from the tool coordinate frame to the workpiece coordinate frame $[X_w, Y_w, Z_w]$. In order to capture the effects of spindle runout, an intermediate coordinate system $[X_i, Y_i, Z_i]$ is introduced to describe the theoretical pose of the ball end mill. Homogeneous transformations are applied to emulate parallel axis offset as well as angular misalignment between the tool axis and spindle axis. Cutting edge locations referenced in the intermediate tool frame can then be mapped to the workpiece frame with the corresponding commanded tool trajectories. These coordinate frames are graphically represented in Fig. 3.3.

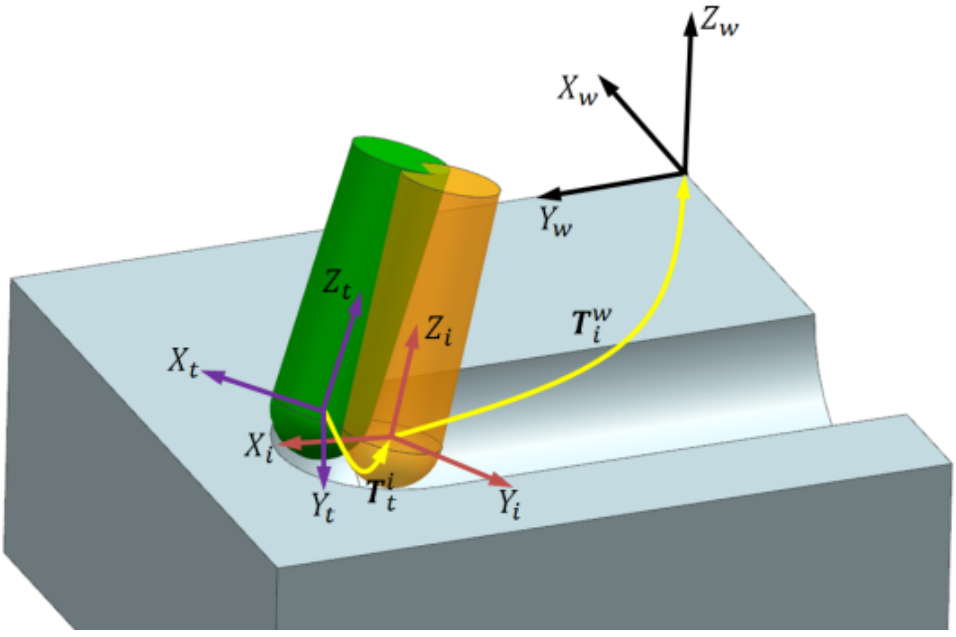

Figure 3.3. Coordinate frames transformations.

3.1.2.1 Intermediate theoretical tool frame

The first homogeneous transformation maps the cutting edge points defined in Sec. 2.1 to

an intermediate tool frame. This transformation accounts for parallel axis runout as well as misalignment between the tool axis and the spindle axis. The homogeneous transformation is given by

$$\mathbf{T}_t^i = \mathrm{Trans}(0,0,l_t)\mathrm{Rot}_z(\theta)\mathrm{Rot}_z(\alpha) * \mathrm{Rot}_x(\beta)\mathrm{Trans}(\varepsilon_x, \varepsilon_y, 0)\mathrm{Trans}(0,0,-l_t), \quad (3.4)$$

where l_t is the length of the tool, α and β define angular axis misalignment due to runout, ε_x and ε_y define the parallel axis runout, and θ is the spindle rotation angle. The runout parameters from this homogeneous transformation are shown graphically in Fig. 3.4.

It should be noted that these runout parameters represent the overall runout experienced at the end mill flutes. This will include the effective errors induced by both the end mill collet system and the cylindricity tolerances of the end mill itself.

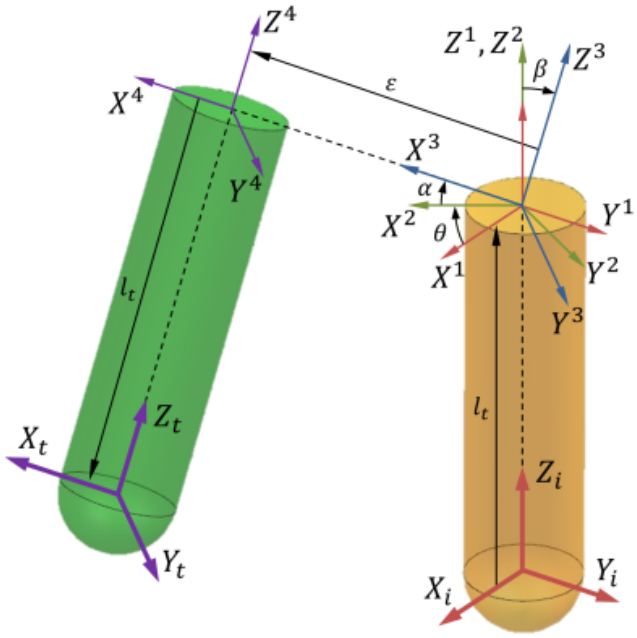

Figure 3.4. Intermediate tool frame runout parameters.

3.1.2.2 Workpiece coordinate frame

The ball end mill pose is described by a position vector specifying the location of the ball end mill center along with the two inclination angles of the tool: lead angle and tilt angle. Both of these angles represent the angle between the tool shank axis and the line normal to the machining surface. As shown in Fig. 3.5, for a right-handed tool, a positive tilt angle means the tool is tilted to the right and doing down milling when facing feed direction, and vice versa. Similarly, a positive lead angle means the tool is leaning forward to the feed direction, and vice versa.

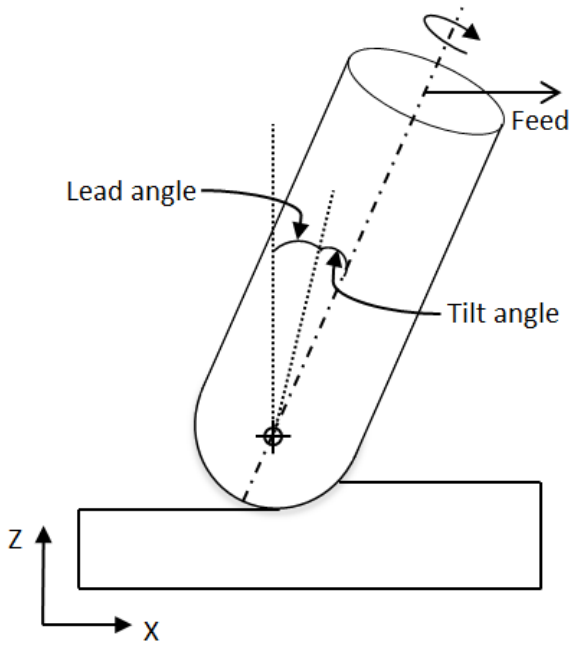

Figure 3.5. Illustration of tool inclination angles

As shown in Fig. 3.6, the homogeneous transformation from the intermediate theoretical tool frame to the workpiece frame is defined by

$$\boldsymbol{T}_i^w = Trans(\overrightarrow{Q_w})Rot_z(\Omega_z)Rot_x(\Omega_x)$$

$$\overrightarrow{Q_w} = [x_{tool}, y_{tool}, z_{tool}]^T \ , \tag{3.5}$$

where $\overrightarrow{Q_w}$ is the tool center position vector and x_{tool}, y_{tool}, and z_{tool} are the components of the position vector in the workpiece coordinate frame. Ω_X and Ω_Z are tool position angles about the X- and Z- axes in the workpiece coordinate frame. The relationship between Ω_X / Ω_Z and lead/ tilt angles are given as:

$$\Omega_X = \begin{cases} 90° - \sin^{-1}\left(1/\sqrt{1 + \frac{1}{\tan^2(90°-lead)} + \frac{1}{\tan^2(90°-tilt)}}\right) & tilt \geq 0 \\ \sin^{-1}\left(1/\sqrt{1 + \frac{1}{\tan^2(90°-lead)} + \frac{1}{\tan^2(90°-tilt)}}\right) - 90° & tilt < 0 \end{cases} \tag{3.6}$$

$$\Omega_Z = \begin{cases} \sin^{-1}\left(\frac{1}{\tan(90°-lead)}/\sqrt{\frac{1}{\tan^2(90°-lead)} + \frac{1}{\tan^2(90°-tilt)}}\right) & tilt \geq 0 \\ -\sin^{-1}\left(\frac{1}{\tan(90°-lead)}/\sqrt{\frac{1}{\tan^2(90°-lead)} + \frac{1}{\tan^2(90°-tilt)}}\right) & tilt < 0 \end{cases} \tag{3.7}$$

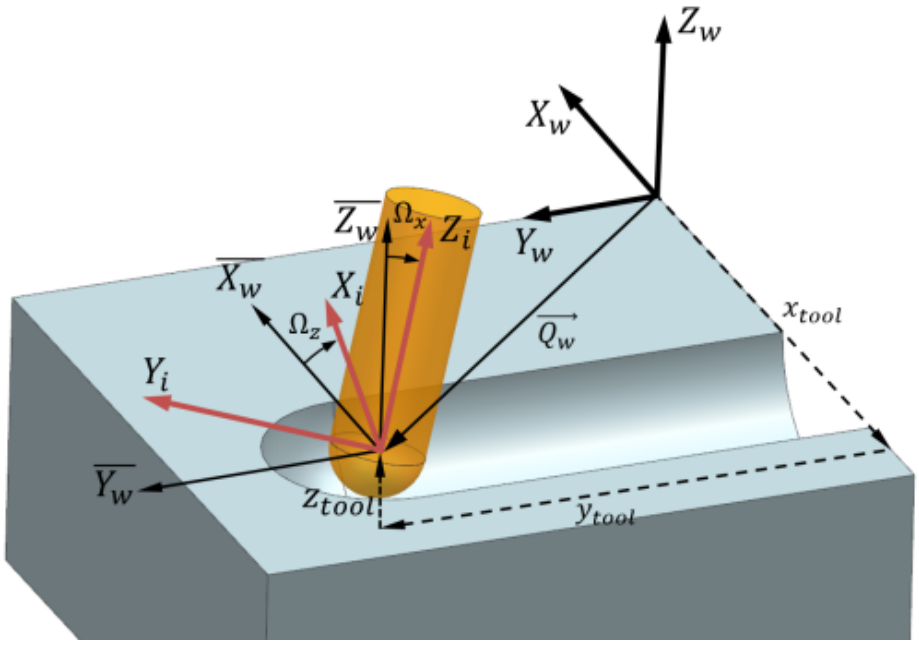

Figure 3.6. Ball end mill location and orientation parameters.

3.1.3 Tool velocity kinematics

Using the two homogeneous transformations defined above, cutting edge points in the tool frame are mapped to the workpiece frame as

$$\overrightarrow{P_w} = \mathbf{T}_i^w \mathbf{T}_t^i \overrightarrow{P_t} = \mathbf{T}_t^w \overrightarrow{P_t} = \begin{bmatrix} \mathbf{A} & \vec{d} \\ \vec{0}^T & 1 \end{bmatrix} \overrightarrow{P_t}, \tag{3.8}$$

where $\mathbf{T}_t^w$ is a 4x4 matrix that describes the total transformation. $\mathbf{A}$ is a rotation matrix and $\vec{d}$ is the translational vector, which are both functions of time.

The velocity of point $\overrightarrow{P_w}$ in the workpiece frame is calculated as

$$\overrightarrow{v_w} = \dot{\mathbf{T}}_t^w \overrightarrow{P_t} = \dot{\mathbf{T}}_t^w \left(\mathbf{T}_t^{w-1} \overrightarrow{P_w} \right) = \begin{bmatrix} \dot{\mathbf{A}}\mathbf{A}^T & -\dot{\mathbf{A}}\mathbf{A}^T \vec{d} + \dot{\vec{d}} \\ \vec{0}^T & 0 \end{bmatrix} \begin{bmatrix} \overrightarrow{P_w} \\ 1 \end{bmatrix}, \tag{3.9}$$

3.2 Chip thickness algorithm

In traditional three-axis cutting force models, the cutter feed motion is typically assumed to be planar [1, 5, 16, 18]. However, the complex tool movements associated with five-axis machining requires a versatile chip thickness algorithm to be defined. The velocity of a cutting edge point is projected onto its associated outward radial vector, which is defined as the direction from the tool center to the cutting edge point. The feed vector for each discretized cutting edge point is then defined as the distance traveled in the radial direction in $1/N_f$ rotations. This is given explicitly as

$$\vec{f} = \left(\left(\frac{60}{N_f N} \right) \overrightarrow{v_w} \cdot \overrightarrow{n_r} \right) \overrightarrow{n_r},$$

$$\overrightarrow{n_r} = \frac{\overrightarrow{Q_w} - \overrightarrow{P_w}}{\left\| \overrightarrow{Q_w} - \overrightarrow{P_w} \right\|}, \tag{3.10}$$

where N is the spindle speed (RPM) and $\overrightarrow{n_r}$ is the outward radial vector.

This feed vector is equivalent to the perpendicular distance between two consecutive flutes during a spindle rotation since the velocity projection eliminates all tangential components. Correction factors for runout and elastic recovery are subsequently added to the feed vector to calculate the total chip thickness.

Tool runout, which was introduced in the transformation to the intermediate tool frame, will cause a variation in chip thickness as the tool rotates around the spindle axis. In this context, runout is defined as the distance between a given cutting edge point in the tool frame and the corresponding point in the transformed intermediate frame. This runout factor is again projected in the radial direction $\overrightarrow{n_r}$ and is defined explicitly as

$$\overrightarrow{h_{ro}} = \left(\left(\mathbf{T}_t^i \overrightarrow{P_t} - \mathrm{Rot}_z(\theta) \mathrm{Rot}_z(\alpha) \overrightarrow{P_t} \right) \cdot \overrightarrow{n_r} \right) \overrightarrow{n_r}, \tag{3.11}$$

During micro-machining, the chip loads tend to be small to compensate for the low rigidity of micro-end mills. At these small chip loads, a minimum chip thickness (MCT) is observed. Chip loads below this threshold are observed to shift from a shearing-dominated regime to a ploughing-dominated regime[1, 4, 16]. Ploughing is typically associated with elasto-plastic deformation followed by elastic recovery. In this case, elastic recovery at a cutting edge point is represented as a vector and is given as

$$\overrightarrow{h_{er}} = \begin{cases} \kappa\overrightarrow{t_c} & \text{if } \left\|\overrightarrow{t_c}\right\| < t_{c,min} \\ 0 & \text{else} \end{cases},$$

$$\kappa = \begin{cases} 1.0 & \left\|\overrightarrow{t_c}\right\| < t_{ce} \\ p_e & t_{ce} \le \left\|\overrightarrow{t_c}\right\| < t_{c,min} \\ 0 & \left\|\overrightarrow{t_c}\right\| \ge t_{c,min} \text{ or } \left\|\overrightarrow{t_c}\right\| = 0 \end{cases}, \tag{3.12}$$

where κ is the elastic recovery rate factor, p_e is a factor representing the recovery rate for mixed elasto-plastic deformation [1], $t_{c,min}$ is the minimum chip thickness, t_{ce} is the chip thickness corresponding to the elastic limit of the material, and $\overrightarrow{t_c}$ is the total chip thickness at the current step. The elastic recovery $\overrightarrow{h_{er}}$ does not affect the current chip thickness, but rather, must be stored and added as a contribution in future time increments.

The total chip thickness is the sum of the contributions from the feed vector, the runout correction term, and the elastic recovery, which is defined as

$$\overrightarrow{t_c} = \vec{f} + \overrightarrow{h_{ro}} + \left(\overrightarrow{h_{er,prev}} \cdot \overrightarrow{n_r}\right)\overrightarrow{n_r}, \tag{3.13}$$

where $\overrightarrow{h_{er,prev}}$ is the elastic recovery vector from a previous time increment and therefore requires that chip thickness calculations be historically dependent.

Figure 3.7 provides an example plot showing the effects of the runout term on the chip thickness calculation. As can be seen, runout induces an eccentricity causing one flute to have a preferentially higher chip load. It is also observed from Fig. 3.7 that a clear boundary between the shearing and ploughing regimes exists. The ploughed region is observed to possess a slightly larger chip thickness due to the additional elastic recovery contribution.

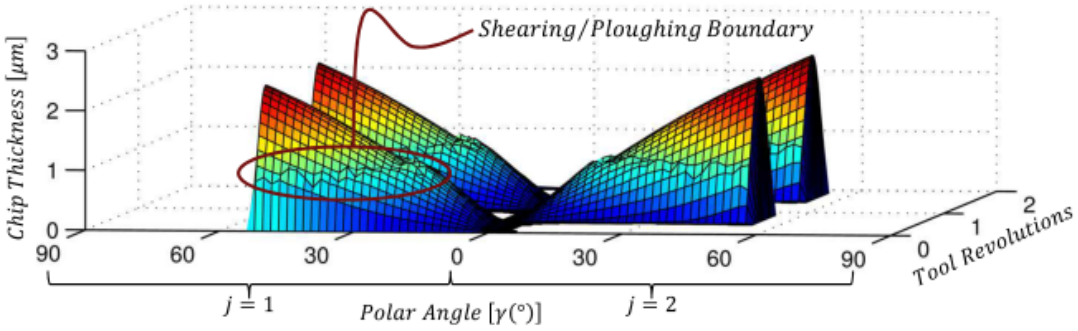

(a)

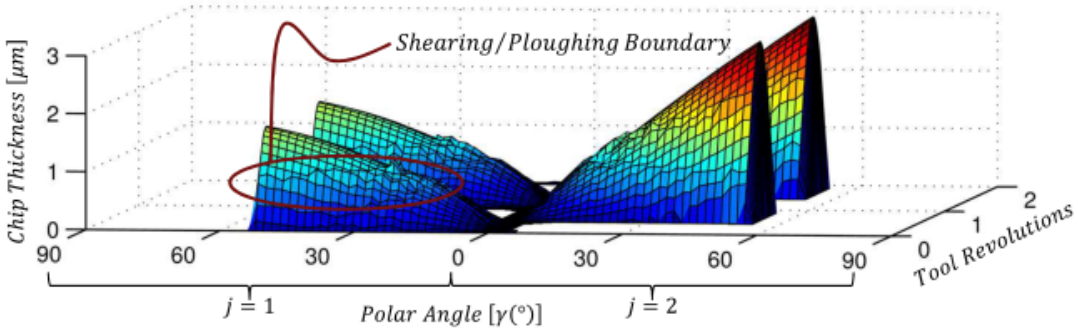

(b)

Figure 3.7. Chip thickness evolution with 3 μm/flute (a) No runout (b) Parallel offset runout ($\varepsilon_y = 0.5\mu m$).

3.3 Tool-workpiece interaction

In this study, the workpiece is limited to surfaces with no undercuts. It is therefore possible to discretize the workpiece and represent the geometry as a 2D uniform point-wise mesh. Since both the tool and the workpiece are discretized in this simulation, the cutting edge point locations will not, in general, match the workpiece grid point locations as the tool proceeds along a set trajectory. The workpiece updating algorithm is therefore necessary to update the workpiece surface to detect cutting edge point engagement as well as store the

localized historical chip thickness vectors for elastic recovery compensation in the chip thickness algorithm.

3.3.1 Workpiece updating algorithm

During the micro-ball end mill simulation, cutting edge points proceed along a given trajectory in discrete time increments. Figure 3.8 shows the workpiece surface mesh from a top view as well as an example of cutting edge points for two consecutive time increments. For each time increment, the grid points located inside the swept area enclosed by the two cutting edges are updated using an interpolation algorithm.

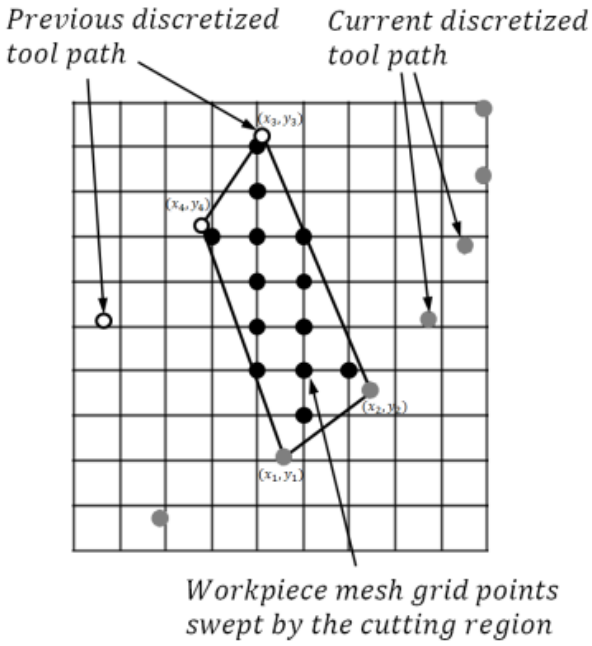

Figure 3.8. Discretized tool path swept area and the workpiece mesh.

The first step of the workpiece interpolation algorithm is to identify the grid points enclosed in the tool swept area between two time increments. Quadrilaterals are formed

between consecutive cutting edge points between two time increments, as shown in Fig. 3.8. These arbitrarily shaped quadrilaterals are then transformed to a unit square through a bilinear mapping function, as shown in Fig. 3.9. This algorithm is similar to shape functions commonly employed by finite element (FE) methods [44]. The Z-height associated with each of the cutting edge points defines the weighting values of the four corners of the unit square. Once the grid points from the workpiece mesh are mapped to the unit square, interpolation is performed using the following linear area weighting algorithm

$$z_{node} = \sum_{i=1}^{4} \frac{A_i}{A} z_i \,, \tag{3.14}$$

where A_i is the area opposite to the vertex of Z- height z_i and A is the unit square area. If the interpolated Z-height is below the current grid point height (i.e. the tool has engaged with the workpiece), the workpiece height is updated.

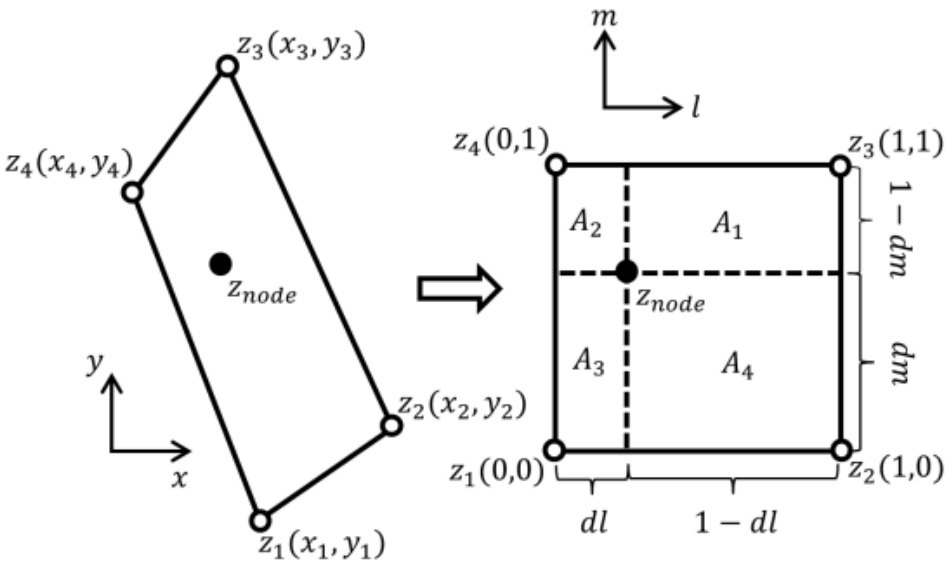

Figure3.9. Bilinear mapping of the tool path quadrilateral to the local unit square.

3.3.2 Historical Localized Chip Thickness

Tracking the elastic recovery on the workpiece is exceedingly difficult for five-axis machining due to the varying tool tilt angles and complex tool-workpiece engagement. A discretized workpiece mesh, however, is particularly suited for this task. As seen in Eq. 11, elastic recovery is a function of a previously stored chip thickness vector. Depending on the trajectory of the tool, this historical chip thickness is not necessarily equal to the chip thickness of the previous flute.

In order to track elastic recovery, the chip thickness generated for each cutting edge point $\overrightarrow{P_w}$ is stored locally on the workpiece mesh using the interpolation algorithm described in Sec. 3.3.1. For each time increment, the elastic recovery will be a function of the workpiece location and will be decoupled from the trajectory of the tool. The workpiece mesh therefore provides a dual purpose: first to represent the z-height of the machined surface, and second to store the localized historical elastic recovery throughout the simulation.

As described in Sec. 3.2, the chip thickness is expressed as a vector. Consequently, the interpolation algorithm is performed for each component of the chip thickness vector. This formulation associates directionality with the elastic recovery term. Depending on the approach direction of the ball end mill, the elastic recovery term will contribute to the total chip thickness only for the component projected onto the direction of the radial vector. The vector-based elastic recovery is shown graphically in Fig. 3.10 with a representation of the workpiece surface along with the components of the chip thickness calculation. It should be noted that elastic recovery is present at the tip of the ball end mill and the side walls perpendicular to the feed direction. These areas are typically prone to small chip thickness

values and therefore induce ploughing.

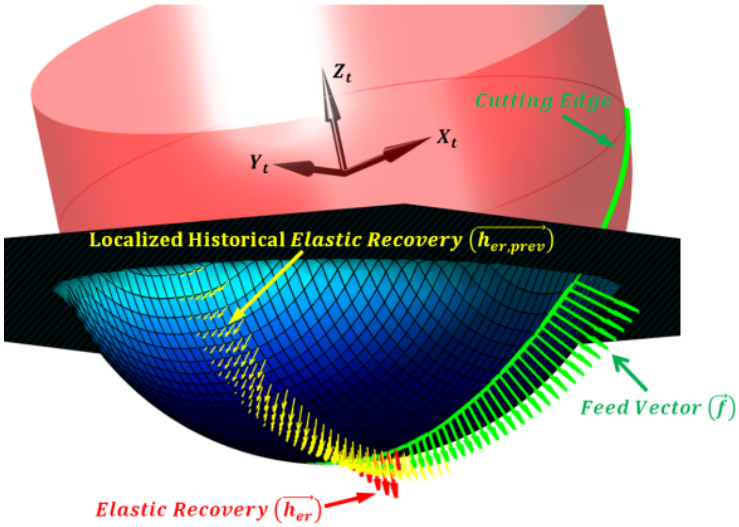

Figure 3.10. Workpiece updating algorithm with local historical elastic recovery vectors.

3.3.3 Tool-workpiece engagement

The workpiece updating algorithm is used to indicate tool-workpiece engagement during five-axis machining. This requires the workpiece Z-height to be known at each cutting edge point $\overrightarrow{P_w}$. Similarly, the localized historical chip thickness is also required at each cutting edge point for elastic recovery calculations. It is therefore necessary to perform interpolation at the cutting edge points while using the workpiece mesh nodes as the original quadrilateral in the bilinear mapping function. The same algorithm described in Sec. 3.3.1 is applicable, except that the mapping is performed on the quadrilateral formed by the four closest mesh points.

3.4 Cutting force model

Orthogonal cutting forces are first calculated based on a slip-line field framework. The

2D forces are subsequently transformed into an equivalent 3D force using the local helix angle. To provide an accurate estimate for plunge-type tool movements, an indentation force is calculated based on the quasi-static contact behaviour near the tip of a ball end mill. These two force contributions are combined to create a composite force model using a weighting function based on the ratio of tangential velocity to the radial velocity of each cutting edge point. In the following section, the general methodology for force calculations is reviewed.

3.4.1 Slip-line field model

Due to the difficult nature of performing calibration experiments required by mechanistic modeling, particularly at the micro-scale, a slip-line field model is the preferred modeling methodology in this work. Each cutting edge point $\overrightarrow{P_w}$ is assumed to be associated with an orthogonal cutting model with differential thickness dS, given as

$$dS = R_0\sqrt{\cos^2\varphi + 2(\cos^2\gamma - 1)(\cos^2\varphi - 1)}d\gamma, \tag{3.15}$$

where dS is the infinitesimal length of the helical cutting edge segment. Based on slip-line theory, differential cutting and thrust forces are calculated for each discretized cutting edge point.

Several slip-line field models have been previously developed for micro-scale orthogonal cutting [1, 26-28]. As opposed to traditional mechanistic force models typically applied in machining literature [5, 8, 9], slip-line models require minimal experimental data fitting and rely on inherent material properties to evaluate force calculations. Following the cutting force model developed by Jun et al. [1], micro-scale cutting can be characterized by two modes. The first mode involves the bifurcation of material flow resulting in chip formation and is

shearing-dominated. The second mode is dominated by ploughing effects and is associated with elasto-plastic deformation with no chip formation.

3.4.1.1 Mode 1: chip formation

The first mode corresponds to the case where the chip thickness is greater than a threshold MCT. In this regime, forces are dominated by a shearing mechanism associated with chip formation. However, the edge radius of the tool is still significant at the micro-scale and therefore it is assumed that a dead metal cap is present in the model, which contributes a ploughing force to the total force calculation. Differential shearing force components in the slip-line field model are defined as

$$\begin{aligned} df_{sc} &= kdS[(\cos\phi + a_\theta \sin\phi)l_s + (\cos(2\eta_2)\sin\alpha_e + a_2\cos\alpha_e)l_b], \\ df_{st} &= kdS[(a_\theta\cos\phi - \sin\phi)l_s + (\cos(2\eta_2)\cos\alpha_e - a_2\sin\alpha_e)l_b], \end{aligned} \tag{3.16}$$

where k is the material shear flow stress, ϕ is the shear angle, and α_e is the effective rake angle. a_θ, l_s, η_2, a_2, l_b are defined explicitly by Jun et al. [1]

In addition, the differential ploughing contribution of the slip-line field model is provided as

$$\begin{aligned} df_{pc} &= kdS[\cos(2\eta_1)\cos\psi + a_1\sin\psi]l_b, \\ df_{pt} &= kdS[a_1\cos\psi - \cos(2\eta_1)\sin\psi]l_b, \end{aligned} \tag{3.17}$$

where η_1, ψ, and a_1 are again defined explicitly by Jun et al [1].

These two differential force contributions are summed to obtain the total differential cutting and thrust forces

$$\begin{aligned} df_t &= df_{st} + df_{pt}, \\ df_c &= df_{sc} + df_{pc} . \end{aligned} \tag{3.18}$$

3.4.1.2 Mode 2: no chip formation

The second mode corresponds to the case where the chip thickness is less than the threshold MCT. Since there is no chip formation, forces generated in this model are completely attributed to elasto-plastic deformation beneath the tool. The force calculation for this mode is summarized below.

$$\begin{aligned} df_c &= kdS[(\cos(2\eta_0)\cos\psi_e - e_0\sin\psi_e)l_e \\ &\quad -e_1 l_b - \big(\cos(2\eta_2)\sin\alpha_p - e_2\cos\alpha_p\big)l_p], \\ df_t &= kdS[(\cos(2\eta_0)\sin\psi_e + e_0\cos\psi_e)l_e \\ &\quad + \cos(2\eta_1)\, l_b - \big(\cos(2\eta_2)\cos\alpha_p + e_2\sin\alpha_p\big)l_p], \end{aligned} \tag{3.19}$$

where η_0, ψ_e, e_0, l_e, e_1, α_p, e_2, l_p and their associated parameters are again derived by Jun et al. [1].

3.4.1.3 Transformation to 3D forces

The slip-line field model generates 2D cutting and thrust forces in an orthogonal cutting framework. These forces are transformed into 3D radial, tangential, and axial forces through the local helix angle as follows [1]

$$df_{r,cut} = df_t,$$

$$df_{t,cut} = df_c \cos\lambda,$$

$$df_{a,cut} = df_c \sin\lambda\ . \qquad (3.20)$$

These force contributions are shown graphically in Fig. 3.11.

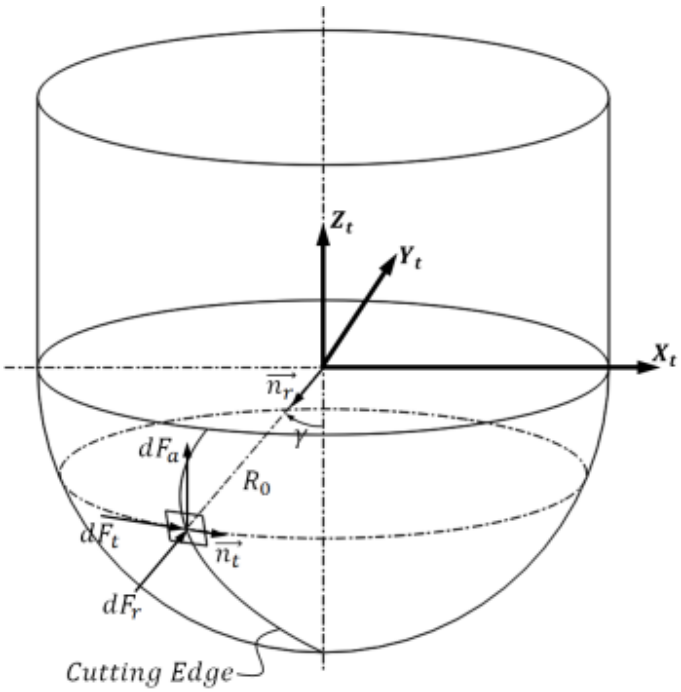

Figure 3.11 Ball end mill force components.

3.4.2 Elasto-plastic indentation force

In a recent study, indentation force during ball end milling was found to have a significant contribution to force generation [2]. In particular, the cutting edge near the tip of a ball end mill experiences relatively low cutting velocities and therefore quasi-static indentation was found to have a critical role in force generation. An analytical solution for tool indentation is

adapted from Tuysuz et al. [2]. For this indentation force component, it is assumed that the tool has a positive nominal rake angle. The differential indentation force is found using the following equations

$$df_{ind} = [\sum_{x_0}^{x_1} p_e(x)dx + \sum_{x_1}^{x_2} p_p(x)dx + \sum_{x_2}^{b} p_e(x)dx]dS$$

$$p_e(x) = \frac{Eb}{4\pi r_e(1-\nu^2)(1+y(x)^2)}\left[(1-y(x)^2)\left(\frac{\pi}{4} - \tan^{-1}(y_1)\right)\right.$$

$$\left. - \frac{(y(x)-y_1)(1-y(x)y_1)}{1+y_1^2} ln\left(\left|\frac{y_1-y(x)}{y(x)y_1-1}\right|\right)\right],$$

$$p_p(x) = C\sigma_y\,, \tag{3.21}$$

where p_e and p_p are the elastic and plastic contact pressure, respectively, E, σ_y, and ν are the elastic modulus, yield strength, and Poisson's ratio of the workpiece, respectively, r_e is the edge radius of the cutting edge, x is the projected distance along the flank face, x_0 is the projected length of initial contact of the indentor, x_1 and x_2 are transition locations between elastic and plastic pressure, b is the total projected length of the indentor, C is a constant that characterizes plastic flow, and $y(x)$ and y_1 are parameters defined explicitly by Tuysuz et al. [2].

3.4.3 Composite cutting force model

A composite cutting force is generated by combining the two force contributions from the shearing/ploughing slip-line model and the quasi-static indentation model. Cutting forces are dominant where the tangential velocity of the cutting edge is relatively high compared to the

radial velocity component. In contrast, the indentation forces dominate when the tangential velocity is relatively small compared to the radial velocity component. The radial and tangential velocity components for each cutting point is computed as follows

$$\begin{aligned}
\overrightarrow{v_r} &= \left(\overrightarrow{v_w} \cdot \overrightarrow{n_r}\right)\overrightarrow{n_r}, \\
\overrightarrow{n_z} &= \mathbf{T}_t^w \overrightarrow{e_3}, \\
\overrightarrow{n_t} &= \frac{\overrightarrow{n_r} \times \overrightarrow{n_z}}{\|\overrightarrow{n_r} \times \overrightarrow{n_z}\|}, \\
\overrightarrow{v_t} &= (\overrightarrow{v_w} \cdot \overrightarrow{n_t})\overrightarrow{n_t},
\end{aligned} \tag{3.22}$$

where $\overrightarrow{e_3}$ is one of the standard basis vectors, $\overrightarrow{n_z}$ and $\overrightarrow{n_t}$ are the unit vectors describing the tool axis direction and tangential velocity direction, respectively, and $\overrightarrow{v_r}$ and $\overrightarrow{v_t}$ are the cutting edge point radial and tangential velocity, respectively.

The magnitude ratio between these two velocities is defined as a threshold ratio χ given by

$$\chi = \frac{\|\overrightarrow{v_t}\|}{\|\overrightarrow{v_r}\|}. \tag{3.23}$$

This threshold ratio provides a measure of the relative significance of shearing/ploughing forces compared to indentation forces. When χ is small, the radial velocity dominates the tangential velocity. This corresponds to a nearly quasi-static indentation process and will typically occur near the tip of the ball end mill. Conversely, when χ is large, the tangential velocity dominates the radial velocity and therefore corresponds to a cutting process. This will typically occur away from the tip of the tool, near the outer periphery of the tool where

rotational velocities are the highest.

The threshold ratio is defined in the interval $[0, \infty)$. It is desired to find a bijective map between $[0, \infty)$ and $[0,1)$ such that a weighting function can be defined for the cutting and indentation forces. A candidate weighting bijective map is given by

$$\mu = 1 - \exp\left(-c_0 \chi^2\right), \tag{3.24}$$

where c_0 is a fitting parameter that dictates sensitivity of the threshold ratio.

This weighting function is used to give relative significance between cutting forces and indentation forces as follows

$$\begin{aligned} df_r &= \mu df_{r,cut} + (1-\mu) df_{ind}, \\ df_t &= \mu df_{t,cut}, \\ df_a &= \mu df_{a,cut}\,. \end{aligned} \tag{3.25}$$

The differential radial force component df_r and the associated slip-line contribution to the differential radial force $df_{r,cut}$ are plotted together in Fig. 3.12. Differential force contributions of each cutting edge point in the radial direction are represented in Fig. 3.12. Tor this example plot, feedrate is set to of $5\ \mu m/flute$ and the polar angle is discretized into 100 elements ($N_s = 100$). It is seen that the overall force trend is generated by the slip-line model, however, the peak values tend to be accentuated with addition of the indentation force component. It should be noted that the significance of the indentation force is highly dependent on the feed direction of the ball end mill and will be most significant during a

plunge-type operation. With complex tool trajectories experienced during five-axis machining, it should be expected that this cutting condition will be significant.

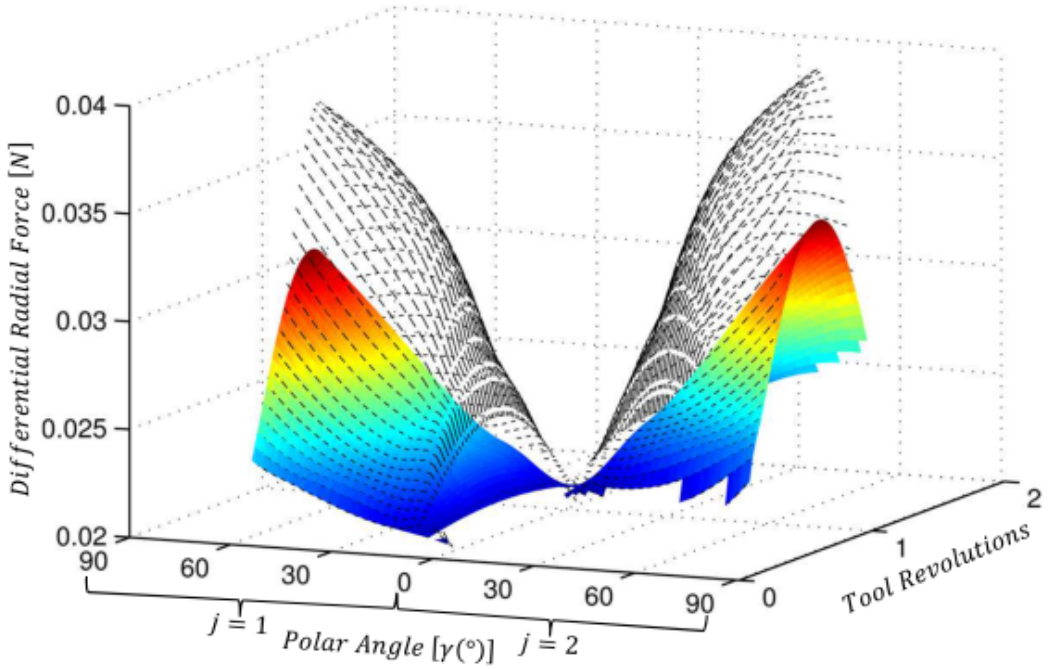

Figure 3.12. Differential radial force contributions: df_r – dotted outline and $df_{r,cut}$ – solid surface.

3.4.4 Force components in workpiece frame

These differential forces are transformed into the global workpiece frame using the following homogeneous transformation

$$[df_x \quad df_y \quad df_z]^T = Rot_z(\Omega_z)Rot_x(\Omega_x) * Rot_z(\theta)Rot_z(\alpha)Rot_x(\beta)Rot_z(\varphi) * Rot_y\left(\frac{\pi}{2} - \gamma\right)[df_r \quad df_t \quad df_a]^T . \tag{3.26}$$

Once the forces are transformed into the global workpiece frame, the differential forces are summed across all of the engaged cutting edge points to find the total force acting on the tool and is given as

$$[F_x \quad F_y \quad F_z]^T = \sum_n^{\text{engaged elements}} [df_x^n \quad df_y^n \quad df_z^n]^T. \tag{3.27}$$

3.5 Summary

In this Chapter, a composite force model for five-axis micro-ball end milling is developed. Within the model, the ball end mill cutting edge is discretized in polar angle, and a set of coordinate transformation is done to incorporate tool position in workpiece frame and runout conditions. A novel chip thickness algorithm that based on cutting edge velocity kinematics is introduced. This unique vector-based framework allows both runout effects and elastic recovery generated during ploughing to be directly incorporated in the chipload calculation. A workpiece updating algorithm is then presented to capture the complex tool-workpiece engagement; however the workpiece model is also able to store historical chip thickness locally for future chip thickness calculation. For cutting force calculation, a slip-line force model is used to calculate the shearing and ploughing force in different chip thickness conditions. In addition to force generated by chip formation, an indentation force model is also used to calculate the radial indentation force between the cutting edge and the workpiece. Finally, a weighting function that depends on the radial/tangential cutting edge speed ratio is designed to balance the contribution between the two force models.

Chapter 4

Model Calibration and Validation

The composite five-axis micro-ball end milling force model consists of a slip-line force model and the cutting edge indentation model. The model also takes into account the runout effect present in five-axis micro ball end millings. Both the slip-line model and the indentation model have been separately calibrated by experiments to obtain set up parameters for material and tool/process geometry. The composite model is validated for a wide range of cutting conditions that represent different scenarios in five-axis ball end mill machining. The runout model introduced in Sec. 3.1.2.1 is also separately validated.

4.1 Five axis micro-ball end mill cutting force measurement experiment set up

To validate the composite five axis ball end mill cutting force model, several requirements regarding to the characteristics of the micro-application must be met. These requirements includes: high repeatability and precision, high resolution, small shank runout from the spindle, controllable spindle and tool speed, etc. To meet these requirements, the UIUC 5-axis micro-machine tool (mMT) was used [3]. Figure 4.1 shows the design and components of the 5-axis mMT, which has three translational stages X,Y,Z, and two rotational stages C and B. Each stage can create movement on one of the axes in a 5-axis system. The mMT is configured by stacking X-Y-C stages which supports the workpiece, and Z-B stages which is holding the electric spindle. The separation of stage stacking can increase the positioning accuracy according to the conclusion from previous research [6]. Design

requirements of the UIUC 5-axis mMT is listed in table 4.1.

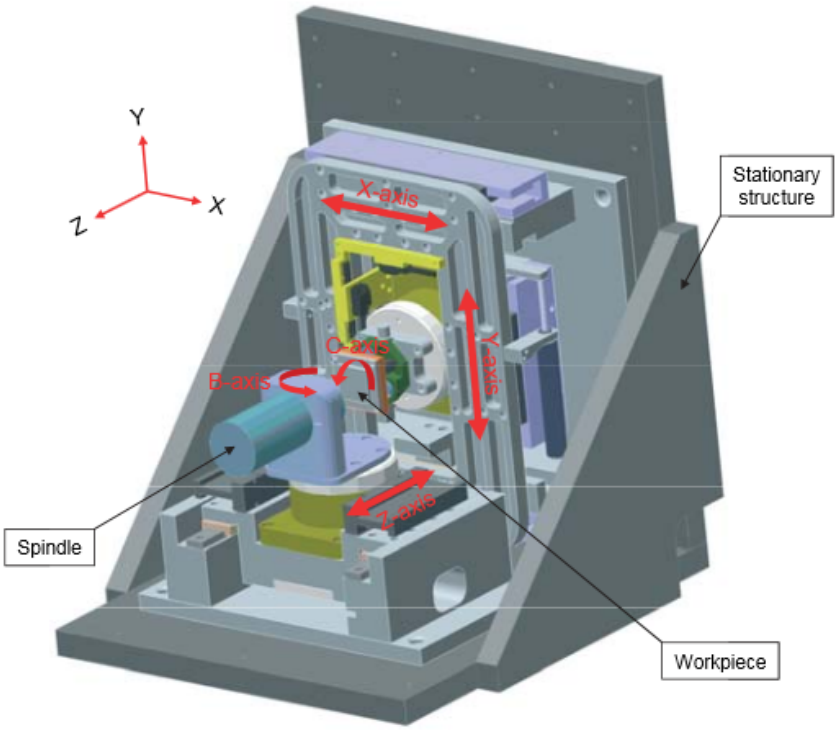

Figure 4.1. UIUC 5-axis mMT [3]

Table 4.1. The UIUC 5-axis mMT design requirements [3]

	General	Linear stages	Rotary stages
Stage travel capability		25 mm	180°-360°
Encoder resolution		1-59 nm	0.05-2.6 arcsec
Spindle speed	1,000-30,000 rpm		
Speed capability		1,600 mm/min	64 rpm
Acceleration capability		5G	377×10^3 °/s^2
Rotary axis offset	<2.5 mm		
Stiffness	10-100 N/μm		
Machine footprint	0.3 m^2		

To record the force exerted on the workpiece during the experiment, a Kistler 9018A three-component force sensor was mounted under the c-stage. X-, Y- and Z- directional force

data will be recorded during the milling operation.

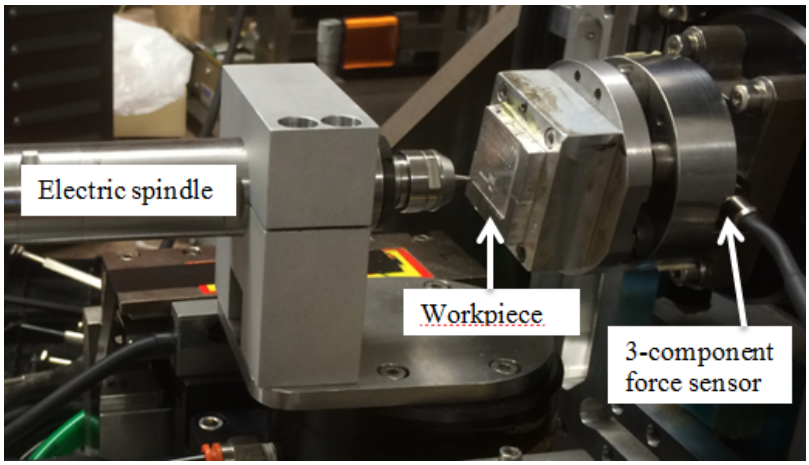

Fig 4.2. The setup for electric spindle and

As the spindle speed can be freely adjusted on a electric spindle, a NSK E2530 electric spindle is retrofitted into the 5-axis mMT system. As shown in fig.4.2, an aluminium spindle mount is machined to hold the spindle in the cutting tool end. As the tool is cutting on the workpiece, force exerted on the three-component force sensor behind the workpiece will be transferred into charge pulses by piezoelectric effect. The charges will be then transmitted into a Kistler charge amplifier which transfer electric charges into time-variant voltage, which will be logged by Labview software from National Instrument.

There are also high frequency signal noises affecting the force measurement. Such high frequency signals can be filtered out by a low pass filter.

4.2 Model calibrations

Experiments are conducted to estimate the slip-line model and indentation force model parameters. For the slip-line model calibration, experiments are done with cutting conditions that are dominated by shearing and ploughing force but do not experience considerable indentation effect. For the indentation force model, experiments are conducted by plunging the tool into the workpiece with little or no shearing.

4.2.1 Slip-line model calibration

For estimation of the parameters needed in the slip-line model, slot cutting experiments with DOC of 50μm and feed rates ranging from 0.5μm/flute to 3μm/flute are performed. The material removal mechanism parameters in the slip-line mode including shear flow stress of the ferrite material k, the minimum chip thickness to tool radius ratio $\frac{tc_{min}}{r_e}$, the tool geometry parameter ξ, the elastic recovery rate p_e, the ferrite Young's modulus E, shear modulus σ and Poisson's ratio ν are adopted from previous estimations done by Jun et al.[1], and are listed Table 4.2.

Table 4.2. Material removal mechanism parameters [1]

Material	$\frac{tc_{min}}{r_e}$	p_e	k(MPa)	E(GPa)	σ(MPa)	ν
Ferrite	0.35	0.09	525	190	350	0.291

For the cutting conditions that result shearing-dominated cutting force, force data from high feed rate experiments, i.e. 1-3 μm/flute are used for calibration. The shear angle ϕ is modeled and is obtained as a function of the effective rake angle α_e according to [16]. Following the fitting procedure developed in [16], the shear angle is obtained as

$$\phi = 9.33 + 0.105\alpha_e. \quad (4.1)$$

The prow angle ρ that controls the ratio between the cutting and thrusting forces and affects the force balance between Z- force and X-/Y- force in the workpiece coordinate frame is estimated as 50°.

Similar to the fitting procedure developed in [26], for the cutting conditions that result in ploughing-dominated cutting force, parameter fitting is done considering cutting/thrust force ratio in low feed rate conditions, i.e. 0.5μm/flute. Slip-line field angles η_0, η_1 and η_2 are defined as a function of friction factors m_0, m_1 and m_2 respectively, and are calculated using the following equation given in [27].

$$\eta_i = \frac{1}{2}\cos^{-1} m_i, \tag{4.2}$$

where m_0, m_1 and m_2 are estimated to be 0.95, 0.85 and 0.99, respectively.

4.2.2 Cutting edge indentation model calibration

As discussed in Sec. 5.2 and 5.3, the indentation model parameter C in Eqn. (3.21) that controls the indentation force magnitude, and c_0 in Eqn. (3.24) that controls the indentation force distribution on the cutting edge need to be estimated from the plunging experiments. Specifically designed experiments are done where the ball end mill directly plunges into the workpiece with feed rates of 0.25, 0.5 and 0.75 μm/flute and a spindle speed of 1,000 rpm starting from a fully immerse condition as shown in Fig. 4.3.

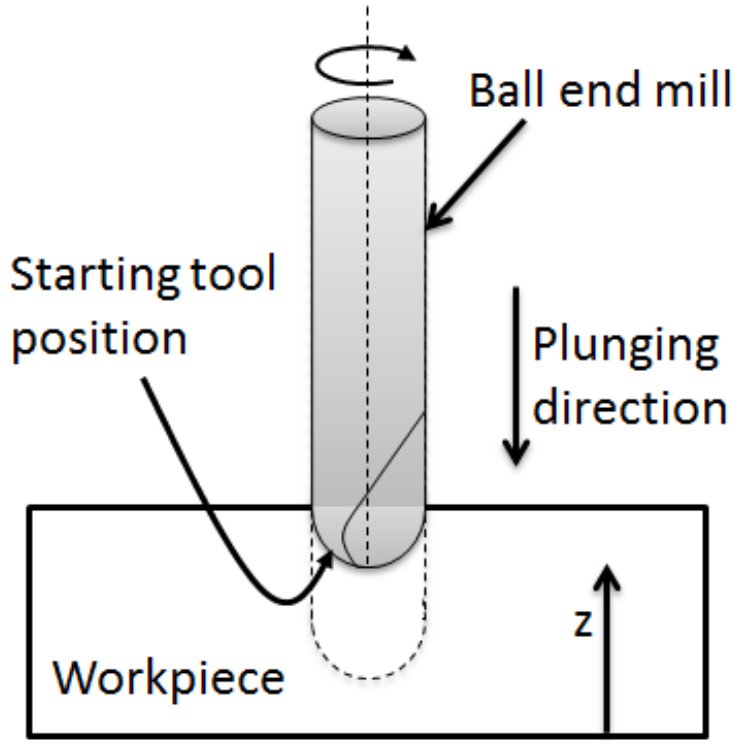

Figure 4.3. Tool plunge test for indentation model fitting

Note that due to large radial/tangential cutting speed ratio χ in the direct plunging cutting condition, the Z- force will be dominated by cutting edge indentation force and is needed to estimate model parameters C and c_o.

With the assumption that the Z-force is entirely caused by cutting edge indentation in high feed rate plunging, the indentation force magnitude parameter C is first obtained as $C = 1.5\times10^{-5}$ using the Z-force from the plunging experiment with the feed rate of 0.75μm/flute. When plunging with lower feed rates, the Z-force is partially contributed by shearing and ploughing, thus the indentation distribution factor $c_0$is estimated as c_0=10.0 using the Z-forces from the plunging experiments with feed rates of 0.5 and 0.25 μm/flute, such that the indentation model prediction error across all feed rate conditions are within 10%.

Note that in reality, the Z-force in all the plunging experiments may also have small

contributions from shearing and ploughing. As an alternative calibration approach, the indentation parameters can also be estimated using the differences between the experimental Z-forces and the slip-line model predictions mainly accounting for shearing and ploughing forces as discussed in Sec. 3.4.1.

4.3 Model validations

4.3.1 Cutting tool runout model validation

In order to validate the effect of runout on the prediction of cutting force using the chip thickness model presented in Sec. 2.2.1, runout parameters including the parallel offset distance ε, parallel angle λ, and shank tilting angles α and β are obtained first using the measurement procedure presented by Jun et al.[1]. For a slot cutting experiment with feed rate= 3μm/flute and DOC=50μm, the resulting runout parameters are measured to be ε=0.367μm, λ_s=25°, α=32.4° and $\beta = 1.375\times10^{-5}$°. These runout parameters are used in the composite force model to predict the cutting force for model validation.

Due to runout effect, the experimental peak-to-valley (P-V) cutting forces for each flute in X- and Y- directions show a "High-low" pattern between the consecutive flutes. Average experimental high and low P-V forces for both X- and Y- directions are calculated over 16 tool revolutions, and are plotted in Fig. 4.4 for comparison. As seen in Fig. 4.4, the composite model predicted X- and Y- direction high and low P-V forces match reasonably well with the experimental results, with an average error of 7.31% for X- direction, and 5.26% for Y-direction.

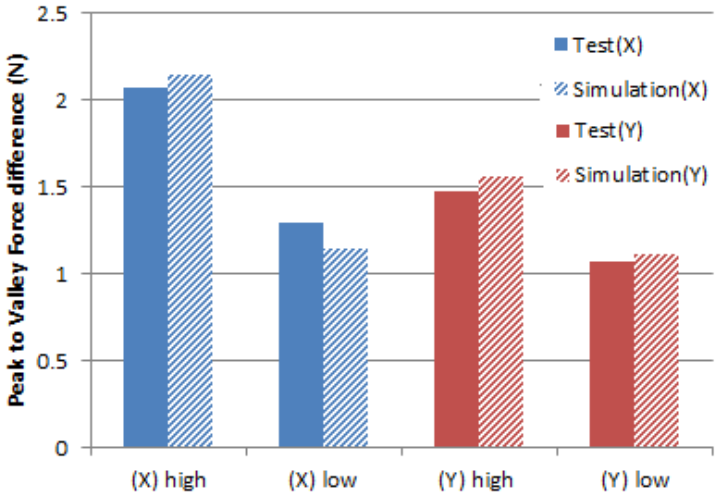

Figure 4.4. Average high and low peak-to-valley force difference observed in test and simulation for test cutting condition feed rate=2µm/flute, DOC=50µm

4.3.2 Composite force model validation

The validation of the composite force model predictions has been done by comparing the experimental forces obtained from machining slots at cutting conditions that include varying feed rate, DOC tile angle and lead angles. The test conditions for both simulation and experiments are listed in Table 4.3.

Table 4.3. Experimental cutting conditions

<table>
<tr><th rowspan="2">test#</th><th rowspan="2">Variable Parameters</th><th colspan="4">Cutting conditions</th></tr>
<tr><th>Feed (µm/flute)</th><th>DOC (µm)</th><th>tilt (°)</th><th>lead (°)</th></tr>
<tr><td>1</td><td rowspan="4">feed rate (µm/flute)</td><td>0.5</td><td rowspan="4">50</td><td rowspan="6">0</td><td rowspan="10">0</td></tr>
<tr><td>2</td><td>1</td></tr>
<tr><td>3</td><td>2</td></tr>
<tr><td>4</td><td>3</td></tr>
<tr><td>5</td><td rowspan="2">DOC (µm)</td><td rowspan="10">2</td><td>30</td></tr>
<tr><td>6</td><td>100</td></tr>
<tr><td>7</td><td rowspan="4">Tilt angle (°)</td><td rowspan="8">50</td><td>-30</td></tr>
<tr><td>8</td><td>-15</td></tr>
<tr><td>9</td><td>15</td></tr>
<tr><td>10</td><td>30</td></tr>
<tr><td>11</td><td rowspan="4">Lead angle (°)</td><td rowspan="4">0</td><td>-30</td></tr>
<tr><td>12</td><td>-15</td></tr>
<tr><td>13</td><td>15</td></tr>
<tr><td>14</td><td>30</td></tr>
</table>

For each test, X- Y- and Z- directional force data for 16 tool revolutions are recorded and the root-mean-square (RMS) force for each direction is used for comparison. Figures 15 and 17 show the RMS X-, Y- and Z- predicted forces from the slip-line model (SL), the composite model with and without runout conditions (SL+ID and SL+ID+RO) as well as forces form experiments for all test conditions listed in Table 4.3. Experimental and simulation forces profiles are listed in Appendix A.

For cutting conditions with 0° tilt and lead angles, Fig. 4.5 shows that the slip-line force model match well with experiment results for varying feed rate and DOC conditions. The addition of indentation model does not largely affect the prediction. This agrees with the indentation weighting function presented in Sec. 3.4.3, that cutting with 0° tool inclination angles does not induce major indentation force due to small radial/tangential cutting speed ratio χ. The only exception is shown in Fig. 4.5-(a), where the indentation model contributes significantly to the z-force prediction in high feed rate condition (3μm/flute). This is due to the fact that large feed rate causes increased radial cutting speed, resulting in large weighing factor μ for the indentation force. The addition of runout model did not cause considerable change in RMS force prediction error.

The force data for two tool revolutions are also plotted in Fig. 4.6. As seen in Fig. 4.6, the composite model with indentation (SL+ID) can accurately predict force profile for cuttings with 0° tool inclination angles.

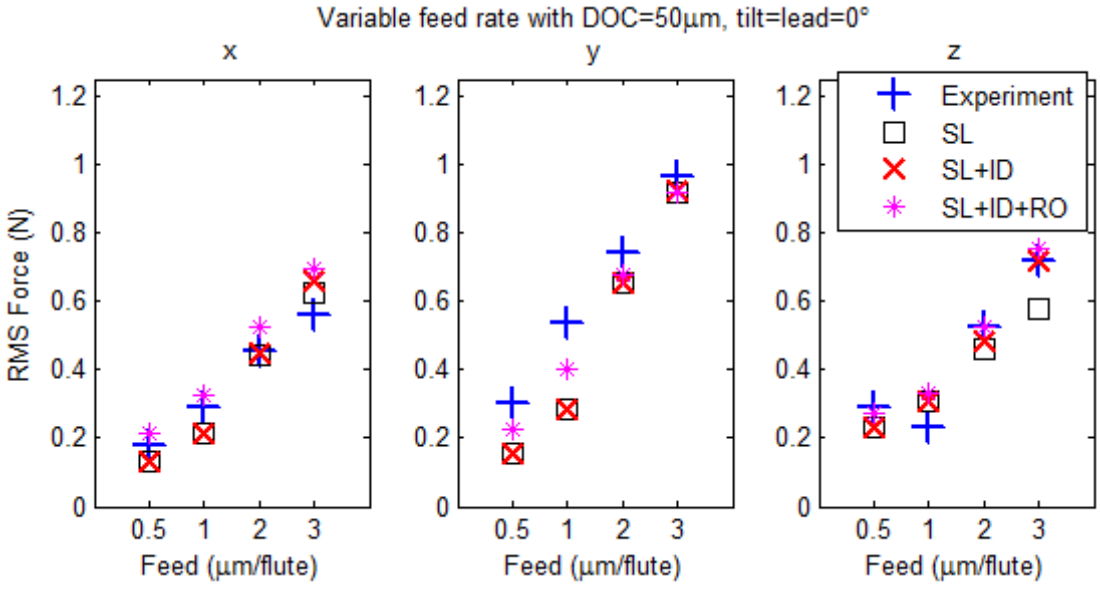

(a)

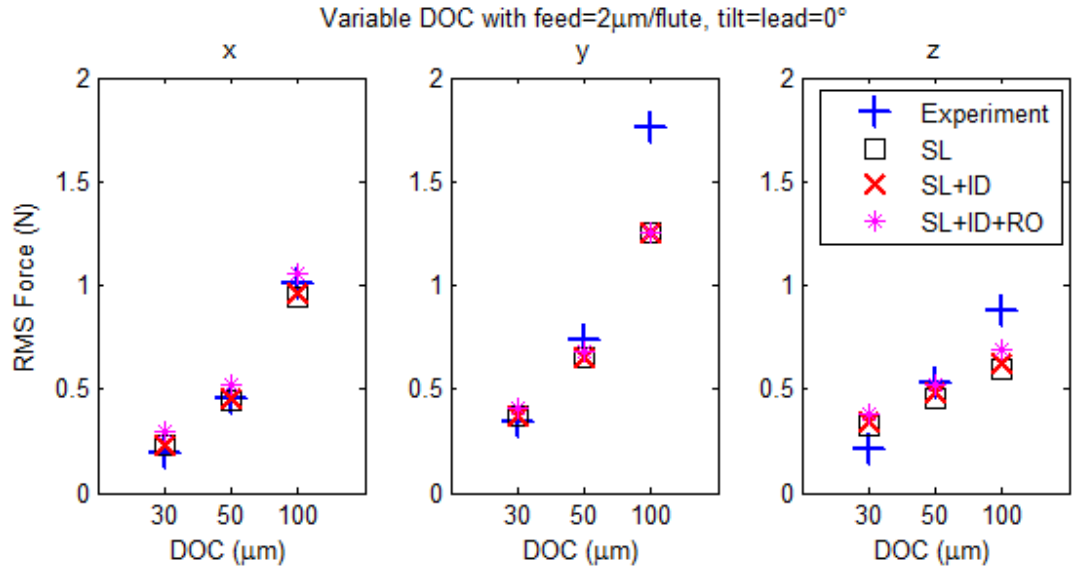

(b)

Figure 4.5. RMS x- y- and z- force comparisons between experiments and simulations for orthogonal cutting with varying (a) feed rate, (b)DOC

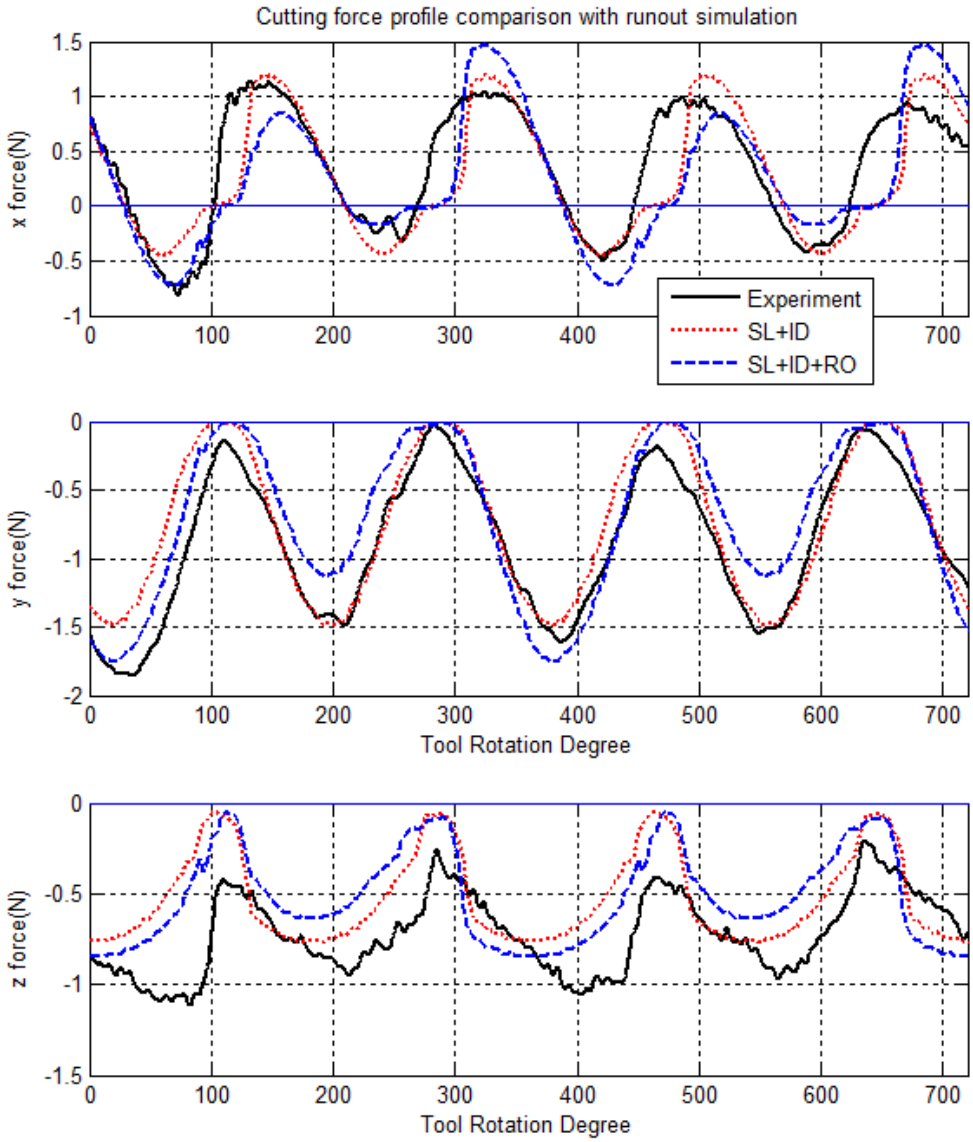

Figure 4.6. Force profile experiment/composite model comparison for test#4, where feed=3μm/flute, DOC=50μm, lead=tilt=0°

Fig. 4.7-(a) shows the comparison of RMS forces for cutting conditions with varying lead angle and 0° tilt angle (tests# 11,12,13,14). As seen in Fig. 4.7-(a), the inclusion of indentation model (ID) significantly improves the force prediction accuracy for the conditions with negative lead angles due to large indentation force occurring in tool tip area during cutting. Since considerable process faults are expected in non-zero lead angle cutting

conditions, the runout parameters estimated using the procedure discussed in Sec. 4.3.1 are used in the simulation. Although Fig. 4.7-(a) does not show significant RMS force improvement due to the runout parameters, it is seen in Fig. 4.8-(a) that the force prediction for test #11 (tilt angle =0°, lead angle =-30°) is significantly improved for X- and Y-directional forces with runout conditions.

Figure 4.7-(b) shows the comparison of experimental and model-predicted forces for cutting conditions with varying tilt angle and 0° lead angle (tests# 7, 8, 9, 10). As seen in Fig.4.7-(b), the composite model (SL+ID) underpredicts cutting forces in positive tilt angle conditions, which represents climb milling processes. Since for climb milling (positive tilt angle), the machining process could be considerably affected by process faults, the composite model with runout parameters are used in the simulation. It is seen the model predictions are considerably improved and match well with the experiments. The force profiles shown in Fig. 4.8 and Fig. 4.9 also show a good match between the simulations and experiments.

It is noticed that the composite model prediction for cutting conditions with negative lead angles and positive tilt angles are less accurate. This observation agrees with the findings by López de Lacalle et al. [45] that higher dimensional errors were found in tests with negative lead angles or positive tilt angles due to larger tool deflection.

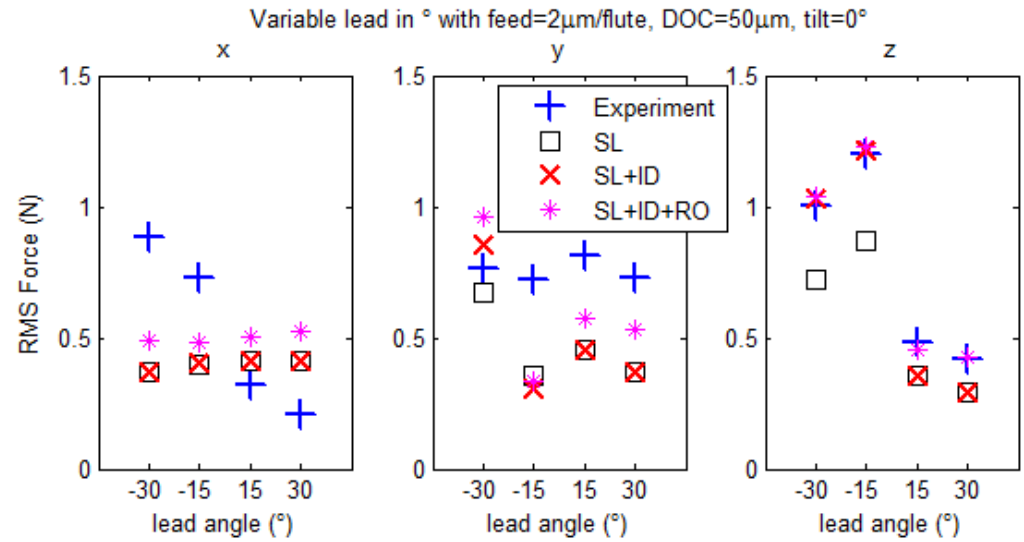

(a)

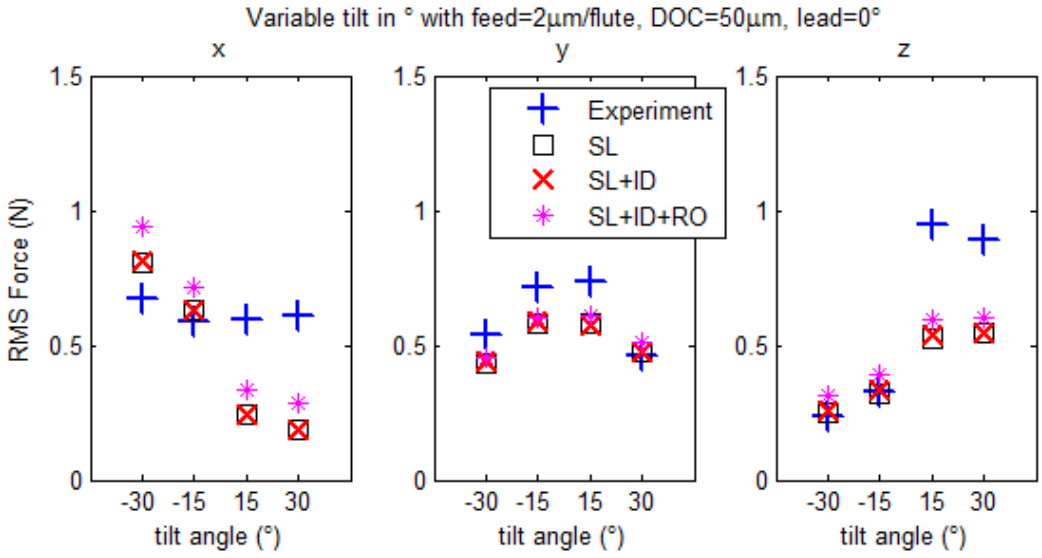

(b)

Figure 4.7. RMS x- y- and z- force/simulation comparison for non-orthogonal cuttings with varying (a) tilt angle, (b)lead angle

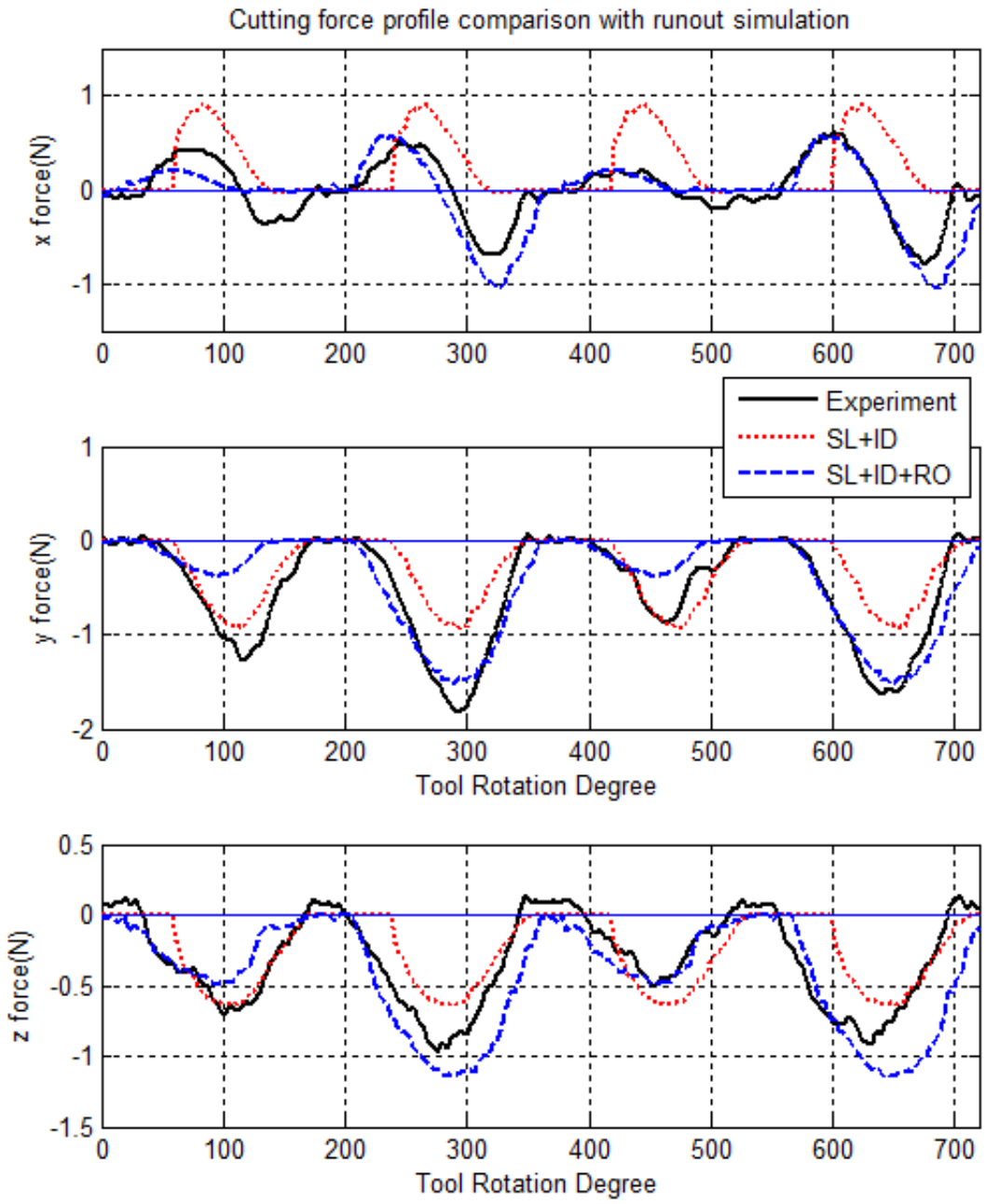

Figure 4.8. Force profile experiment/composite model comparison for test#13, where feed=2μm/flute, DOC=50μm, tilt=0°, lead=15°

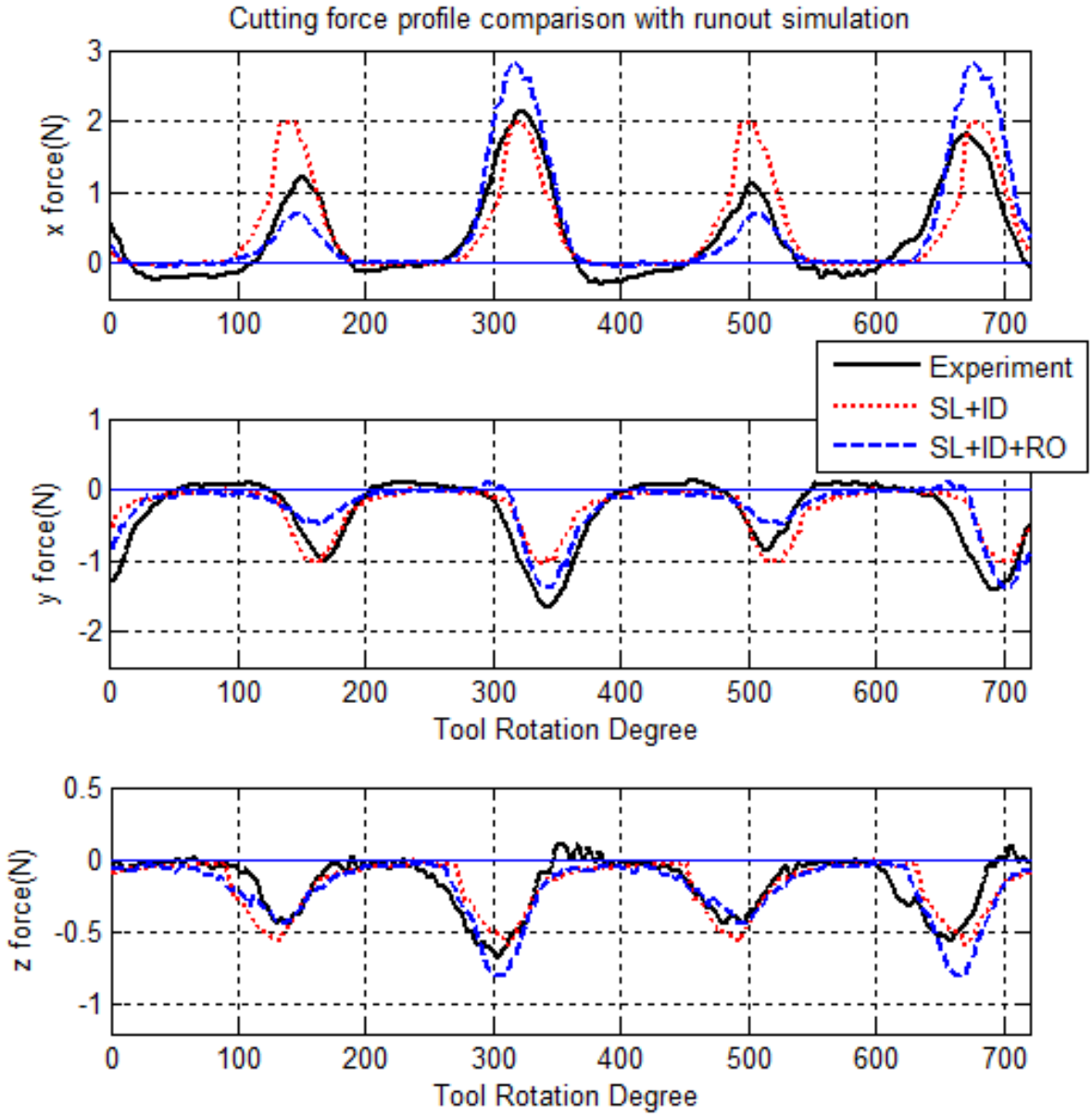

Figure 4.9. Force profile experiment/composite model comparison for test#7, where feed=2μm/flute, DOC=50μm, tilt=-30°, lead=0°

4.4 Summary

This this chapter, the calibration and validation process for the composite five-axis micro-ball end milling force model has been presented. The UIUC five-axis mMT is used to carry out experiments for both calibration and validation processes. First, the unknown parameters

of the slip-line force model are estimated by comparing to the slot-cutting experiment results with cutting conditions that do not induce major indentation force. Secondly, for the indentation force model calibration, experiments have been done to directly plunging into the workpiece, such that the recorded force result is considered mainly contributed by the indentation force. After the parameters for both models are estimated, the runout effect on the cutting force prediction is validated by measuring the runout parameters and compares the simulation force profile to the experiment. Finally, the composite model is validated using slot-cutting experiments RMS forces with cutting conditions that vary in feed rate, DOC, tilt angle and lead angle. The simulation-experiment comparison result has shown that the composite force model is able to predict the RMS forces for most cutting conditions with reasonable accuracy. Also, force profile comparisons show that the composite model can accurately capture the experimental data in each flute. However in the cutting conditions of negative lead angle or positive tilt angle, prediction result is less accurate. The reason for this large error is suspected to be extra tool dynamics in such cutting conditions.

Chapter 5

Model Applications

5.1 Overview

Premature tool failure posts a major challenge to micro-scale ball end milling due to the extreme fragile nature of micro-scale ball end mill [10]. Previous literature has stated that tool failures including tool wear and breakage during end milling operation are closely related to tool force generation during machining [9, 46, 47]. A process planning to prevent large force generation can significantly prolong tool life, thus reducing tool cost and cost of tool changing time. To avoid tool breakage when machining free-form surfaces where chip thickness constantly changes for a constant feed rate, Zhu [9] proposed a chipload prediction-based feed rate scheduling scheme by adjusting feed rate along the ball end milling tool path. However, Chapter 3 has shown that due to the significant cutting edge indentation force induced in cutting conditions with non-zero inclination angles, tool force generation will be different despite the same chip load generation. Therefore, instead of using purely chipload-based method, force prediction-based process planning becomes necessary. Therefore, the composite cutting force model for five-axis micro-ball end milling can be used to predict cutting force for process planning purpose.

The composite five-axis micro-ball end milling force model developed in Chapter 3 requires a large amount of computation time, it is unreasonable to fully simulate the whole tool path during machining. Hence, it is proposed to perform simulation for varying cutting

conditions including feed rate, DOC, tilt and lead angles and compute a look-up table for on-line implementation of process planning. This force look-up table will be generated for every combination of workpiece material and radial depth of cut. Using this look up table, process planning for both feed rate and tool path can be done in order to keep the force level below a pre-determined force boundary, thereby preventing premature tool failure.

The remainder of this chapter will propose two approaches of force prediction-based process planning for large force avoidance. Sect. 5.2 introduces the feed rate scheduling scheme that can slow down the feed rate without modifying the absolute tool orientation when large tool force is predicted ahead in the tool path. However, slowing down the feed rate will cause lower machining efficiency. Alternatively, Sect. 5.3 introduces the tool oriental scheduling scheme that will alter the relative inclination angle between the tool and the workpiece to avoid large force generation without sacrificing the machining time. However, limitation of equipment and workpiece set up will often prevent the use of all tool orientations during machining. Therefore, by utilizing the combination of the feed rate scheduling scheme and the tool orientation scheduling scheme, an optimized process planning can be done to balance machining efficiently and feasibility within the limit of equipment. Sect. 5.4 presents an example of a process planning that utilized both the feed rate scheduling scheme and tool orientation scheduling scheme to achieve cutting force reduction under the constrains of tool orientation. The summary of this Chapter is presented in Sec. 5.5.

5.2 Force prediction-based feed rate scheduling

During the machining of a free-form surface using micro-ball end mill with a constant radial DOC, force generated on the tool is directly affected by feed rate and tool orientation including tilt/lead angles. Due to the change of relative angle between tool and workpiece

along the pre-determined tool path, the lead and tilt angles are subjected to a constant change. Further, as described in 3.4.2, due to relative large cutting edge to chip load ratio in micro-machining, the combination of ploughing/shearing regime and cutting edge indentation effect will significantly increase tool force for certain tool orientations. Therefore, in the proposed method for a given tool orientation in a certain section, if the total force exceeds the pre-determined force for tool failure, the feed rate will be reduced to ensure machining without any interruption.

As an example of a real life machining scenario with process planning, simulation was performed for the situation illustrated in Fig.5.1, where a slot cutting on a ferrite workpiece with concave surface is performed on a five-axis CNC machine with micro-ball end mill. The uncut workpiece surface has radius of 5.0mm, and the maximum gradient on the concave surface was set to 35°, thus the total machining distance is calculated to be 6.11 mm. In the case of fixing the B and C stage angles on the CNC machine, the lead angle between the tool and the workpiece surface ranges from -35° in the beginning of the tool path to 35° at the end of the tool path, while tilt angle is kept to be 0°, and maximum feed rate is limited to 2μm/flute. A two-flute ball end mill of 508μm in diameter and spindle speed of 10,000 rpm is used in the simulation.

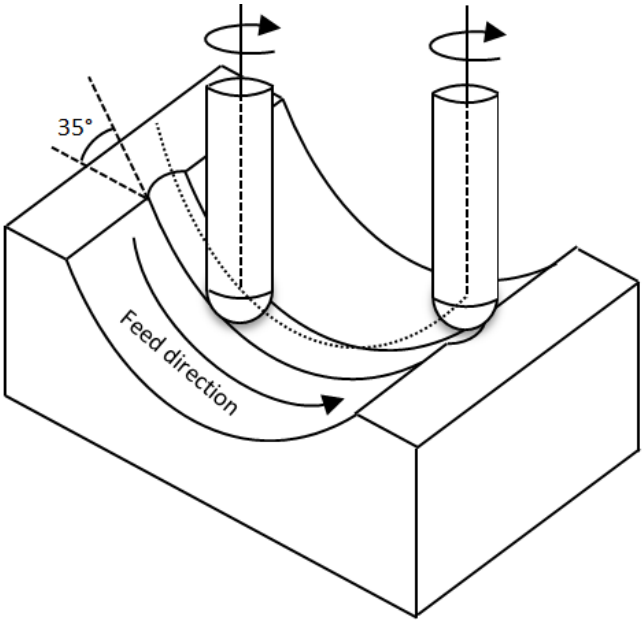

(a)

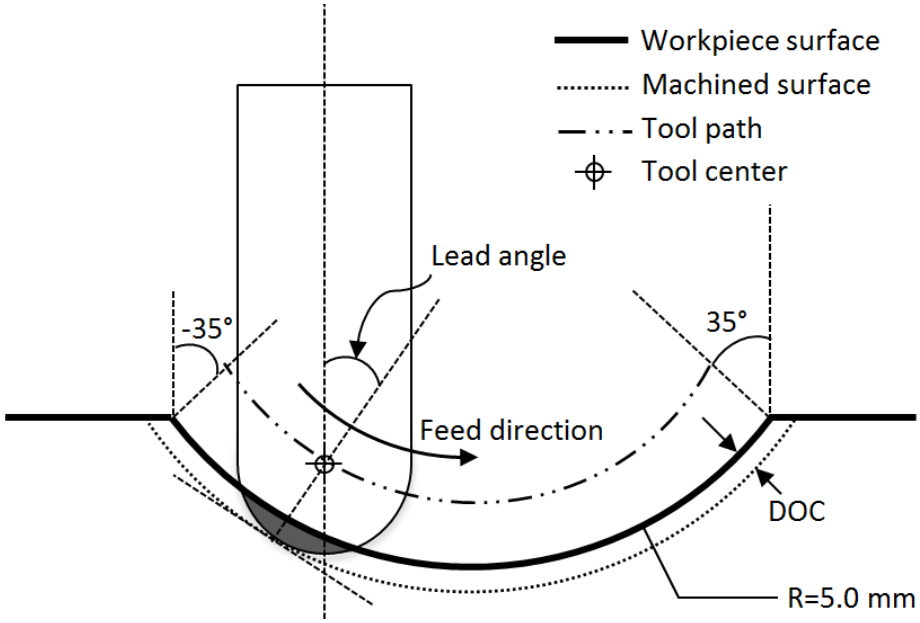

(b)

Figure 5.1 Illustration of slot cutting on a concave surface with fixed B and C stage

The total force exerted on the tool F_{total} is calculated as the norm of forces in the X-, Y- and Z- directions as:

$$F_{total} = \sqrt{F_X^2 + F_Y^2 + F_Z^2}. \quad (5.1)$$

The maximum F_{total} in each tool rotation is also recorded throughout the tool motion. Following the cutting condition illustrated in Fig. 5.1, a look–up table presented here as a three-dimensional surface for maximum F_{total} is created for machining ferrite with cutting condition of DOC= 50µm. Figure 5.2 shows the look-up table as a three-dimensional surface when tilt angle is kept as 0°.

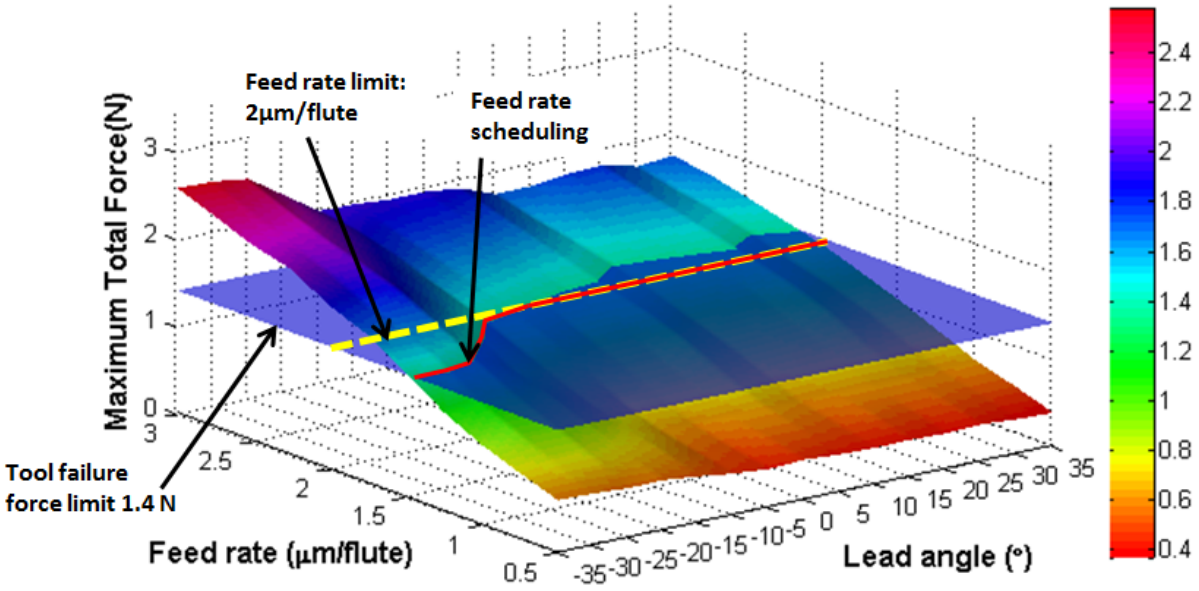

Figure 5.2 Maximum total cutting force look-up table for ferrite workpiece, with cutting conditions of tilt angle = 0° and DOC=50µm.

As seen in Fig. 5.2, when tilt angle is set to 0°, the increase of feed rate and the decrease of lead angle will both increase the maximum total cutting force. As suggested by Tansel et al. [43], the tool life is directly inversely proportional to the cutting force. In order to achieve tool life that is longer than one shift, it is assumed that the maximum tool failure boundary force is 1.4N. Figure 5.3 shows the process of feed rate scheduling for the machining scenario described in Fig. 5.1 using Fig. 5.2.

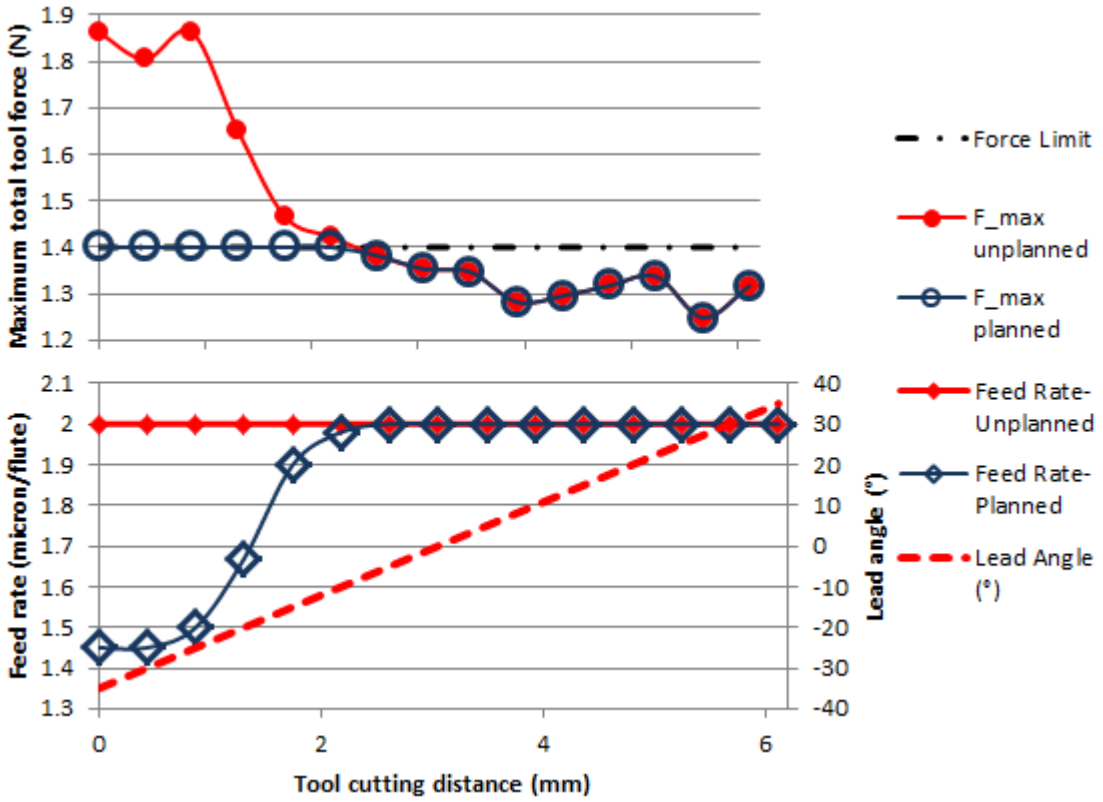

Figure 5.3 Feed rate scheduling process for micro-ball end mill slot cutting on concave surface with tool failure bounday force =1.4N, tilt angle = 0°

As seen in Fig. 5.3, for fixed B and C stage on the CNC machine, the micro-ball end mill will experience large maximum total tool force in the beginning of the tool path, where a large negative lead angle is present. The feed rate scheduling scheme keeps the maximum tool force below 1.4N by decreasing feed rate down to 1.45μm/flute according to the look-up table, then gradually raise the feed rate as the tool proceeds in the concave surface, and tool lead angle becomes less negative. When the tool reaches the point where the regular 2.0μm/flute feed rate will cause tool force below 1.4N, the feed rate was maintained at 2.0μm/flute until the tool reaches the end of path.

5.3 Force prediction-based tool orientation planning

Feed rate scheduling presented in the previous section is able to prevent the total cutting force to exceed a pre-determined force limit. However, simply reducing feed rate will affect

the total machining time. As seen in Chapter 4, the cutting edge indentation with certain lead and tilt angles play a significant role in generating large cutting forces. Therefore, it will be more appropriate to alter the process planning by changing the tilt and lead angles in order to limit the cutting forces.

Note that when machining a free-form surface using a ball end mill, every point on the surface will have a corresponding tool centre location in the X-Y-Z space. A five-axis machine can provide additional two degree of freedom for the tool in the null space, meaning that while machining the same point on the workpiece, the tool orientation can be changed to avoid critical tilt or lead angle.

The composite force model introduced in this thesis is able to generate a maximum force map for all the possible tilt and lead angle for a certain feed rate and DOC. In order to understand the effect of changing tilt and lead angle on the total cutting force, the composite model is used to generate maximum total cutting force for the machining scenario described in Fig. 5.1 with a feed rate of 2μm/flute and DOC of 50μm. Fig. 5.4 shows the maximum tool total force for each combination of tilt and lead angle ranging from -35° to 35°.

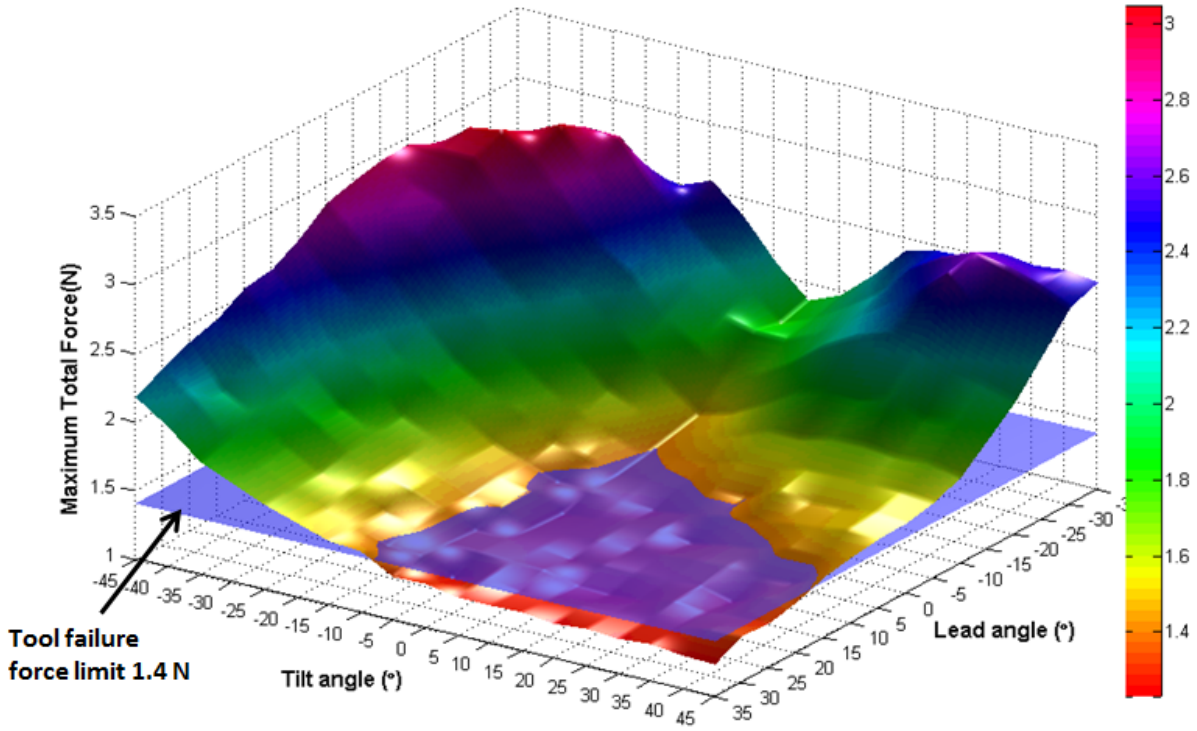

Figure 5.4 Maximum total tool force look-up table for ferrite workpiece, with cutting conditions of feed rate=2µm/flute and DOC=50µm

Figure 5.5 shows the tool orientation scheduling process for the same cutting scenario described in the previous section. In order to keep the maximum total tool force below the 1.4N threshold limit, instead of feed rate reduction, the lead angle was simply kept to -5° instead of -35° from the beginning of the tool path, up to a point where a straight tool position will cause less than 1.4N of maximum total force.

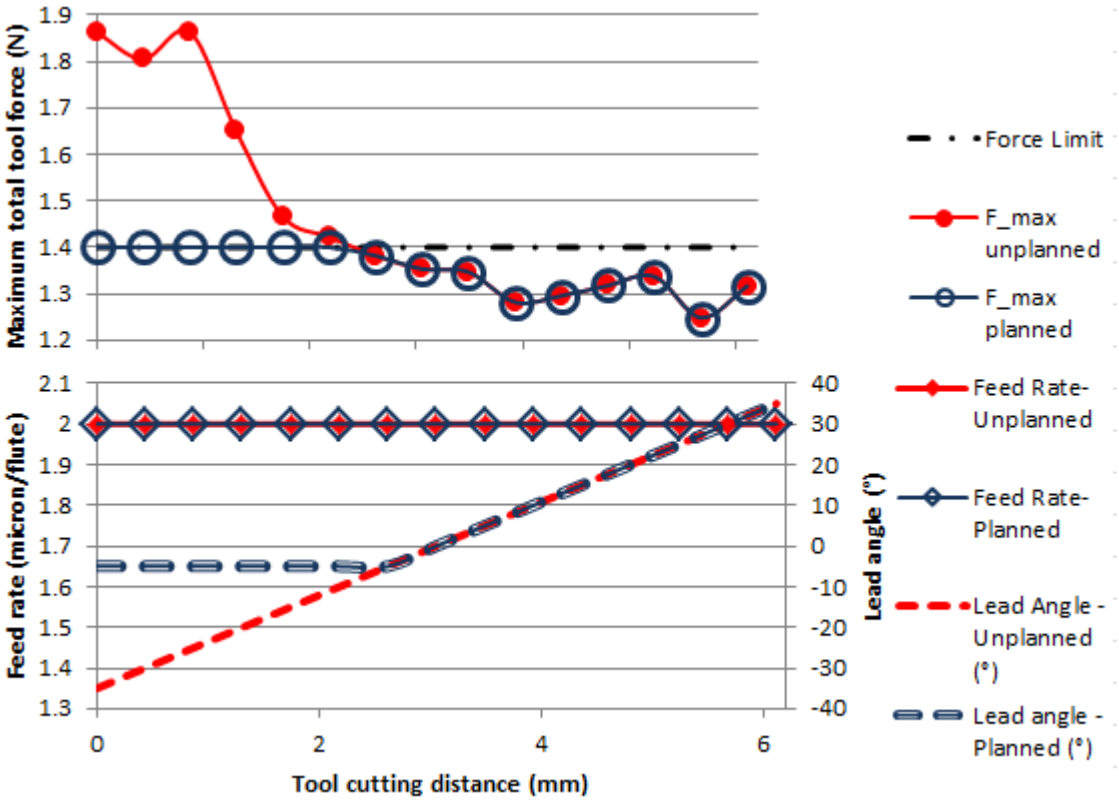

Figure 5.5 Tool orientation scheduling process for micro-ball end mill slot cutting on concave surface with tool failure bounday force =1.4N, tilt angle = 0°

As seen in Fig. 5.5, by changing the lead angle along the tool path, the same force reduction goal can be achieved without reducing the feed rate. For this specific machining simulation, to complete the full 50μm deep slot on the 5.0mm radius concave workpiece surface, the force-prediction-based tool orientation planning scheme will require 9.82 second of machining time, compared to the 10.70 second required by the feed rate scheduling scheme, the machining time is reduced by 8.3%.

5.4 Hybrid process planning scheme

Although the tool orientation scheduling provides a better option than the simple feed rate scheduling in term of machining time, the combination of both process planning scheme could be used to satisfy both feasibility and efficiency. In certain machining scenarios where

a high lead or tilt angle is absolutely necessary due to part feature or machine set up, feed rate can be further reduced for keeping the total cutting force low when the tilt and lead angle limits have been reached.

For example, in the machining condition illustrated in Fig. 5.6, for the feed in Y-direction (into the paper), the tilt angle is limited to maximum -30° when machining the line projected by point A. Assuming that the lead angle is also limited to [-35°, 35°], according to the maximum total cutting force look-up table shown in Fig. 5.7 for various feed rate and lead angle when tilt angle is set as -30°, cutting with any of the lead angles within the limit is impossible to achieve the maximum feed rate of 2μm/flute but keeping the maximum total force below 1.4N. Process planning with feed rate reduction introduced in Sec. 5.2 has to be used.

However, the combined use of feed rate planning and tool orientation-based process planning can minimize the feed rate reduction in such machining scenario. As shown in Fig. 5.7, if the lead angle is kept at 0°, the feed rate needs to be reduced to 1.375μm/flute in order to operate within the tool failure force limit of 1.4N; however, when the lead angle is changed to 35°, the feed rate need to be only reduced to 1.575μm/flute in order to operate within the same force limit. Thus the hybrid process planning scheme provides an option to achieve machining efficiency.

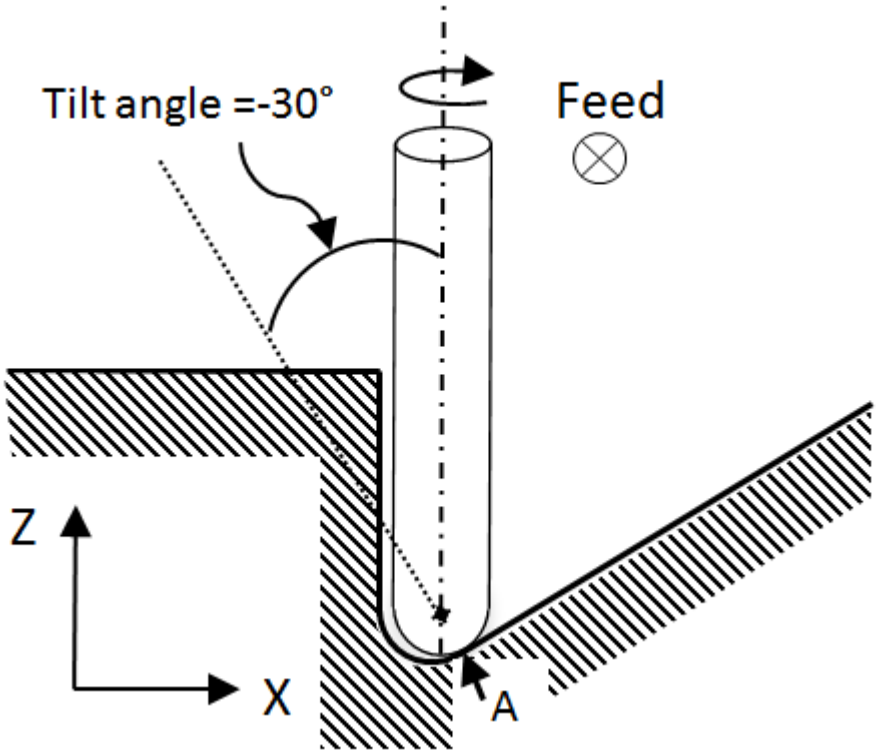

Figure 5.6 Machining with tilt angle being limited to maximum -30°

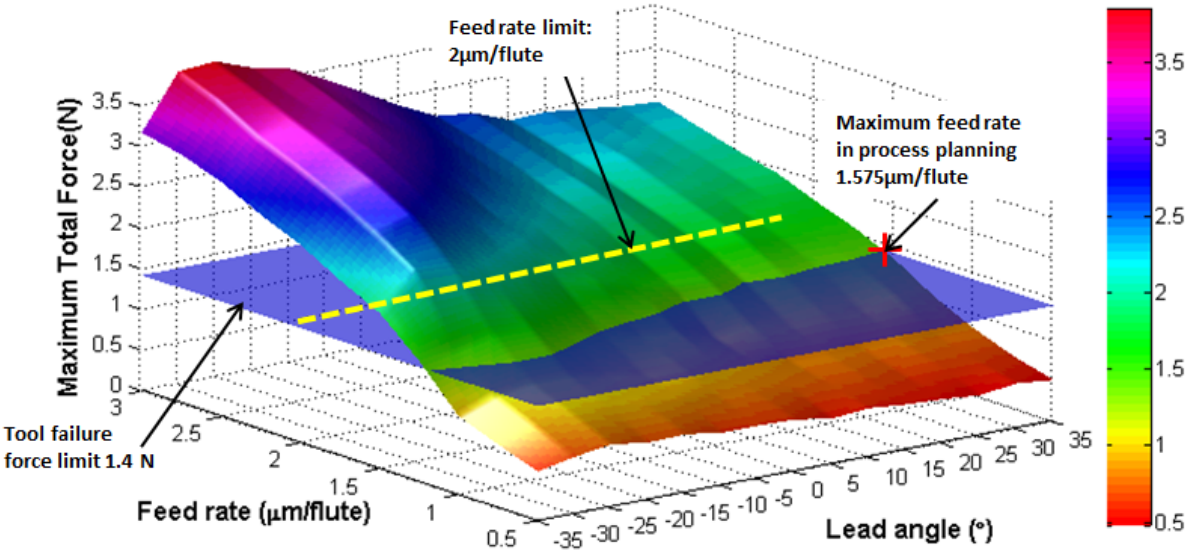

Figure 5.7 Maximum total cutting force look-up table for ferrite workpiece, where tilt angle =-30°, DOC=50μm

5.5 Summary

In this chapter, the force-prediction based five-axis micro-ball end mill process planning

using the composite model developed in Chapter 3 is presented. As the tool life is inversely proportional to the cutting force, the composite model force prediction can be used in process planning to limit the cutting force in order to prolong the tool life. Compared to chip thickness prediction-based process planning, the force-prediction based process planning can provide a more reliable result due to the consideration of indentation force by the composite five-axis ball end mill.

Predicted maximum cutting forces in various cutting conditions along the tool path are essential to effective process planning. Due to the large computation need of the composite model force prediction, a look-up table that stores predicted maximum force for every combination of feed rate, lead angle and tilt angle can be created for specified workpiece material, tool dimensions and DOC.

Using the look-up table, this chapter presented three different approaches of force-prediction based process planning. First, when the look-up table shows large cutting force is ahead in the tool path, the feed rate scheduling approach can slow down the feed rate to the extent that maximum cutting force does not exceed the tool failure boundary. However, simply slowing down the feed rate will affect machining time. Second, by utilizing the extra two degrees of freedom in five-axis machining, the tool orientation scheduling approach can alter the lead and tilt angles of the tool thus lowering the cutting force without slowing down the machining process. Finally, when machine set up and/or part geometry limit the range of tool tilt and lead angle, the combination of both feed rate scheduling and tool orientation scheduling can be used in process planning to reach the optimal cutting condition that balances machining efficiency and feasibility.

Chapter 6

Conclusions and Future Work

6.1 Overview of thesis results.

The object of this research was to develop a force model that predicts the cutting force in five-axis micro-ball end milling. In order to capture the complex cutting edge movement during five-axis ball end milling, a new chip thickness algorithm that based on cutting edge velocity kinematics has been developed. In addition to calculating the chip thickness along the whole cutter flute including the tool tip area, the algorithm also serves as a frame work that incorporates the runout and historical chip thickness calculation. For simulating the engagement condition between the tool and the workpiece, a workpiece updating algorithm has also been presented. This algorithm is used to locally store the historical workpiece elastic recovery condition on the machined surface. In order to predict the cutting force in micro-scale five-axis cutting conditions, a composite force model that consists of a slip-line cutting force model attributing to the minimum chip thickness effect and a tool indentation model that considers the plunging effect has been presented. Both parts in the composite model have been separately calibrated using ball end mill machining experiments. The slip-line force model has been calibrated by slot-cutting experiments that have minimal indentation effect and the indentation model has been calibrated through plunging experiments that have minimal shearing/ploughing force.

The validation of the force model has been done in two steps. First, the effect of runout

on the predicted cutting force has been validated through slip-line force simulation with runout parameters obtained from measurement and the experiment force. Second, the composite cutting force model has been validated by comparing experimental forces from cutting conditions with various feed rate, DOC, tilt angles and lead angles.

A potential application of the force model developed in this thesis has been discussed. Process planning approaches including feed rate scheduling, tool orientation scheduling and combination scheduling to reduce the cutting force and enhance tool life has been illustrated.

6.2 Conclusions

- **Five-axis micro-ball end milling force model development**

1. A discretization scheme for ball end mill force models is proposed based on decomposing the cutting edge into a set of differential circular sectors. Comparing to the conventional disk element discretization, discretizing the polar angle provides a consistent differential arc length for the series of cutting edge points. The consistent arc length discretization in the tool tip area allows detailed force analysis in this area.
2. Velocity kinematics for the discretized cutting edge points are integrated into a chip thickness algorithm. The velocity vector of each cutting edge point is projected in the associated outward radial direction to eliminate tangential components thereby isolating the velocity component associated with chip thickness evolution. Using a similar methodology, both runout and elastic recovery are also accounted for. This unique algorithm is capable of computing the chip thickness for complex tool trajectories typically encountered during five-axis machining such as plunging.
3. The workpiece is represented as a 2D uniform point-wise mesh. An interpolation algorithm has been developed to update workpiece geometry throughout the

simulation while testing for tool-workpiece engagement. As a dual purpose, historical elastic recovery is also stored locally on the workpiece mesh in vector form. This formulation preserves the directionality of elastic recovery for chip thickness calculation for future time increments.

4. A composite cutting force is generated by combining the two force contributions from a shearing/ploughing slip-line cutting force model and the quasi-static indentation model. The slip-line model can predict shearing/ ploughing cutting forces with consideration of the minimum chip thickness effect. The indentation force model can predict the extra radial force produced by the cutting edge when it indents into the workpiece. A weighting function between the slip-line model and indentation force model allows the predicted indentation for to be distributed on the tool area where tool force is more dominated by indentation, and is defined based on a threshold ratio of the tangential velocity to the radial velocity. This formulation emphasizes the use of inherent material properties and requires minimal experimental data fitting.

- **Model calibration and validation**

1. The calibration of the composite force model is done in two steps. First, the unknown parameters of the slip-line cutting force model are obtained using the experiments with cutting conditions 0° tilt/lead angles and do not induce significant indentation force. Slot cutting experiments with high feed rates are used to calibrate the model parameters that affect shearing force calculation. Experiments with low feed rates are used to calibrate the model parameters that affect ploughing force calculation. Second, for the indentation model calibration, a set of plunging tests are performed that allow to estimate the indentation magnitude as well as the weighing factors required in the

composite force model to adjust the contribution from the slip-line model and indentation model.

2. By measuring the runout parameters, the runout effect for a known cutting condition is simulated and the predicted force profile is validated by compared with the experimental data. The composite force model is then validated against the experimental five-axis cutting force data obtained from cutting tests with various cutting conditions. The cutting conditions employed in the tests include varying levels of feed rate, DOC, tilt and lead angles, and represent typical five-axis machining tool movements.
3. It is shown that the simulation is able to match the experimental data with reasonable accuracy for most tool orientations. For cutting conditions include large feed rate and tool plunging movements, the inclusion of the indentation force model clearly improves the prediction accuracy over the prediction purely from the slip-line model. For cutting conditions with high levels of tilt and lead angles, the model underpredicts the cutting force because the model does not take into account the effect of tool deflection and system dynamics.

- **Model application**

1. The five-axis micro-ball end milling model developed in this thesis is capable of generating a process plan for five-axis machining of free form surfaces. For a certain tool, workpiece material and DOC, a maximum tool force look-up table can be created using the composite cutting force model for a range of cutting conditions. Using this look up table, process planning for both feed rate and tool path can be done

in order to keep the force level below a pre-determined force boundary, thereby preventing premature tool failure.

2. Process planning approaches of force prediction-based feed rate scheduling and tool orientation scheduling are discussed in this thesis. The feed rate scheduling scheme allows feed rate to be reduced if the cutting force exceeds the target force level. However reducing the feed rate can cause an increase of machining time. The tool orientation scheduling scheme, on the other hand, makes use of the extra two degrees of freedom of the five-axis machine and allows reducing of the cutting force by changing the tool tilt and lead angles. For cases where the change in tool orientations is limited to a smaller range by the machine set up, the combination of the feed rate scheduling and tool orientation scheduling scheme can further improve the process planning to accommodate both machining efficiency and feasibility.

6.3 Recommendations for Future work

Several areas of potential future research are proposed here based on the results of this thesis:

- **Cutting force model:** Although the composite five-axis micro-ball end milling force model can predict tool force in various cutting conditions with reasonable accuracy, the prediction error differences between cutting conditions with 0° tool inclination angle non-zero tilt/lead angles still present. A more in-depth study is needed to better understand the effects of the shear angle, nominal rake angle, friction factors and other slip-line filed angles on the cutting and thrusting force components in the orthogonal cutting conditions. A universal calibration procedure for wider range of workpiece material in orthogonal cutting is also

desired. In addition, the extension of the composite force model to micro-cutting tools other than ball end mill that also experiences both cutting and indentation effects, such as micro-bull nose end mill and micro-chamfer end mill, is desired.

- **Workpiece update algorithm:** The current workpiece update algorithm is an effective way of serving the dual purpose of tool registration and historical chip thickness storage. However, it is based on a 2-D architecture where only one Z-height data on each X-Y- location of the workpiece surface, which means that cutting simulation in ball end mill undercut operations are not possible. When the tool is cutting a workpiece surface where another uncut part of the workpiece is above the same X-Y- location, more than one Z-height data is needed to represent the overlapped workpiece area. Therefore, instead of the current 2-D discretization, a new version of the workpiece structure that discretizes the workpiece body as a 3-D point mesh is needed for undercut simulation.
- **Machined surface conditions:** The workpiece updating algorithm proposed in this thesis has the potential to simulate machined surface condition. If the historical workpiece surface recovery stored in the X-Y- location can be presented as a permanent increment of surface Z- height, the surface mark caused by ploughing/rubbing or surface roughness can potentially be simulated. This feature would be beneficial to study the effects of different cutting conditions and runout conditions on machined surfaces.
- **Dynamic process fault estimation:** This thesis has only incorporated static shank runout model presented by [1], however, more complex dynamics runout model for micro-end milling in high speed machining is available. According to [1], instead of treating the cutting tool as completely rigid, it can be modelled as a

Timoshenko beam such that the tool rotary inertia, shear deformation and gyroscopic moments can be considered in modeling the tool dynamics. The large shank and small taper design of micro-ball end milling can also introduce a second mode of cutting edge runout beyond the shank runout model. The inclusion of a tool dynamics model can better assist the understanding of cutting force behaviour in high speed micro-machining.

- **Path generation algorithm:** An automatic tool path generation algorithm is possible with the presence of this composite force model and further study of the machined surface. As different cutting condition will also result in different surface finish qualities, a cost function can be developed to consider both the tool force generation and surface finish qualities. A new interpolation scheme can be developed to find the local minimum of the cost function by changing cutting conditions, thereby generating an optimal feed rate and tool orientation profile along the tool path. By automatically choosing optimal tool orientation with general consideration of tool force and surface finish can greatly enhance manufacturing capability and drastically reduce cost.

List of References

[1] Jun, M. B., Liu, X., DeVor, R. E., 2006, "Investigation of the Dynamics of Microend Milling—Part I: Model Development," Journal of Manufacturing Science and Engineering, 128(4) pp. 893-900.

[2] Tuysuz, O., and Altıntaş, Y., 2013, "Prediction of Cutting Forces in Three and Five-Axis Ball-End Milling with Tool Indentation Effect," International Journal of Machine Tools and Manufacture, 66pp. 66-81.

[3] Ehmann, K. F., DeVor, R. E., Kapoor, S. G., 2008, "Design and Analysis of Micro/Meso-Scale Machine Tools," Smart Devices and Machines for Advanced Manufacturing, pp. 283-318.

[4] Liu, X., DeVor, R. E., Kapoor, S. G., 2005, "The Mechanics of Machining At the Microscale: Assessment of the Current State of the Science," Journal of Manufacturing Science and Engineering, 126(4) pp. 666-678.

[5] Malekian, M. e. a., 2009, "Mechanistic Force Modeling of Micro Ball End Milling Processes," Trans NAMRI/SME, 37pp. 67-74.

[6] Phillip, A. G., 2008, "Development and Evaluation of a Five-Axis Micro/Meso-Scale Machine Tool," Master's Thesis, University of Illinois at Urbana-Champaign, .

[7] Gietzelt, T., Eichhorn, L., and Schubert, K., 2008, "Manufacturing of Microstructures with High Aspect Ratio by Micromachining," Microsystem Technologies, 14(9-11) pp. 1525-1529.

[8] Lazoglu, I., Boza, Y., and Erdimb, H., 2011, "Five-Axis Milling Mechanics for Complex Free Form Surfaces," CIRP Annals - Manufacturing Technology, 60(1) pp. 117-120.

[9] Zhu, R., Kapoor, S. G., and DeVor, R. E., 2000, "Mechanistic Modeling of the Ball End Milling Process for Multi-Axis Machining of Free-Form Surfaces," Journal of Manufacturing Science and Engineering, 123(3) pp. 369-379.

[10] Tansel, I., Rodriguez, O., Trujillo, M., 1998, "Micro-End-Milling – I. Wear and Breakage," International Journal of Machine Tools and Manufacture, 38(12) pp. 1419-1436.

[11] Erdim, H., Lazoglu, I., and Ozturk, B., 2006, "Feedrate Scheduling Strategies for Free-Form Surfaces," International Journal of Machine Tools and Manufacture, 46(7-8) pp. 747-757.

[12] Sabberwal, A. J. P., and Koenigsberger, F., 1961, "Chip Section and Cutting Force during the Milling Operation," CIRP Annals - Manufacturing Technology, 10(3) pp. 62.

[13] Kline, W. A., DeVor, R. E., and Lindberg, J. R., 22, "The Prediction of Cutting Forces in End Milling with Application to Cornering Cuts," International Journal of Machine Tool Design and Research, 1(1982) pp. 7-22.

[14] Yucesan, G., Xie, Q., and Bayoumi, A. E., 1993, "Determination of Process Parameters through a Mechanistic Force Model of Milling Operations," International Journal of Machine Tools and Manufacture, 33(4) pp. 627-641.

[15] Martellotti, M. E., 1941, "An Analysis of the Milling Process," Transactions of ASME, 63pp. 677.

[16] Vogler, M. P., Kapoor, S. G., and DeVor, R. E., 2005, "On the Modeling and Analysis of Machining Performance in Micro-Endmilling, Part II: Cutting Force Prediction," Journal of Manufacturing Science and Engineering, 126(4) pp. 695-705.

[17] Lee, P., and Altıntaş, Y., 1996, "Prediction of Ball-End Milling Forces from Orthogonal Cutting Data," International Journal of Machine Tools and Manufacture, 36(9) pp. 1059-1072.

[18] Altıntaş, Y., and Lee, P., 1998, "Mechanics and Dynamics of Ball End Milling," Journal of Manufacturing Science and Engineering, 120(4) pp. 684-692.

[19] Sutherland, J. W., 1987, "A Dynamic Model of the Cutting Force System in the End Milling Process," Thesis (Ph. D.)--University of Illinois at Urbana-Champaign, pp. 258-271.

[20] Engin, S., and Altıntaş, Y., 2001, "Mechanics and Dynamics of General Milling Cutters.: Part I: Helical End Mills," International Journal of Machine Tools and Manufacture, 41(15) pp. 2195-2212.

[21] Yang, M., and Park, H., 1991, "The Prediction of Cutting Force in Ball-End Milling," International Journal of Machine Tools and Manufacture, 31(1) pp. 45-54.

[22] Fard, M. J. B., and Bordatchev, E. V., 2013, "Experimental Study of the Effect of Tool Orientation in Five-Axis Micro-Milling of Brass using Ball-End Mills," The International Journal of Advanced Manufacturing Technology, 67(5-8) pp. 1079-1089.

[23] Sonawane, H., and Joshi, S. S., 2015, "Analytical Modeling of Chip Geometry in High-Speed Ball-End Milling on Inclined Inconel-718 Workpieces," Journal of Manufacturing Science and Engineering, 137(1) .

[24] Yuan, Z. J., Zhou, M., and Dong, S., 1996, "Effect of Diamond Tool Sharpness on Minimum Cutting Thickness and Cutting Surface Integrity in Ultraprecision Machining," Journal of Materials Processing Technology, 62(4) pp. 327-330.

[25] Liu, X., Vogler, M. P., Kapoor, S. G., 2004, "Micro-endmilling with meso-machine-tool system," NSF Design, Service and Manufacturing Grantees and Research Conference Proc.
, Anonymous Dallas, TX, 1, pp. 1-9.

[26] Waldorf, D. J., DeVor, R. E., and Kapoor, S. G., 1998, "A Slip-Line Field for Ploughing during Orthogonal Cutting," Journal of Manufacturing Science and Engineering, 120(4) pp. 693-699.

[27] Fang, N., 2003, "Slip-Line Modeling of Machining with a Rounded-Edge tool—Part I: New Model and Theory," Journal of the Mechanics and Physics of Solids, 51(4) pp. 715-742.

[28] Jin, X., and Altıntaş, Y., 2011, "Slip-Line field Model of Micro-Cutting Process with Round Tool Edge Effect," Journal of Materials Processing Technology, 211(3) pp. 339-355.

[29] Kountanya, R. K., and Endres, W. J., 2001, "A high-magnification experimental study of orthogonal cutting with edge-honed tools," Proceedings of ASME International Mechanical Engineering Congress and Exposition, Anonymous pp. 157-164.

[30] Nakayama, K., and Tamura, K., 1968, "Size Effect in Metal-Cutting Force," Journal of Manufacturing Science and Engineering, 90(1) pp. 119-126.

[31] Wu, D. W., 1989, "A New Approach of Formulating the Transfer Function for Dynamic Cutting Processes," Journal of Manufacturing Science and Engineering, 111(1) pp. 37-47.

[32] Endres, W. J., DeVor, R. E., and Kapoor, S. G., 1995, "A Dual-Mechanism Approach to the Prediction of Machining Forces, Part 1: Model Development," Journal of Engineering for Industry, 117(4) .

[33] Narayanan, K., Ranganath, S., and Sutherland, J. W., 1997, "A dynamic model of the cutting force system in peripheral milling characterizing the effects of flank face interference," Proceedings of the ASME Annual Meeting, Anonymous MED, 6-2, pp. 143-151.

[34] To, S., Cheung, C. F., and Lee, W. B., 2001, "Influence of Material Swelling on Surface Roughness in Diamond Turning of Single Crystals," Materials Science and Technology, 17(10) pp. 102-108.

[35] Bao, W. Y., and Tansel, I. N., 2000, "Modeling Micro-End-Milling Operations. Part II: Tool Run-Out," International Journal of Machine Tools and Manufacture, 40(15) pp. 2175-2192.

[36] Li, C., Lai, X., Li, H., 2007, "Modeling of Three-Dimensional Cutting Forces in Micro-End-Milling," Journal of Micromechanics and Microengineering, 17(4) .

[37] Bao, W. Y., and Tansel, I. N., 2000, "Modeling Micro-End-Milling Operations. Part III: Influence of Tool Wear," International Journal of Machine Tools and Manufacture, 40(15) pp. 2193-2211.

[38] Sutherland, J. W., and DeVor, R. E., 1986, "An Improved Method for Cutting Force and Surface Error Prediction in Flexible End Milling Systems," Journal of Manufacturing Science and Engineering, 108(4) pp. 269-279.

[39] Altıntaş, Y., 2000, "Manufacturing Automation: Metal Cutting Mechanics, Machine Tool Vibrations and CNC Design," Cambridge University Press, New York, .

[40] Srinivasan, L. N., and Ge, Q. J., 1996, "Parametric Continuous and Smooth Motion Interpolation," Journal of Mechanical Design, 118(4) pp. 494-498.

[41] Erkorkmaz, K., and Altıntaş, Y., 2001, "High Speed CNC System Design. Part I: Jerk Limited Trajectory Generation and Quintic Spline Interpolation," International Journal of Machine Tools and Manufacture, 41(9) pp. 1323-1345.

[42] Sencer, B., and Altıntaş, Y., 2008, "Feed Optimization for Five-Axis CNC Machine Tools with Drive Constraints," International Journal of Machine Tools and Manufacture, 48(7-8) pp. 733-745.

[43] Tansel, I. N., Arkan, T. T., Bao, W. Y., 2000, "Tool Wear Estimation in Micro-Machining.: Part I: Tool Usage–cutting Force Relationship," International Journal of Machine Tools and Manufacture, 40(4) pp. 599-608.

[44] Hughes, T.J.R., 2000, "The finite element method: linear static and dynamic finite element analysis," Dover Publications, .

[45] López de Lacalle, L. N., Lamikiz, A., Sánchez, J. A., 2004, "Effects of Tool Deflection in the High-Speed Milling of Inclined Surfaces," The International Journal of Advanced Manufacturing Technology, 24(9-10) pp. 621-631.

[46] Yesilyurt, I., 2006, "End Mill Breakage Detection using Mean Frequency Analysis of Scalogram," International Journal of Machine Tools and Manufacture, 46(3-4) pp. 450-458.

[47] Miyaguchi, T., Masudaa, M., Takeokab, E., 2001, "Effect of Tool Stiffness upon Tool Wear in High Spindle Speed Milling using Small Ball End Mill," Precision Engineering, 25(2) pp. 145-154.

Appendix A

Measured and simulated cutting forces for slot cutting tests

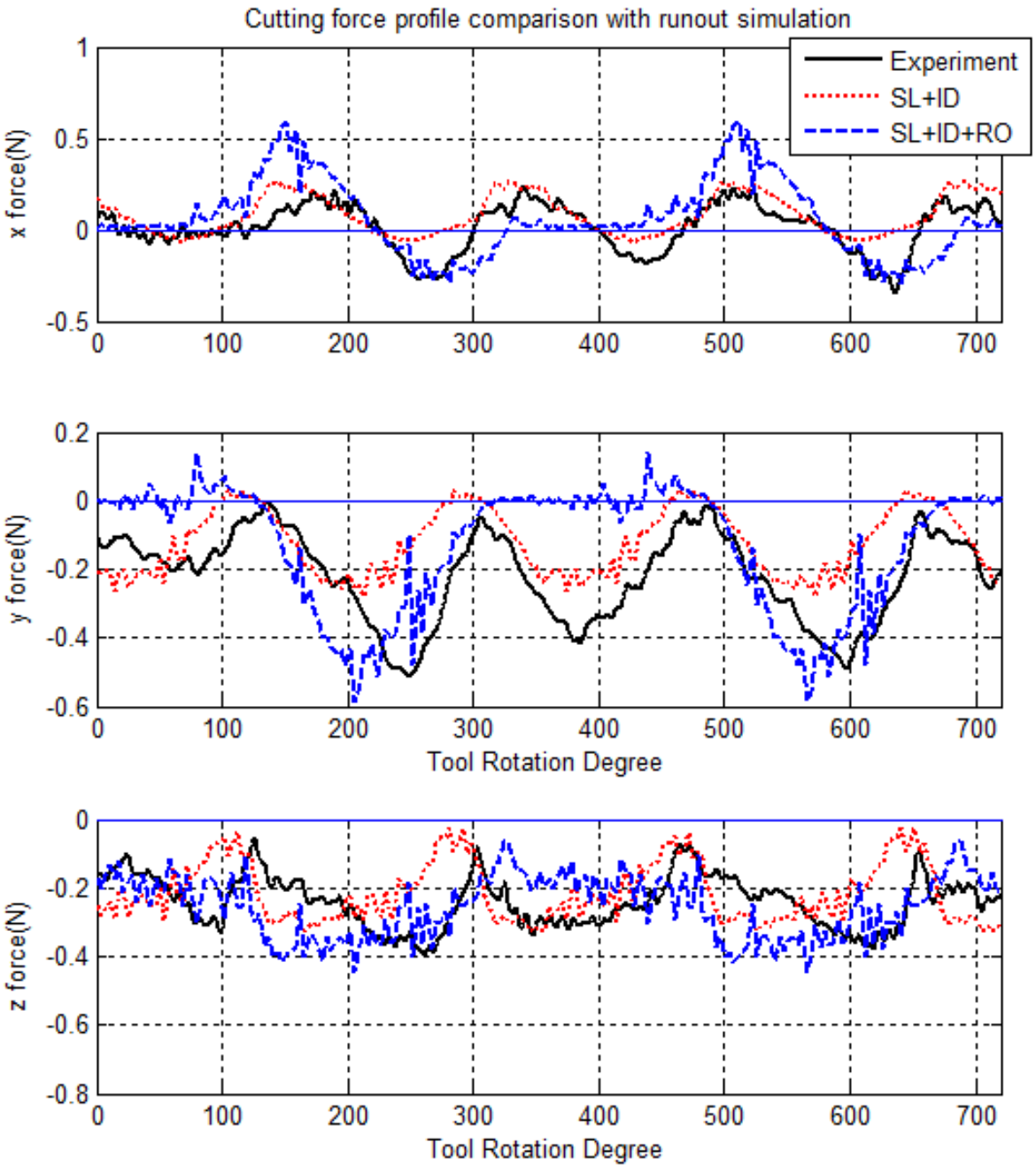

Figure A.1 Measured and simulated cutting forces – Test #1

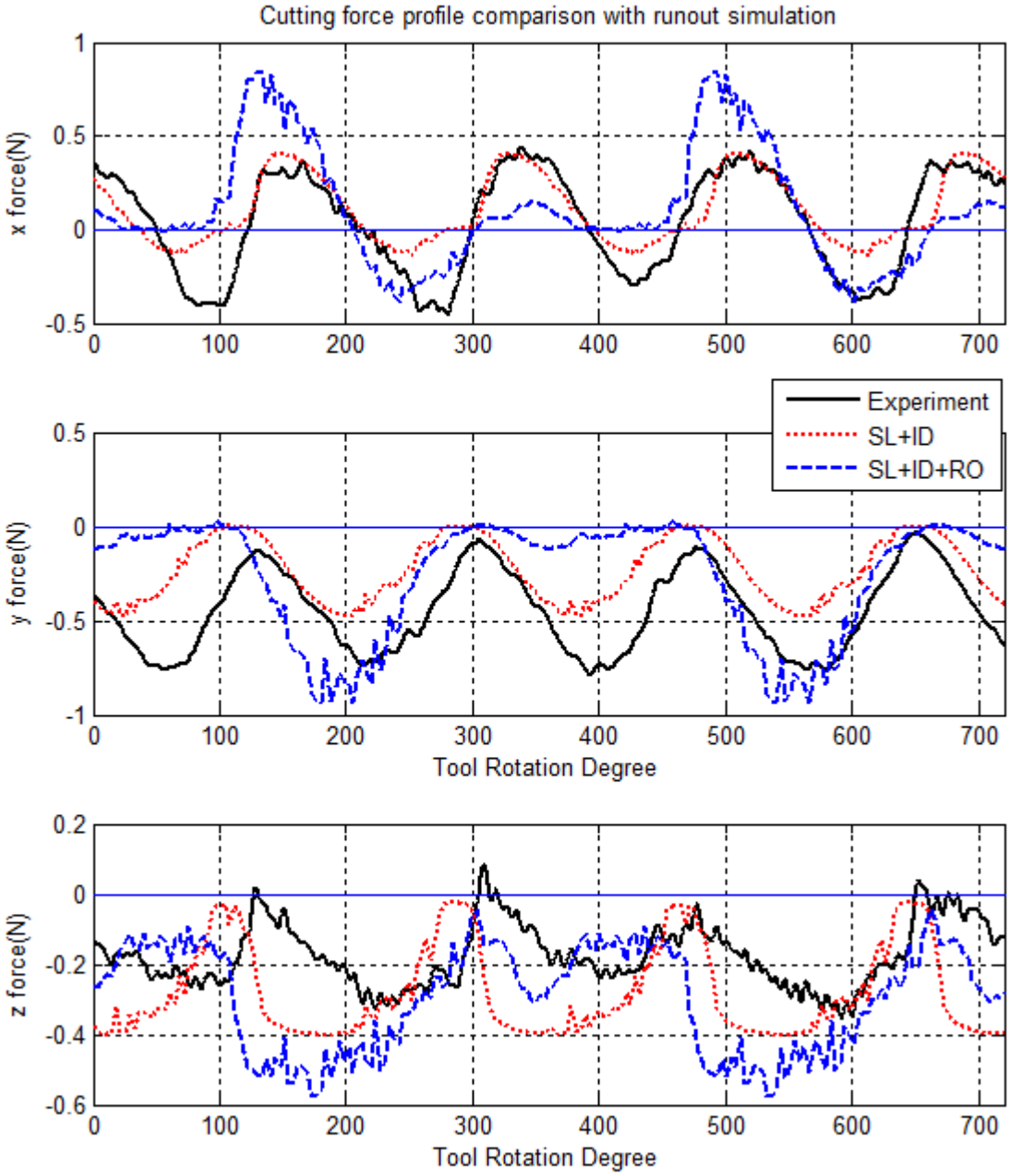

Figure A.2 Measured and simulated cutting forces – Test #2

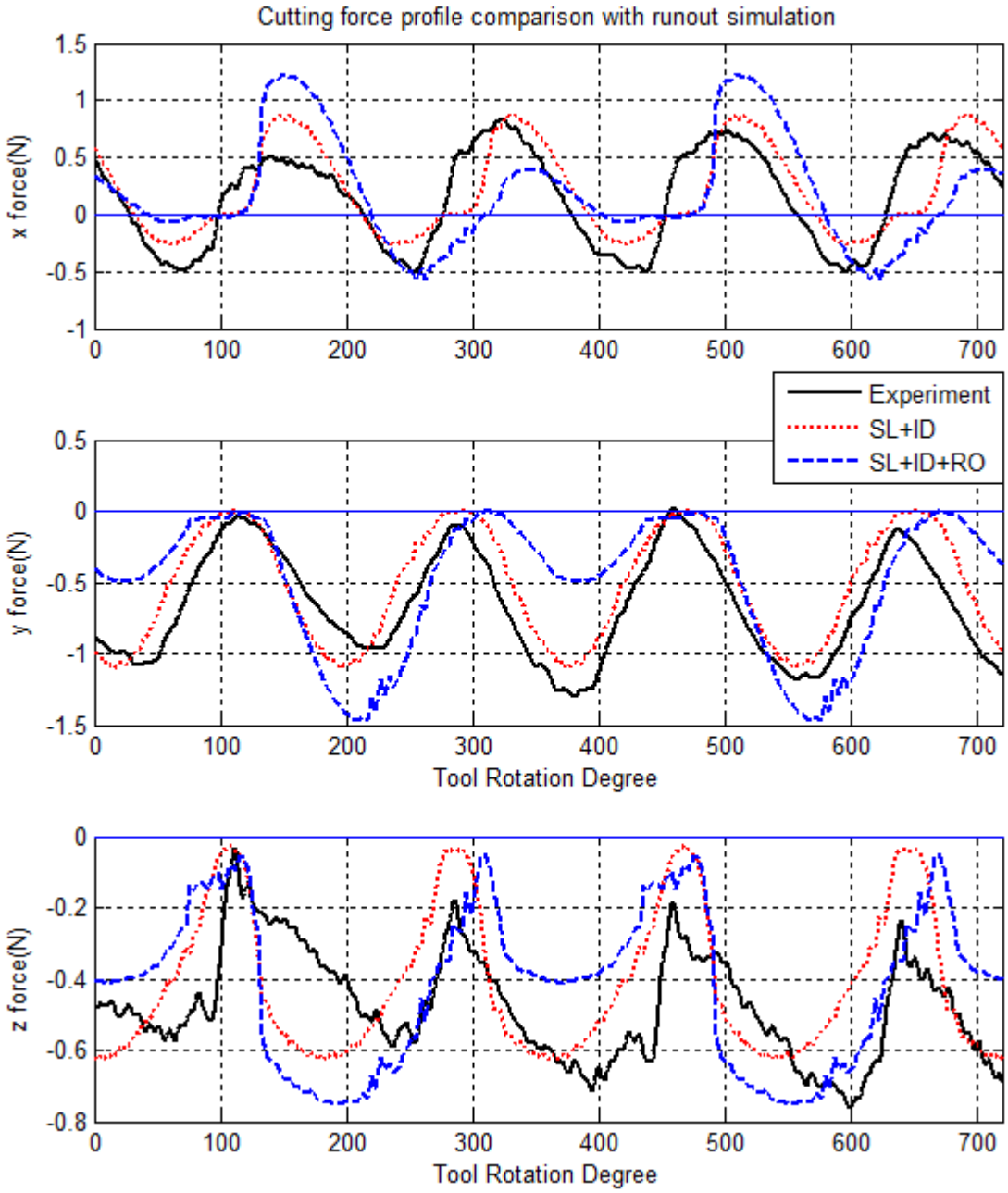

Figure A.3 Measured and simulated cutting forces – Test #3

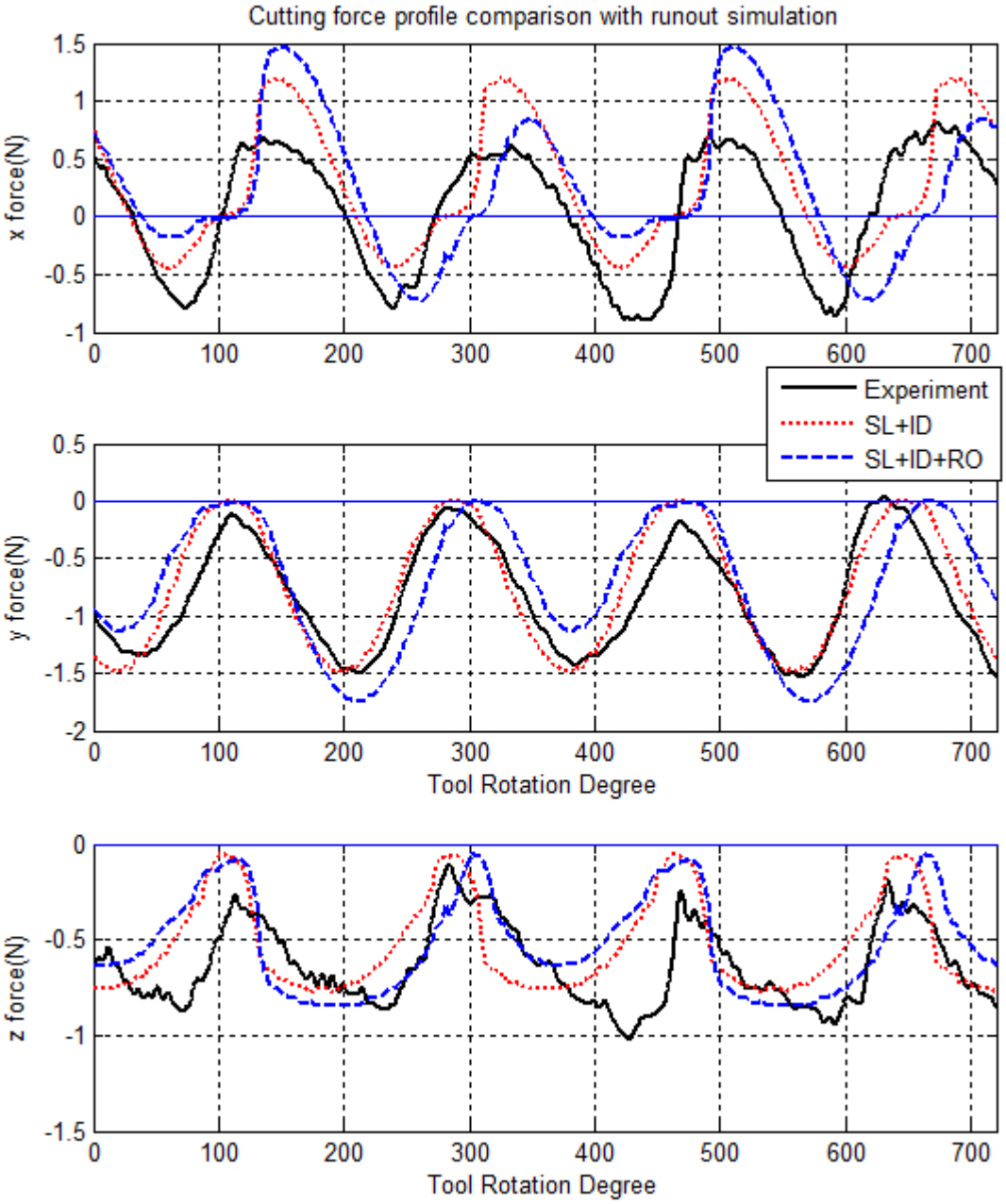

Figure A.4 Measured and simulated cutting forces – Test #4

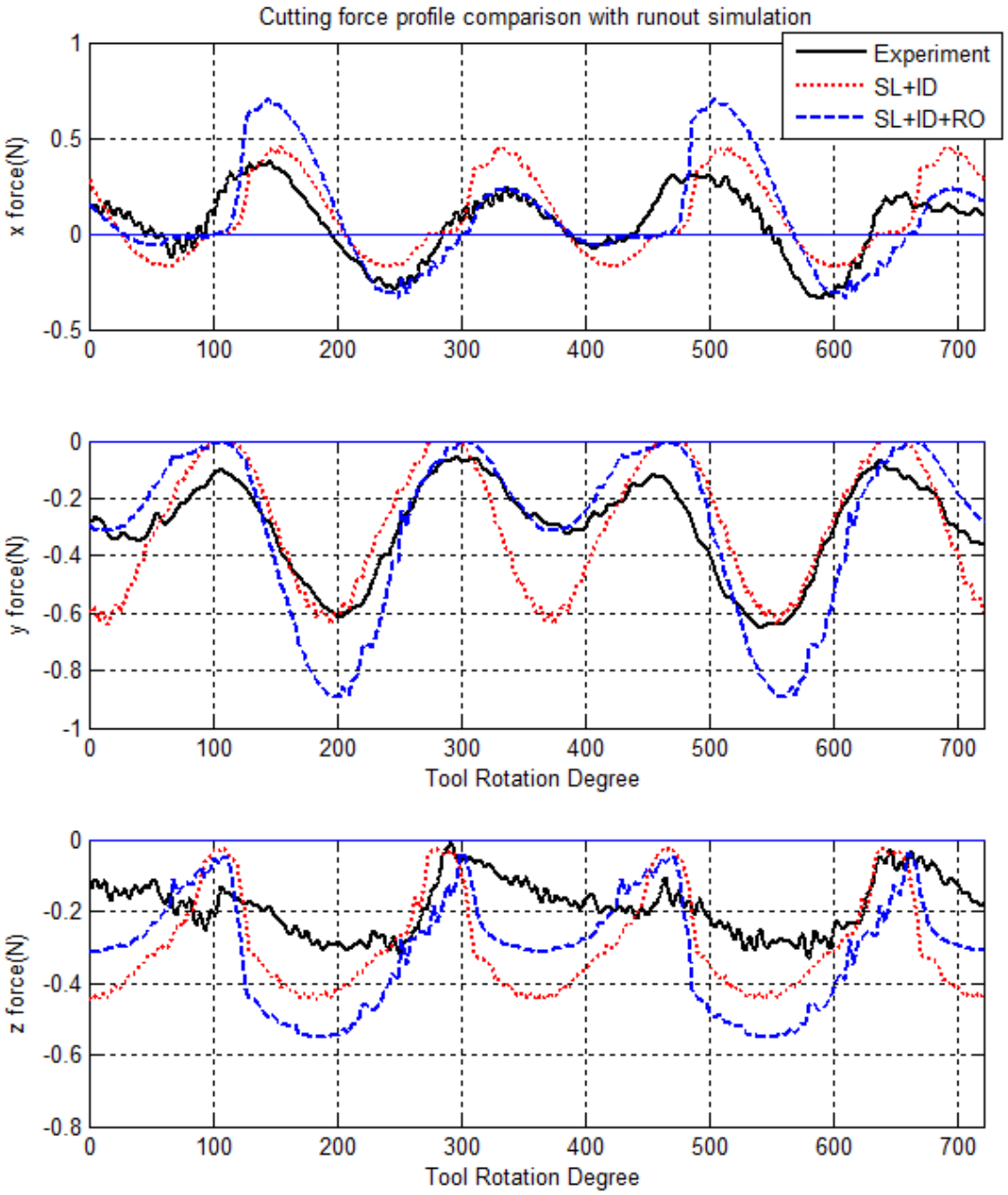

Figure A.5 Measured and simulated cutting forces – Test #5

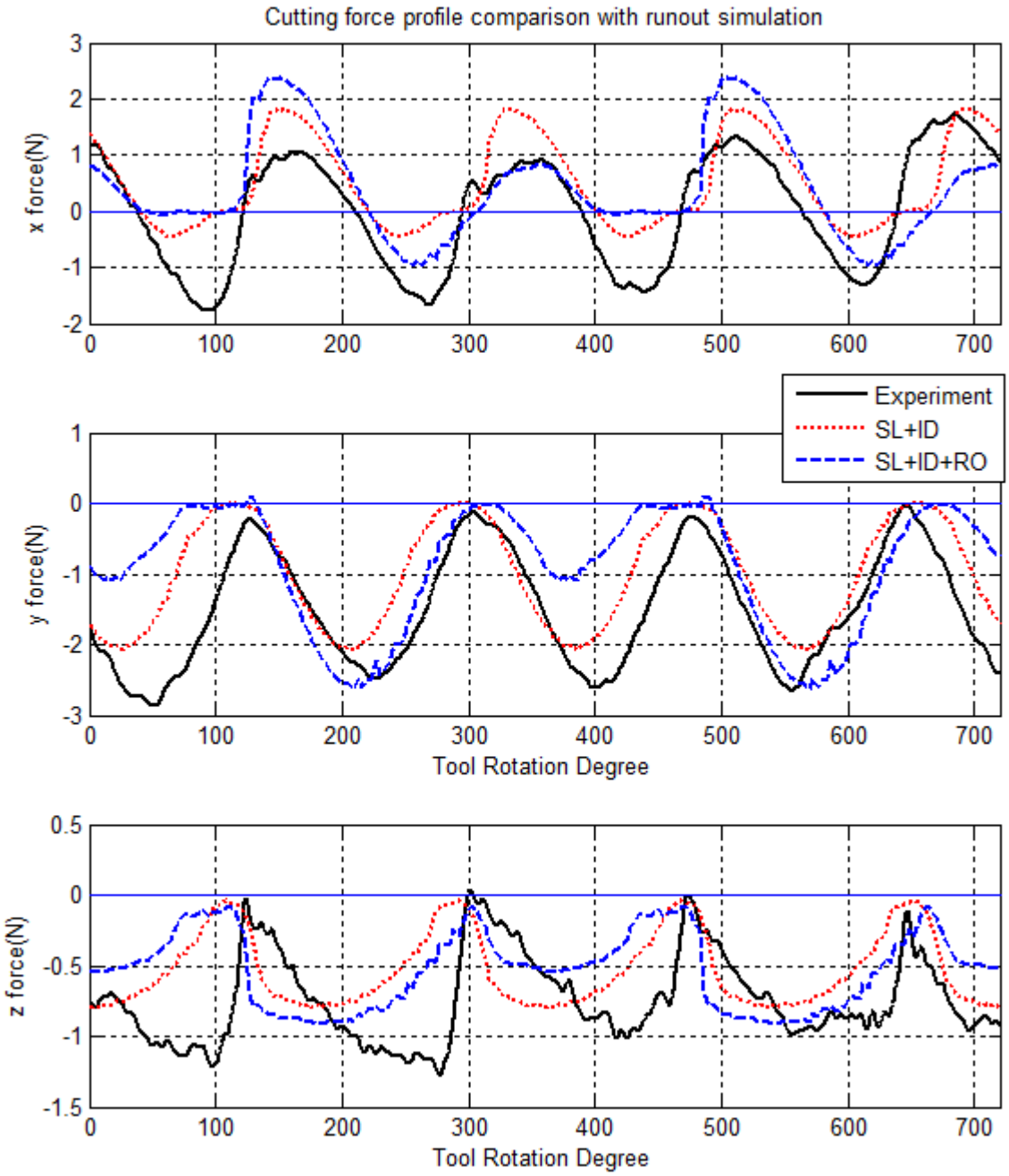

Figure A.6 Measured and simulated cutting forces – Test #6

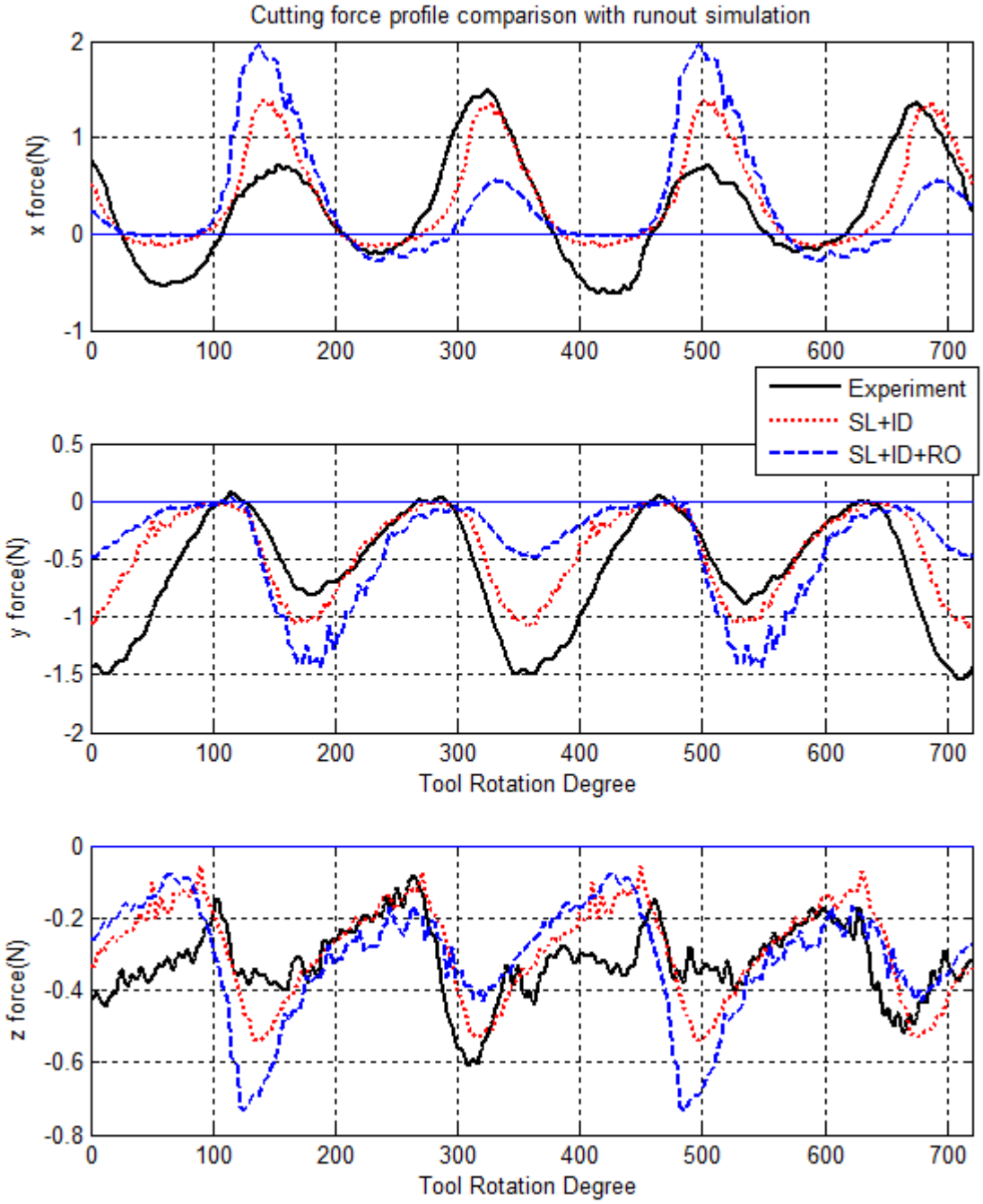

Figure A.7 Measured and simulated cutting forces – Test #8

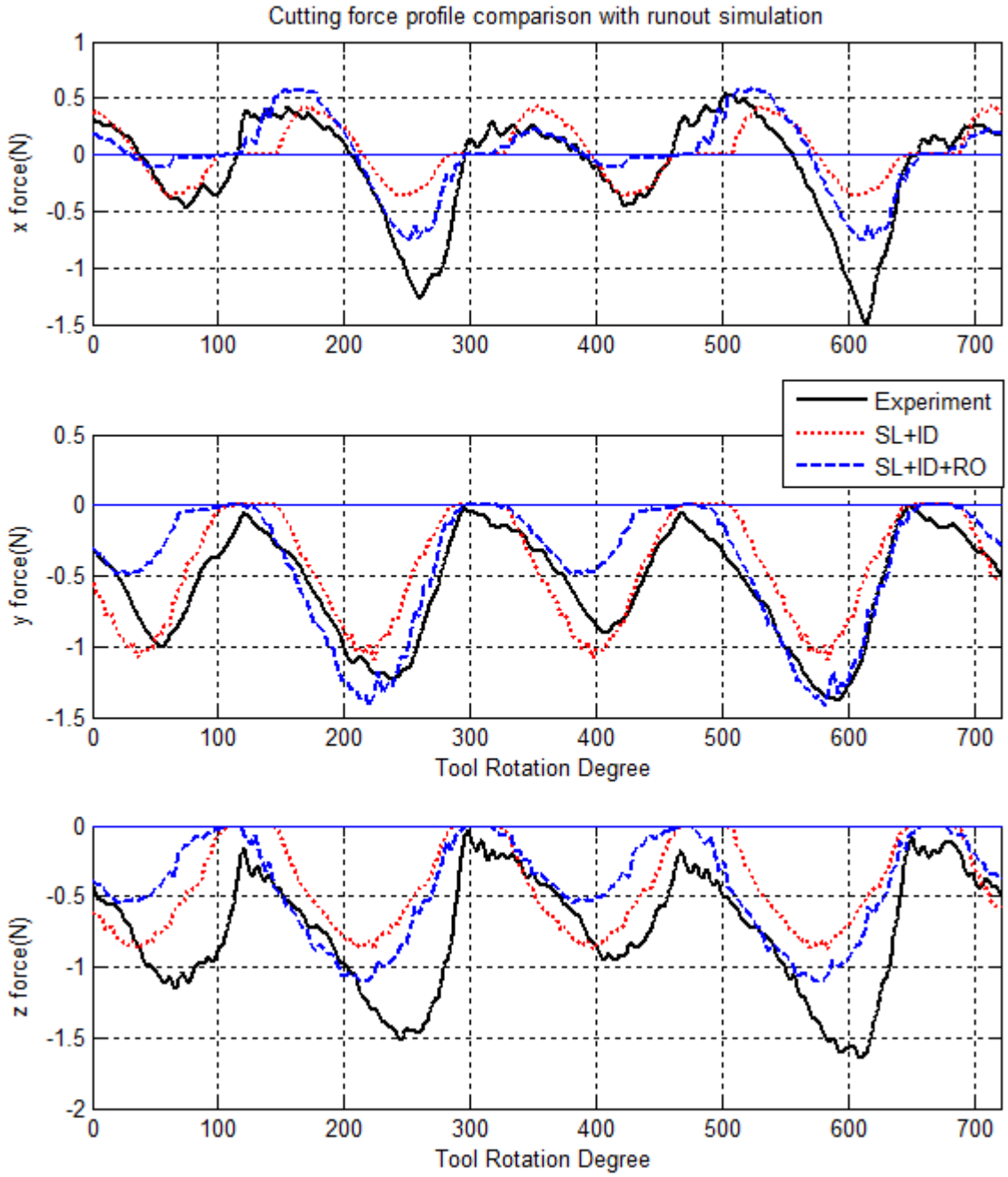

Figure A.8 Measured and simulated cutting forces – Test #9

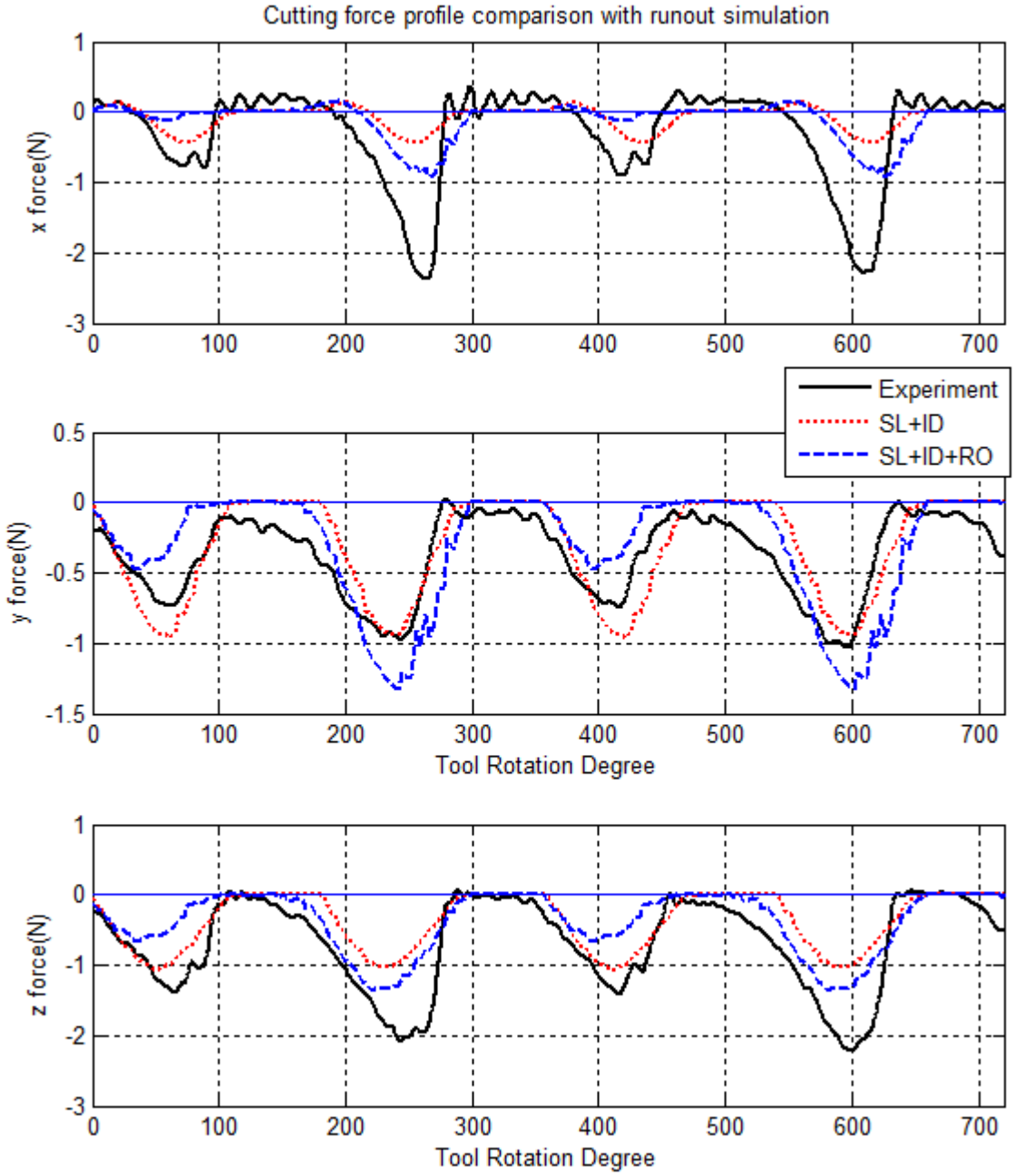

Figure A.9 Measured and simulated cutting forces – Test #10

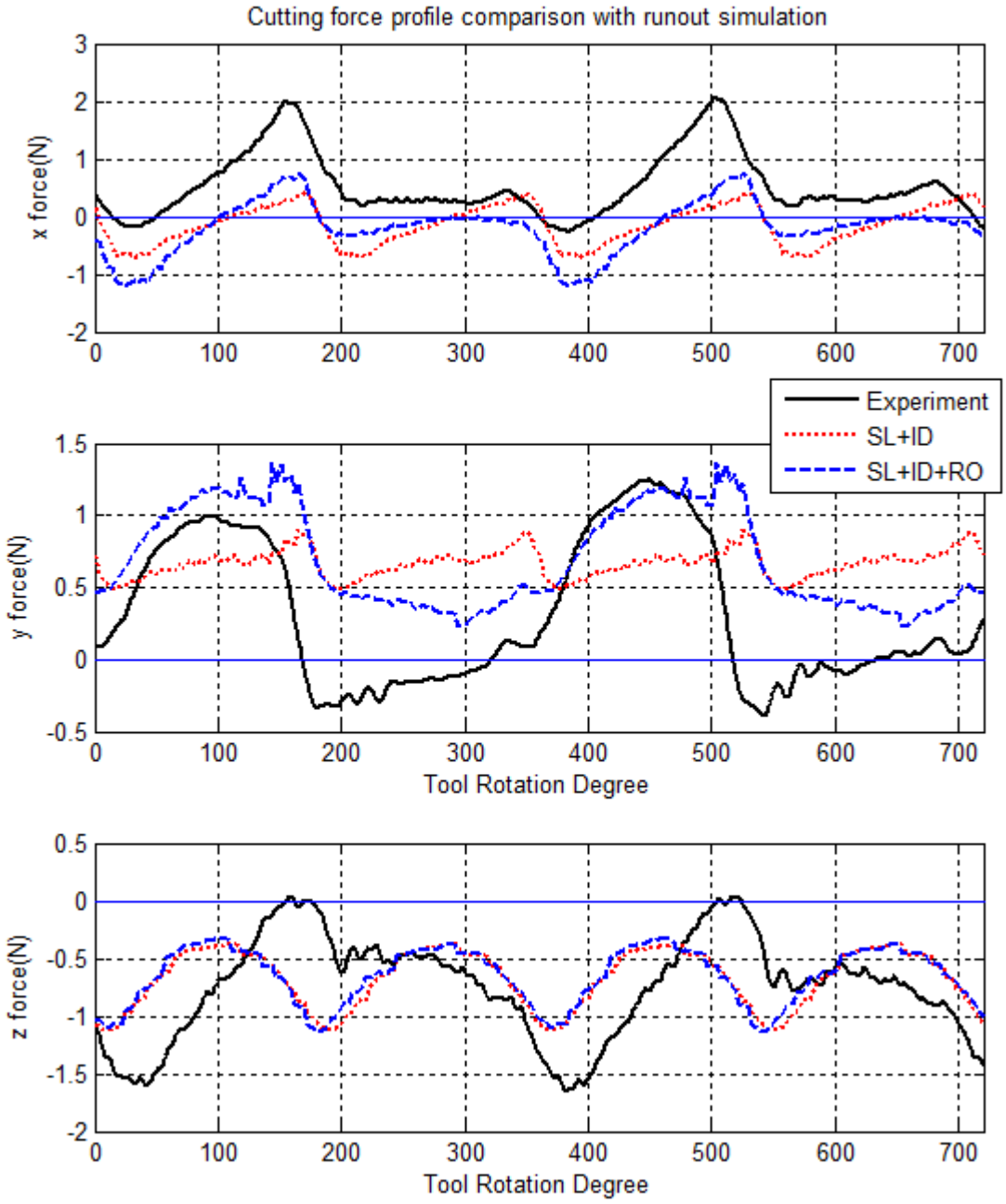

Figure A.10 Measured and simulated cutting forces – Test #11

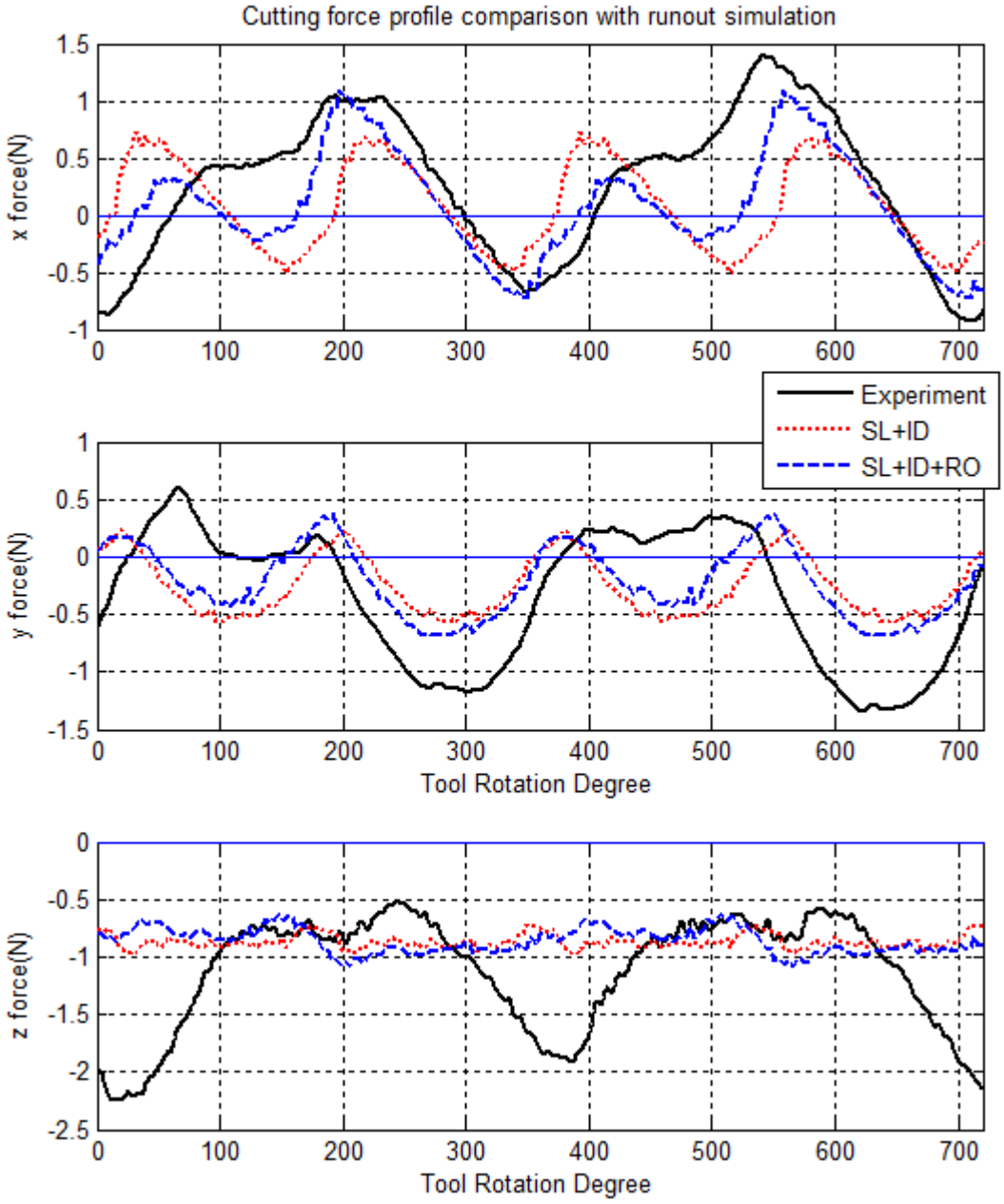

Figure A.11 Measured and simulated cutting forces – Test #12

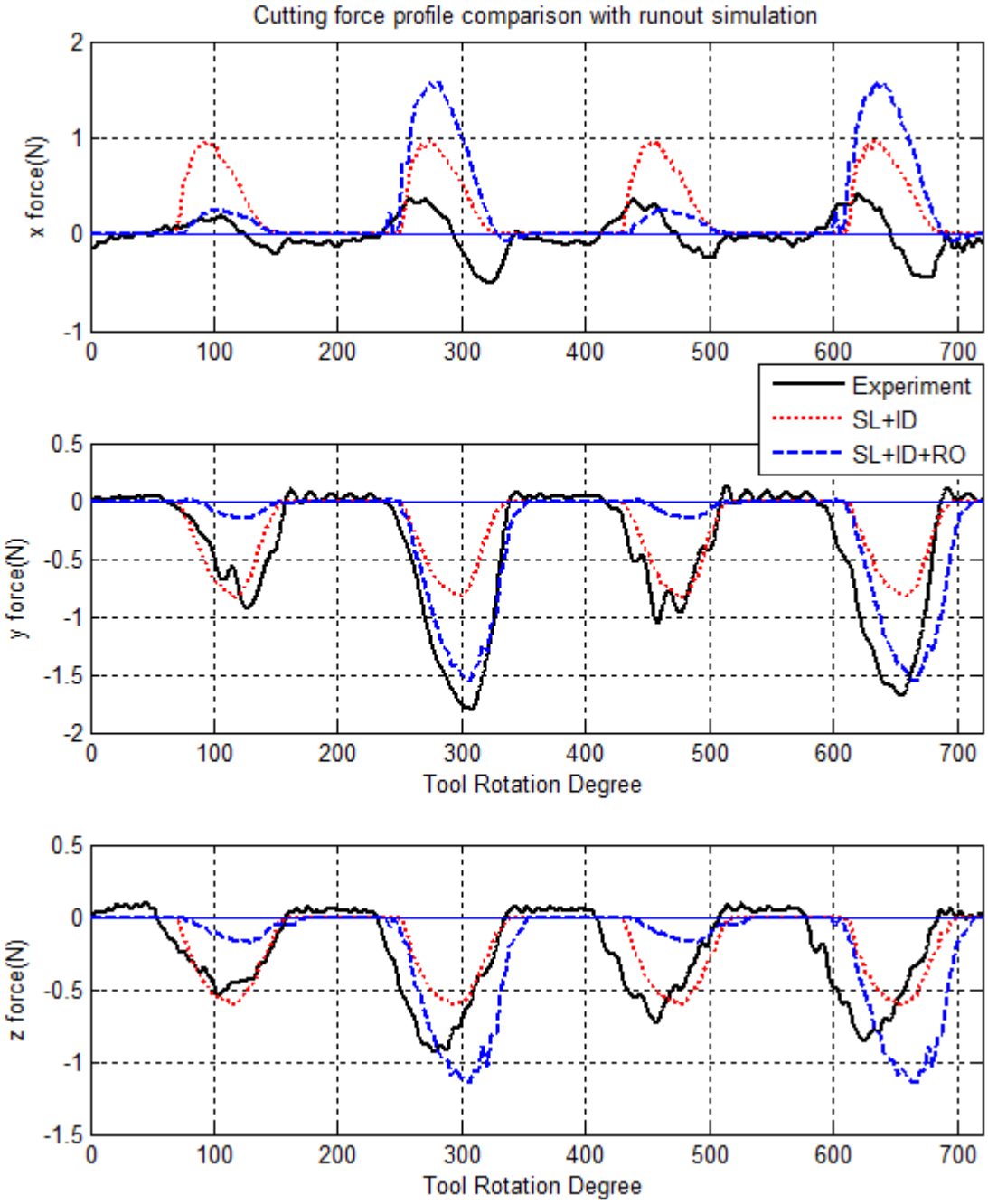

Figure A.12 Measured and simulated cutting forces – Test #14